Spring 4-2014

POSITION/SPEED SENSORLESS CONTROL FOR PERMANENT-MAGNET SYNCHRONOUS MACHINES

Yue Zhao
University of Nebraska-Lincoln, yue.zhao@huskers.unl.edu

POSITION/SPEED SENSORLESS CONTROL FOR PERMANENT-MAGNET SYNCHRONOUS MACHINES

by

Yue Zhao

A DISSERTATION

Presented to the Faculty of

The Graduate College at the University of Nebraska

In Partial Fulfillment of Requirements

For the Degree of Doctor of Philosophy

Major: Electrical Engineering

Under the Supervision of Professor Wei Qiao

Lincoln, Nebraska

May, 2014

POSITION/SPEED SENSORLESS CONTROL FOR PERMANENT-MAGNET SYNCHRONOUS MACHINES

Yue Zhao, Ph.D.

University of Nebraska, 2014

Advisor: Wei Qiao

Permanent-magnet synchronous machines (PMSMs) are widely used in industrial applications owing to their distinctive advantages, such as high efficiency, high power density, and wide constant power region. To achieve high-performance field oriented control, accurate rotor position information, which is usually measured by rotary encoders or resolvers, is indispensable. However, the use of these sensors increases the cost, size, weight, and wiring complexity and reduces the mechanical robustness and the reliability of the overall PMSM drive systems. The goal of the research for this dissertation was to develop a rotor position/speed sensorless control system with performance comparable to the sensor-based control systems for PMSMs over their entire operating range.

In this work, different sensorless control methods were developed for different speed regions. In the medium- and high-speed regions, quasi-sliding-mode observer-based position estimators were proposed to obtain rotor position information. Several assistive algorithms, including an online observer parameter adaption scheme, a model reference adaptive system based speed estimator, and an estimated speed-based oscillation mitigation scheme, were proposed to improve the performance of the rotor

position estimation and the sensorless PMSM control system. The proposed methods were effective for both salient-pole and nonsalient-pole PMSMs. In the low-speed region, saliency tracking observers are commonly used for rotor position estimation of salient-pole PMSMs. However, for a nonsalient-pole PMSM, due to the symmetric rotor structure, the dependence between rotor position and spatial saliency is weak. This research proposed a novel high frequency square-wave voltage injection-based rotor position estimation method, which is much less dependent on the machine rotor asymmetry and is well suited for nonsalient-pole PMSMs.

The proposed sensorless control offers an effective means to solve the problems incurred in using position sensors in PMSM control systems. Firstly, it provides an alternative to existing sensor-based controls for PMSMs with reduced cost, size, weight, and hardware complexity. Second, it can be used as a supplementary (backup) function in the sensor-based control systems, when the sensor failure occurs. Moreover, the estimated rotor position and speed and other state variables of the PMSMs can be used for condition monitoring of the position sensors and other components in the PMSM drive system.

ACKNOWLEDGMENT

First and foremost, I would like to express my deep gratitude to my advisor, Prof. Wei Qiao, for his unwavering guidance, encouragement, and continuous support for all of the technical and personal aspects of my studies. I am deeply impressed by his patience, motivation, enthusiasm, and immense knowledge. His advice and suggestions will be of great help in my future career.

I would like to thank other members of my supervisory committee, Prof. Jerry Hudgins, Prof. Liyan Qu, and Prof. Anuj Sharma, for their valuable suggestions and insightful comments on my dissertation research as well as their assistance throughout the process of my Ph.D. work. I would also like to thank Prof. Dean Patterson for his advice.

I am very grateful to Dr. Long Wu with John Deere Electronic Solutions (JDES) for his continuous support. With his help and support, I have made great progress in my research. I am also grateful to Mr. David Gordon, Mr. Tianjun Fu, and all of the other members in the software department of JDES. I especially appreciate the positive technical collaboration, access to power electronics test resources, and financial support provided by JDES, through a sponsored research program in sensorless control.

Additionally, I am also grateful to all of my colleagues, Dr. Xiang Gong, Mr. Zhe Zhang, Mr. Jianwu Zeng, Mr. Ze Wang, Mr. Cong Ma, Mr. Taesic Kim, and Mr. Chun Wei, in the Power and Energy Systems Laboratory for their friendship and technical insight.

Last but not least, I am always indebted to my parents, Xinfang Zhao and Huijuan Wu, my girlfriend, Manting Zhang, and my family members for their endless support and

love throughout these years. They gave me additional motivation and determination during my doctoral study.

Financial support from the following institutions/organizations is gratefully acknowledged:

- National Science Foundation, USA
- University of Nebraska-Lincoln
- IEEE Industrial Electronics Society
- IEEE Power and Energy Society

TABLE OF CONTENTS

LIST OF SYMBOLS AND ABBREVIATIONS

x	measured or actual value of variable x
x^*	reference value of x
$\hat{x}$	estimated value of x
$x^* - x$	tracking error
$x - \hat{x}$	estimation error
$\dot{x}$	derivative of x

ALE	adaptive line enhancer
BLDC	brushless DC
CPSR	constant power speed region
CSMO	continuous-time sliding mode observer
CT	current transducer
DFIG	doubly-fed induction generator
DSMO	discrete-time sliding mode observer
DSP	digital signal processor
e_a	back electromotive force of phase a
EEMF	extended electromotive force
E_{ext}	magnitude of the extended electromotive force
EKF	extended Kalman Filter
EMF	electrommotive force
EMI	electromagnetic interference

ETDS	electric traction drive system
EV	electric vehicle
FEA	finite element analysis
FOC	filed-oriented control
HEV	hybrid electric vehicle
HF	high-frequency
HFSI	high frequency signal injection
i_a and i_b	measured *a*-phase and *b*-phase currents
i_d and i_q	*d*-axis and *q*-axis stator currents in *dq* rotor reference frame
$i_{d,h}$ and $i_{q,h}$	induced *d*-axis and *q*-axis high-frequency currents in *dq* rotor reference frame
i_α and i_β	α-axis and β-axis stator currents in $\alpha\beta$ stationary reference frame
IM	indution machine
INFORM	indirect flux detection by on-line reactance measurement
IPMSM	interior permanent-magnet synchronous machine
k	gain of the switching terms in sliding mode observer
l	sliding mode observer feedback gain
L_d and L_q	*d*-axis and *q*-axis inductances
LPF	low-pass filters
L_{sa}	synchronous inductance of phase *a*
MA	moving average
MRAS	model reference adaptive system

MTPA	maximum torque per ampere
p	the derivative operator
PI	proportional-integral
PLL	phase-locked loop
p_o	the number of magnetic pole pairs
PM	permanent-magnet
PMSG	permanent-magnet synchronous generator
PMSM	permanent-magnet synchronous machine
PWM	pulse-width modulation
QSMO	quasi-sliding mode observer
$R_{d,h}$ and $R_{q,h}$	d-axis and q-axis high-frequency resistances
R_s	the resistance of the stator windings
S	sliding surface
sgn	sign function
SMO	sliding mode observer
SNR	signal-to-noise ratio
SPMSM	surface-mounted permanent-magnet synchronous machine
SRM	switched reluctance machine
SVPWM	space vector pulse-width modulation
T_e	electromagnetic torque
V	candidate Lyapunov function
V_{dc}	dc bus voltage
v_a	stator terminal voltage of phase a

v_d and v_q	*d*-axis and *q*-axis stator terminal voltages in *dq* rotor reference frame
$v_{d,h}$ and $v_{q,h}$	*d*-axis and *q*-axis high-frequency voltages injected into the ideal *dq* rotor reference frame
$v_{\gamma,h}$ and $v_{\delta,h}$	γ-axis and δ-axis high-frequency voltages injected into the $\gamma\delta$ estimated rotor reference frame
VFD	variable-frequency drive
VSI	voltage source inverter
WECS	wind energy conversion system
$Z_{d,h}$ and $Z_{q,h}$	*d*-axis and *q*-axis high-frequency impedances
Z_0	width of the boundary layer in sliding mode observer
$Z_{\min}$	minimum of Z_0
η	amplitude of the extended electromotive force
θ_{re}	measured or actual rotor position angle
λ_{ext}	magnitude of the position-related flux term
λ_m	flux linkage generated by the permanent magnets
$\psi_{r\alpha}$ and $\psi_{r\beta}$	α-axis and β-axis rotor flux linkages in $\alpha\beta$ stationary reference frame
$\psi_{s\alpha}$ and $\psi_{s\beta}$	α-axis and β-axis stator flux linkages in $\alpha\beta$ stationary reference frame
ω_c	cut off frequency of the low-pass filter
ω_h	frequency of the injected signals
ω_{re}	measured or actual electrical angular velocity of the rotor

LIST OF FIGURES

Chapter 4

Chapter 5

Chapter 6

Chapter 7

LIST OF TABLES

Chapter 3

Chapter 6

LIST OF APPENDICES

CHAPTER 1

INTRODUCTION

1.1 Background

Due to the convenience of torque and speed control, DC electric machine drive systems had been adopted in a variety of industrial applications for more than 100 years. During the past 30 years, with the development of power electronics, digital signal processors (DSPs), and computer-aided design technologies, AC motor drives [1]-[3] have replaced DC motor drives and have become dominant in variable-frequency drive applications. Currently, various types of AC drives using induction machines (IM), permanent-magnet synchronous machines (PMSM), switched reluctance machines (SRM), etc., are widely used in industrial applications.

Among the AC motor drives, PMSM drive systems have been used more and more in many industrial applications, e.g., home appliances [4], electric-drive vehicle systems [5], and wind energy conversion systems (WECSs) [6], due to their distinctive advantages of high efficiency, high power density, and wide constant power region. With the continuous reduction in the cost of permanent-magnet (PM) materials and the development of control techniques, PMSM drives have become more attractive and competitive [7]. Moreover, due to worldwide concerns over environmental problems and a possible energy crisis, much effort from both academia and industry has gone into the development of renewable energy conversion systems and electric-drive vehicles, creating a large market for PMSM drive technologies.

1.2 Permanent-Magnet Synchronous Machines

In general, the most widely used PMSMs [8] have an external stator with conductors and an internal rotor with PMs. According to the rotor structures, the PMSMs with an approximately sinusoidal back electromotive force (EMF) can be broadly characterized into two major categories: nonsalient-pole PMSMs, e.g., surface-mounted PMSMs (SPMSM), and salient-pole PMSMs, e.g., interior PMSMs (IPMSM). A comparison of different types of PMSMs can be found in [9] and [10].

The cross-section of a typical SPMSM is shown in Figure 1.1(a). Since the PMs are mounted on the surface of the rotor core, the SPMSM has a uniform effective air gap. This property makes the synchronous inductances in direct (*d*-) and quadrature (*q*-) axes to be equal. As a result, the SPMSM only produces a magnetic torque. Compared with the IPMSM, the SPMSM has a relatively limited flux-weakening capability. The surface-mounted rotor configuration is simple enough for manufacturing and assembly. However, the PMs are exposed directly to the armature reaction field and at the risk of demagnetization. Due to the surface-mounted rotor structure, the shaft rotating speed should be limited in order to keep the PMs at the rotor surface against the effect of the centrifugal force. Therefore, SPMSMs are commonly used in low-speed applications, e.g., WECSs and home appliances.

A typical cross-section of an IPMSM is shown in Figure 1.1(b), where the magnets are buried and effectively shielded in the rotor iron, which significantly reduces the risk of demagnetization of the PMs during the flux-weakening operation. Due to the rotor saliency, the *d*-axis and *q*-axis inductances are different. Both the magnetic torque

and the reluctance torque contribute to the total torque produced by the IPMSM. For these reasons, IPMSM are more applicable for traction applications in electric-drive vehicle systems, which require flux weakening operation and high output torque.

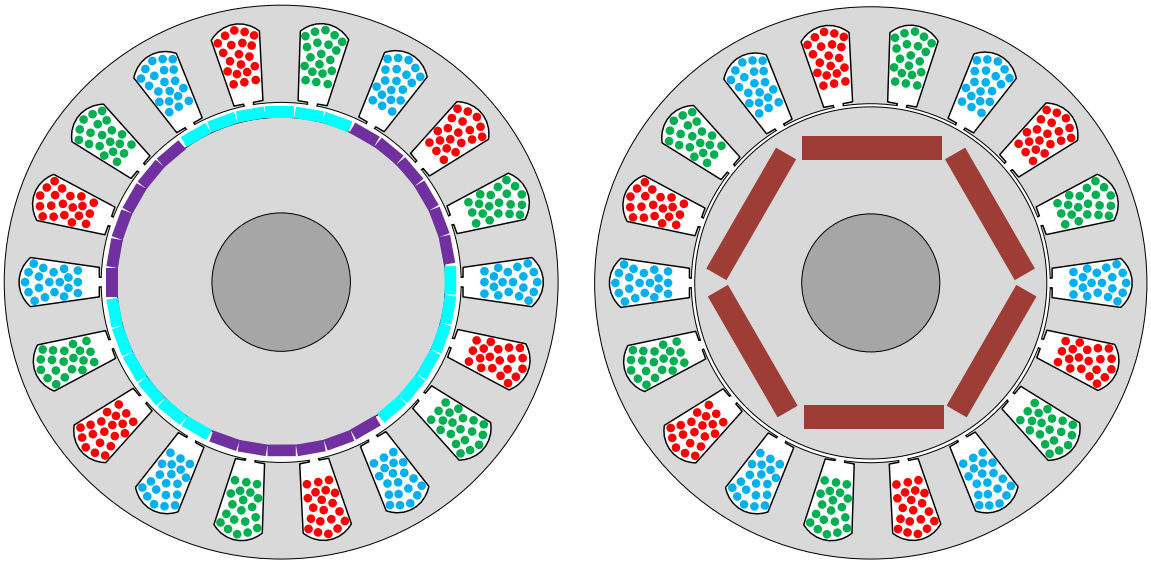

(a) (b)

Figure 1.1: Illustrations of typical PMSMs: (a) a cross-section of SPMSM and (b) a cross-sections of IPMSM.

1.3 Applications for PMSM Drives–Examples

PMSMs are attractive for applications, e.g., electric traction drive systems (ETDS) in electric-drive vehicles and permanent-magnet synchronous generator (PMSG)-based variable-speed WECSs, which require a high power/energy density in terms of weight and volume.

U.S. is the world's leading market for advanced electric-drive vehicles [11], e.g., electric and hybrid electric vehicles (EVs and HEVs), which will play the most essential role in the large-scale reduction of automobile oil use, U.S. dependence on foreign oil

[11], and CO_2 emissions from the transportation sector. Compared to the conventional internal combustion engine (ICE)-based propulsion system, ETDS [12]-[17] has higher peak power, improved dynamic performance, nearly ideal torque-speed characteristics, better fuel efficiency, and reduced CO_2 emissions. In general, the traction motors in ETDSs are required to provide large shaft torque in the low-speed region (including the stall condition) and a wide constant power speed region (CPSR). Compared to other types of AC machines, the PMSMs can be well designed to have a wider CPSR and be operated in both the constant torque control mode below the base speed and the constant power mode above the based speed [18], [19]. Furthermore, since PMSMs have high power density, torque density, and efficiency, the size of the overall drive system can be significantly reduced, which is an attractive feature in vehicular applications. Up-to-date, electric-drive vehicles equipped with PMSM-based ETDSs, e.g., Toyota's Prius [20], have been mass produced.

The total installed capacity of wind power is growing tremendously in the global market. According to a report of the World Wind Energy Association [21], worldwide wind power installation has reached 296 GW by the end of June 2013. Among various configurations of WECSs, the doubly-fed induction generator (DFIG)-based variable-speed WECSs have been the dominant technology in the market since late 1990s [22]. However, this situation has changed in recent years with the developing trend of WECSs with larger power capacity, lower cost per kW, increased power density, and the need for higher reliability. More and more attention has been paid to direct-drive, gearless WECS concepts.

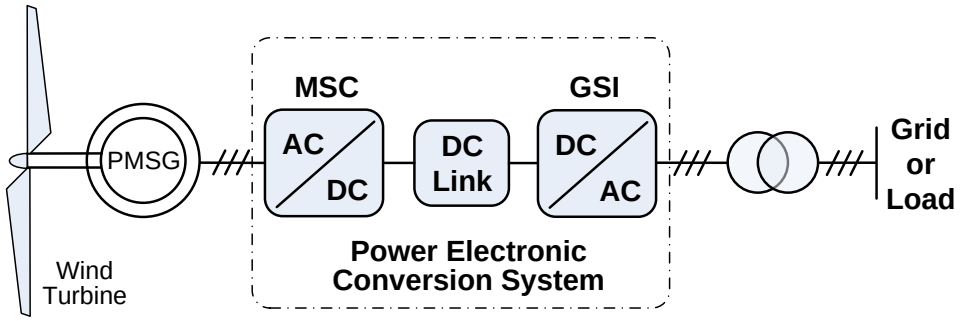

Figure 1.2: Schematic diagram of a direct-drive PMSG-based WECS connected to a grid or local load (MSC = machine-side converter; GSI = grid-side inverter).

Among different types of generators, PMSGs have been found to be more superior in direct-drive WECS applications due to their advantages of higher efficiency, higher power density, lower maintenance costs, and better grid compatibility [23]. Increased reliability as well as higher performance make the PMSG-based direct-drive WECSs, as shown in Figure 1.2, more attractive in multi-MW offshore applications, where the WECSs are installed in harsh and less-accessible environments [23].

Currently, there are a wide variety of commercial PMSG-based direct-drive WECSs on the market, with power ratings ranging from hundreds of watts to 6 MW [24], [25]. Many wind turbine manufacturers, such as Siemens Wind Power, General Electric Energy, Goldwind, etc., have adopted direct-drive PMSG concepts in their WECS products.

1.4 Space Vector Control of PMSM Drives

High-performance motion control for a PMSM is characterized by smooth rotation and accurate torque control over the entire speed range (including standstill) and fast acceleration and deceleration. The vector control techniques [2], [26], also referred to

as the field-oriented control (FOC), are widely adopted to achieve high-performance control of PMSM drives. To perform the vector control, stator currents of a PMSM are decomposed into a magnetic-field-generating part and a torque-generating part, which can be controlled independently. In this manner, the flux and torque can be controlled separately by using the decomposed current components. The structure of the PMSM vector control scheme is then as simple as that of a separately excited DC machine.

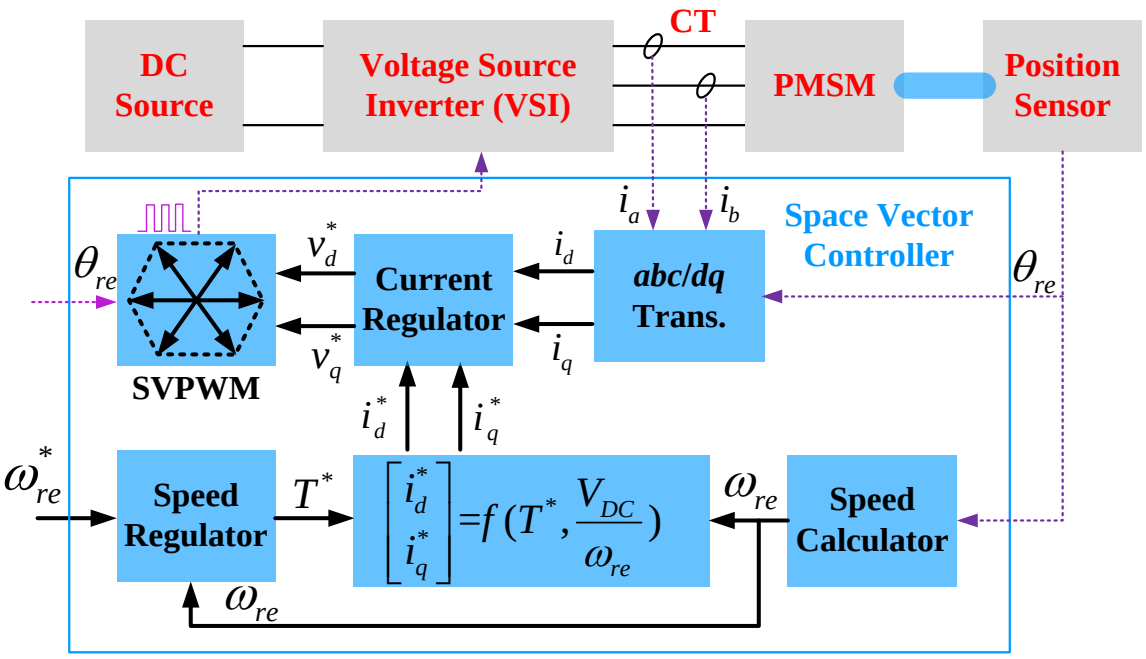

Figure 1.3: Overall block diagram of a PMSM drive system using a position-sensor-based space vector control scheme.

The overall block diagram of a PMSM drive system using a position-sensor-based space vector control scheme is shown in Figure 1.3, including the control scheme, a PMSM, a voltage source inverter (VSI), a DC source, and current and position sensors. To perform the vector control, the following steps are necessary:

1. Sensing and processing of current and rotor position

- Measure the stator phase currents of the PMSM using current transducers (CTs). Owing to the redundancy, the measurements of two phase currents, e.g., i_a and i_b, are sufficient.
- Measure the rotor position information θ_{re} using a rotor position sensor, e.g., a resolver or an encoder.
- Coordinate transformation: transform the stator phase currents i_a and i_b into the currents i_d and i_q in the synchronously rotating (rotor) reference frame using measured rotor position information.

2. Torque command and current commands generation
   - Generate the torque command T^* based on the tracking error between the desired rotor speed ω_{re}^* and the measured rotor speed ω_{re} using a speed regulator.
   - Generate the current commands, i_d^* and i_q^*, according to the relationship among i_d^*, i_q^*, T^*, and V_{dc}/ω_{re} (the ratio between the DC bus voltage and the rotor speed). This relationship is usually implemented by lookup tables in practical applications [27].
3. Current regulation and gate signals generation
   - Perform the decoupled current control by using two current regulators, in which the torque- and flux-producing components of the stator currents, i_q and i_d, are controlled separately. This step will generate reference voltages, v_d^* and v_q^*, in the synchronously rotating reference frame.

- Perform the space vector pulse width modulation (SVPWM) based on v_d^* and v_q^*, and generate the gate signals for the VSI. In this step, rotor position information is required to transform v_d^* and v_q^* into v_α^* and v_β^*.

1.5 Rotor Position Sensorless Space Vector Control of PMSM Drives

In the vector control scheme, there are three blocks using the rotor position information: 1) calculate i_d and i_q using the Park transformation, 2) calculate v_α^* and v_β^* using the inverse Park transformation, and 3) rotor speed calculation. Therefore, the rotor position is indispensable for high performance space vector control of PMSM drives. Inaccurate rotor position information will not only degrade the control performance but also cause instability in the control system.

Electromechanical position sensors, e.g., resolvers, optical encoders, and hall-effect sensors, are commonly used to obtain rotor position/speed in PMSM drives. The use of these sensors increases the cost, size, weight, and hardware wiring complexity of drive systems. From the viewpoint of system reliability, mounting electromechanical sensors on rotor shafts will degrade mechanical robustness of the electric machines. The electromagnetic interference (EMI) noise in the wiring harness, due to switching events and broken wires, may be fatal to the controller's operation. Moreover, sensors are often subject to high failure rates in harsh environments, such as excessive ambient temperature, super high-speed operation, and other adverse or heavy load conditions. To overcome these drawbacks of using position sensors, much research effort has gone into

the development of sensorless drives that have comparable dynamic performance with respect to the sensor-based drives during the last decades [28].

1.6 Research Objectives

The goal of the research for this dissertation was to develop a rotor position/speed sensorless control system that has performance comparable to the sensor-based control systems for PMSMs over their entire operating range. The sensorless control offers an effective means to solve the problems incurred in using electromechanical position sensors in PMSM drive systems. First, it provides an alternative to the existing sensor-based controls for PMSMs with reduced cost, size, weight, and hardware complexity. Second, it can be used as a supplementary (backup) function in the sensor-based control systems. When there are problems with sensors, the sensorless control ensures that the PMSM drive systems can still work properly. This prevents subsequent failures of other system components caused by the failure of the sensors and control system. Finally, the estimated rotor position and speed and other state variables of the PMSMs can be used for condition monitoring of the electromechanical sensors and other PMSM components. This reduces the failure rate and level, saves maintenance costs, and improves the reliability of the PMSM drive systems.

The main objectives of this research included:

1. Develop multiple sensorless control systems for generic salient-pole PMSMs for medium- and high-speed applications. The sensorless control systems should be robust to operating conditions and have zero phase lag in both steady-state and transient conditions. In addition, the

sensorless control systems should be robust to the variations of machine parameters. The sensorless controls are also applicable to nonsalient-pole PMSMs, which are special cases of salient-pole PMSMs.

2. Develop a position/speed estimation scheme and sensorless control for nonsalient-pole PMSMs in the low-speed region. By tracking the inherent rotor saliency of nonsalient-pole PMSMs, the high frequency signal injection (HFSI)-based rotor position estimation can be effective in the low-speed range and even at standstill. However, due to the symmetric rotor structure of a nonsalient-pole PMSM, the dependence between rotor position and spatial inductance is not sufficient for the rotor position estimation. To solve this problem, this research develops a rotor position/speed sensorless control, which has little dependence on machine rotor asymmetry and is well suited for nonsalient-pole PMSMs.

1.7 Dissertation Organization

The dissertation is organized in the following manner:

Chapter 2 is a literature review of rotor position/speed estimation techniques for sensorless control of PMSMs. Indirect position sensing and model- and saliency-based rotor position estimation methodologies for both salient- and nonsalient-pole PMSMs are reviewed.

Chapter 3 describes two model-based rotor position/speed estimation schemes for generic salient-pole PMSMs. First, a model reconstruction method is presented to construct appropriate dynamical PMSM models for the design of the rotor position estimators. Then, two quasi-sliding-mode observers (QSMOs), i.e., an extended EMF (EEMF) based QSMO and an extended flux based QSMO, used for rotor position/speed estimations of the salient-pole PMSMs are described. The estimators are integrated into the vector control to form the rotor position/speed sensorless vector control schemes for the salient-pole PMSM drives.

Chapter 4 describes an integrated rotor position/speed estimator, which includes an improved model reference adaptive system (MRAS)-based rotor speed estimator and an estimated speed-based oscillation mitigation scheme for the rotor position estimation. The estimator improves the transient performance and stability of the sensorless control systems presented in Chapter 3.

Chapter 5 describes an HFSI-based sensorless control for nonsalient-pole PMSMs for low-speed operating conditions. A high-frequency (HF) square-wave voltage signal is injected, which significantly increases the control bandwidth of the speed controller.

Chapter 6 provides a detailed description of the simulation models and experimental test setups for simulation and experimental validation of the sensorless control system.

Chapter 7 validates the sensorless control schemes by using numerous simulation studies and experimental results.

Chapter 8 provides the concluding remarks and contributions of this dissertation research and recommendations for future work.

CHAPTER 2

A LITERATURE REVIEW ON ROTOR POSITION/SPEED ESTIMATION TECHNIQUES FOR PMSMS

To achieve high-performance vector control for PMSMs, accurate measurements of rotor position and speed are indispensable, which, in conventional PMSM drive systems, are usually obtained by using rotary encoders or resolvers. The use of these sensors increases the cost, size, and wiring complexity and reduces the mechanical robustness and reliability of PMSM drive systems. To solve these problems, much research effort has gone into the development of rotor position/speed sensorless drives that have dynamic performance comparable to the position sensor-based drives during the last few decades [28]-[32]. This chapter provides a brief literature review of the methods of estimating the rotor position/speed information without using position sensors, which is the key to achieving rotor position/speed sensorless vector control for PMSM drives.

The rotor position/speed estimation methods can be classified into three major categories:

1. *Indirect position sensing methods* in which the rotor position information is obtained indirectly from the sensed position-related quantities, e.g., back EMF components or third harmonic back EMF.
2. *Model-based methods* in which the fundamental-frequency model of PMSM, measured stator currents, and measured or commanded stator voltages are utilized to estimate the rotor position information.

3. *Saliency-based methods* in which the rotor position information is extracted from the position-dependent machine saliency and an HF excitation is usually required.

The relationship among the three categories of methods is illustrated in Figure 2.1. Each category of methods can be performed through simple and straightforward open-loop techniques. However, to improve the accuracy of the rotor position estimation, the trend in recent research is toward the design of closed-loop position estimation methods. Therefore, the observer design has become the core part of position estimation.

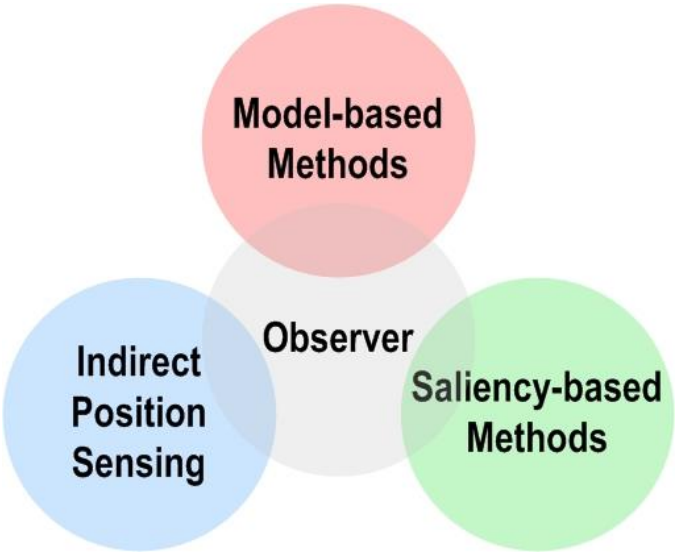

Figure 2.1: Illustration of three major categories of methods to obtain rotor position information without using position sensors.

2.1 Indirect Position Sensing Methods

The basic idea of this category of methods is to obtain the rotor position information indirectly from the sensed position related signals, e.g., the instantaneous magnitude of the back EMF, which is a function of rotor position. These methods were firstly applied to the brushless DC (BLDC) motors, which have trapezoidal back EMF waveforms, where the rotor position was obtained from the detected zero-crossing points on the back EMF [33], [34]. However, back EMF sensing does not work in low-speed operating conditions. To solve this problem, an open-loop starting procedure is needed. Moreover, the base speed is the maximum achievable speed using this method. In addition, the methods presented in [33] and [34] could not be applied to permanent-magnet AC machines, especially the IPMSMs, which have a distorted airgap flux distribution due to the armature reaction.

Reference [35] proposed an indirect position sensing method based on the third harmonic component of the back EMF, which has a constant phase relationship with the rotor flux regardless of the machine operating mode. The third harmonic component is extracted from the stator phase voltages while the fundamental and other higher order harmonic components are eliminated via a simple summation of the three phase voltages. Compared to the aforementioned back EMF sensing methods, this method needs less filtering and has an improved capability to operate in a lower-speed region. This method is particularly applicable to the BLDCs with trapezoidal back EMFs. Other third harmonic back EMF-based indirect position sensing methods, which can be applicable to both BLDCs and SPMSMs, were presented in [36], [37].

In [37], three sensing methods of the third harmonic back EMF were demonstrated. The effectiveness of these methods was verified on both BLDCs and SPMSMs, including the sensorless speed control in the flux weakening region. However, similar to all other EMF-based sensorless control methods, an open-loop starting procedure has to be employed. Very recently, an improved position estimation method was presented in [38] for a PMSM, which combined a third harmonic back EMF sensing method and a position observer. In this method, the integral of the third harmonic back EMF, which is the third harmonic flux linkage, was utilized as a reference. The error between the estimated and reference third harmonic flux linkages was used to compensate the speed estimation error. The rotor position was then calculated based on the compensated rotor speed. This method has been reported to achieve better position estimation accuracy than the previous work.

2.2 Model-Based Methods

Methods based on the fundamental-frequency PMSM models are most widely used for rotor position and speed estimation. These model-based methods are especially effective for medium- and high-speed applications. They can be generally grouped into two different categories: open-loop calculation and closed-loop observers. The open-loop position/speed estimation methods are straightforward and easy to implement. These methods behave like real-time dynamic models of the PMSMs. They receive the same control inputs and run in parallel. Based on the dynamic model of a PMSM, the states of interest, e.g., back EMF, rotor flux, or stator inductance, can be calculated, from which the rotor position and speed information can be extracted.

In a closed-loop observer, both the control inputs of the plant and the output tracking error, i.e., the error between the outputs of the plant and the observer, are often used as the inputs to the observer. The observer gains are designed to force the observer output to converge with the plant output. Thus, the estimated values of the states of interest are forced to converge to their actual values. From this aspect, the closed-loop observer can be viewed as an adaptive filter, which has a good disturbance rejection property and good robustness to the variations of machine parameters and the noises in current/voltage measurements. In the literature, many observers have been proposed for rotor position/speed estimation, such as disturbance observers, sliding-mode observers (SMO), extended Kalman filters (EKF), etc. In this section, the commonly used dynamic models of generic PMSMs are reviewed first. Then a review of both the open-loop calculation and closed-loop estimation methods is presented.

2.2.1 Dynamic Models of Generic PMSMs

A PMSM can be modeled by using phase *abc* quantities. Through proper coordinate transformations, the dynamic PMSM models in the *dq* rotor reference frame and the *αβ* stationary reference frame can be obtained. The relationship among these reference frames are illustrated in Figure 2.2. The dynamic model of a generic PMSM can be written in the *dq* rotor reference frame as:

$$\begin{bmatrix} v_d \\ v_q \end{bmatrix} = \begin{bmatrix} R_s & -\omega_{re} L_q \\ \omega_{re} L_d & R_s \end{bmatrix} \cdot \begin{bmatrix} i_d \\ i_q \end{bmatrix} + \begin{bmatrix} L_d & 0 \\ 0 & L_q \end{bmatrix} \cdot p \begin{bmatrix} i_d \\ i_q \end{bmatrix} + \omega_{re} \lambda_m \begin{bmatrix} 0 \\ 1 \end{bmatrix} \tag{2.1}$$

where v_q and v_d are the *q*-axis and *d*-axis stator terminal voltages, respectively; i_q and i_d are the *q*-axis and *d*-axis stator currents, respectively; L_q and L_d are the *q*-axis and *d*-axis

inductances, respectively, p is the derivative operator; λ_m is the flux linkage generated by the permanent magnets, R_s is the resistance of the stator windings; and ω_{re} is the electrical angular velocity of the rotor.

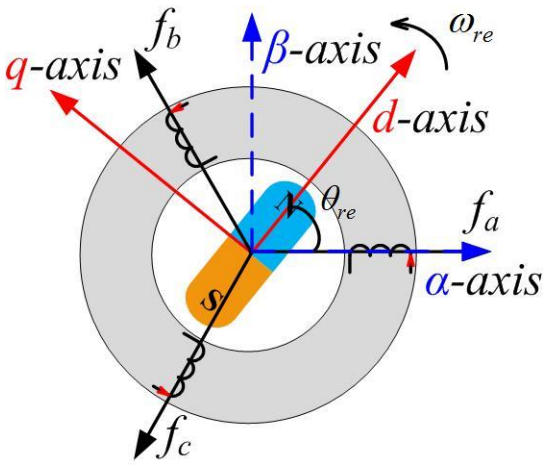

Figure 2.2: Definitions of coordinate reference frames for PMSM modeling.

By using the inverse Park transformation, the dynamics of the PMSM can be modeled in the $\alpha\beta$ stationary reference frame as:

$$\begin{bmatrix} v_\alpha \\ v_\beta \end{bmatrix} = \begin{bmatrix} R_s & 0 \\ 0 & R_s \end{bmatrix} \cdot \begin{bmatrix} i_\alpha \\ i_\beta \end{bmatrix} + \begin{bmatrix} L + \Delta L\cos(2\theta_{re}) & \Delta L \sin\theta_{re} \\ \Delta L \sin\theta_{re} & L - \Delta L\cos(2\theta_{re}) \end{bmatrix} \cdot p \begin{bmatrix} i_\alpha \\ i_\beta \end{bmatrix} + \omega_{re}\lambda_m \cdot \begin{bmatrix} -\sin\theta_{re} \\ \cos\theta_{re} \end{bmatrix} \quad (2.2)$$

where θ_{re} is the rotor position angle; v_α and v_β are the α-axis and β-axis stator voltages, respectively; i_α and i_β are the α-axis and β-axis stator currents, respectively; $L = (L_d + L_q)/2$ and $\Delta L = (L_d - L_q)/2$. For a salient-pole PMSM, since ΔL is nonzero, Equation (2.2) contains both θ_{re} and $2\theta_{re}$ terms, which is not convenient for position estimation. For a nonsalient-pole PMSM, such as an SPMSM, the rotor saliency can be ignored, i.e., $L_d = L_q$. In this case, Equation (2.2) can be simplified as:

$$\begin{bmatrix} v_\alpha \\ v_\beta \end{bmatrix} = \begin{bmatrix} R_s & 0 \\ 0 & R_s \end{bmatrix} \cdot \begin{bmatrix} i_\alpha \\ i_\beta \end{bmatrix} + \begin{bmatrix} L & 0 \\ 0 & L \end{bmatrix} \cdot p \begin{bmatrix} i_\alpha \\ i_\beta \end{bmatrix} + \omega_{re}\lambda_m \cdot \begin{bmatrix} -\sin\theta_{re} \\ \cos\theta_{re} \end{bmatrix} \quad (2.3)$$

As shown in Equation (2.3), only the back EMF components contain the rotor position information. Therefore, if the back EMF components can be estimated, the rotor position can be obtained. In the literature, due to the model's simplicity, numerous model-based position estimation methods for SPMSMs have been proposed based on Equation (2.3). While for salient-pole PMSMs, whose rotor saliency cannot be ignored, i.e., $L_d \neq L_q$, to facilitate the rotor position observation, an EEMF-based salient-pole PMSM model is commonly used. The EEMF-based salient-pole PMSM model can be written in the *dq* rotor reference frame as:

$$\begin{bmatrix} v_d \\ v_q \end{bmatrix} = \begin{bmatrix} R_s & -\omega_{re} L_q \\ \omega_{re} L_q & R_s \end{bmatrix} \cdot \begin{bmatrix} i_d \\ i_q \end{bmatrix} + \begin{bmatrix} L_d & 0 \\ 0 & L_d \end{bmatrix} \cdot p \begin{bmatrix} i_d \\ i_q \end{bmatrix} + E_{ext} \begin{bmatrix} 0 \\ 1 \end{bmatrix} \tag{2.4}$$

where $E_{ext} = \omega_{re}\left[\left(L_d - L_q\right) i_d + \lambda_m\right] - \left(L_d - L_q\right)\left(p i_q\right)$ represents the magnitude of the EEMF components. The EEMF-based salient-pole PMSM model can also be written in the $\alpha\beta$ stationary reference frame as:

$$\begin{bmatrix} v_\alpha \\ v_\beta \end{bmatrix} = \begin{bmatrix} R_s & \omega_{re}\left(L_d - L_q\right) \\ -\omega_{te}\left(L_d - L_q\right) & R_s \end{bmatrix} \cdot \begin{bmatrix} i_\alpha \\ i_\beta \end{bmatrix} + \begin{bmatrix} L_d & 0 \\ 0 & L_d \end{bmatrix} \cdot p \begin{bmatrix} i_\alpha \\ i_\beta \end{bmatrix} + E_{ext} \cdot \begin{bmatrix} -\sin\theta_{re} \\ \cos\theta_{re} \end{bmatrix} \tag{2.5}$$

Similar to Equation (2.3), only the EEMF components contain the rotor position information in Equation (2.5). If the EEMF can be estimated, the rotor position can be obtained.

2.2.2 Open-Loop Calculation

2.2.2.1 Back EMF-Based Methods

The back EMF components in Equation (2.3) and the EEMF components in Equation (2.5) contain the rotor position information. Based on the machine model, the PMSM stator phase currents measured, and measured or commanded stator voltages, the EMF components can be calculated. For example, in [39], the EMF components were calculated as:

$$\begin{cases} E_\alpha = -v_\alpha + R_s i_\alpha + \omega_{re}\left(L_d - L_q\right) i_\beta + L_d p i_\alpha \\ E_\beta = +v_\beta - R_s i_\beta + \omega_{re}\left(L_d - L_q\right) i_\alpha - L_d p i_\beta \end{cases} \tag{2.6}$$

Then the rotor position can be calculated as $\theta_{re} = \tan^{-1}(E_\alpha / E_\beta)$. Although the EEMF concept had not been proposed at that time, it is obvious that Equation (2.6) is equivalent to Equation (2.5). Therefore, the method presented in [39] can be applicable to both salient-pole and nonsalient-pole PMSMs. This method is simple, fast, and straightforward without using complex observers. However, the performance of this method is subjected to the accuracy of the sensed current/voltage and machine parameters.

2.2.2.2 Flux Linkage-Based Methods [40], [41]

At steady state, where $di_\alpha/dt \approx 0$ and $di_\beta/dt \approx 0$, the stator and rotor flux vectors rotate synchronously. Therefore, if the position angle of the stator flux can be calculated, the rotor flux angle can also be determined, which is the same as the rotor position angle.

According to Equation (2.3), the voltage and current components in the stator stationary reference frame can be used to compute the stator and rotor flux linkage as follows:

$$\begin{cases} \psi_{s\alpha} = \int \left(v_\alpha - R_s i_\alpha \right) dt \\ \psi_{s\beta} = \int \left(v_\beta - R_s i_\beta \right) dt \end{cases} \quad \text{and} \quad \begin{cases} \psi_{r\alpha} = \psi_{s\alpha} - L i_\alpha \\ \psi_{r\beta} = \psi_{s\beta} - L i_\beta \end{cases} \tag{2.7}$$

where $\psi_{s\alpha}$ and $\psi_{s\beta}$ are the stator flux linkages, and $\psi_{r\alpha}$ and $\psi_{r\beta}$ are the rotor flux linkages. Then the rotor position can be calculated as $\theta_{re} = \tan^{-1}(\psi_{r\beta}/\psi_{r\alpha})$. The accuracy of the flux-based methods highly depends on the quality and accuracy of the voltage and current measurements. Since integrators are needed in this method, the initial condition of the integration and current sensor DC offset are problems that should be properly handled. In addition, this method may work well in the steady state, but the transient performance is usually unsatisfactory.

2.2.2.3 Inductance-Based Methods [42]

The basic idea for this type of methods is that the spatial distribution of the phase inductance of a PMSM, especially for the PMSM with a significant difference between L_d and L_q, is a function of the rotor position. The phase inductance can be calculated from the measured voltage and current information. Then the rotor position can be found based on the calculated phase inductance. In a PMSM control system, if the switching frequency is high enough, the values of the phase inductance and back EMF can be viewed as constant during a switching period. Under this assumption, the dynamic voltage equation for phase *a* of a PMSM can be expressed as:

$$v_a = R_a i_a + L_{sa} p i_a + e_a \tag{2.8}$$

where all of the variables are phase *a* quantities, v_a is the terminal phase voltage, i_a is the phase current, L_{sa} is the synchronous inductance, R_a is the phase resistance, and e_a is the back EMF. According to Equation (2.8), L_{sa} can be calculated as:

$$L_{sa} = \frac{v_a - R_a i_a - e_a}{p i_a} \tag{2.9}$$

where the instantaneous value of the e_a can be evaluated using the calculated rotor position θ_{re} in the previous two switching cycles, i.e., $e_a[k] = \lambda_m [\theta_{re}[k-1] - \theta_{re}[k-1]] / T_s$. According to the phase inductance obtained by Equation (2.9), the rotor position can be obtained from a lookup table, which was created offline to store the relationship between the rotor position and phase inductance. The accuracy of the inductance-based methods also highly depends on the quality and accuracy of the voltage and current measurements. Since the current and position derivatives need to be calculated in every switching cycle, the rotor position is subjected to a high level of measurement noise. In addition, this type of method requires that the PMSM has a high saliency ratio, e.g., $L_q/L_d > 2.5$; and the performance will be poor for nonsalient-pole PMSMs.

2.2.2.4 Algebraic Manipulation [43]

The basic idea of this method is to solve a set of equations formed by the PMSM model and coordinate transformations, since the rotor position can be expressed in terms of PMSM parameters and measured currents and voltages. The Park transformations and Clarke Transformations for PMSM voltages and currents can be expressed as:

$$\begin{cases} i_d = i_\alpha \cos\theta_{re} + i_\beta \sin\theta_{re} \\ i_q = -i_\alpha \sin\theta_{re} + i_\beta \cos\theta_{re} \\ v_d = v_\alpha \cos\theta_{re} + v_\beta \sin\theta_{re} \\ v_q = -v_\alpha \sin\theta_{re} + v_\beta \cos\theta_{re} \end{cases} \quad \text{and} \quad \begin{cases} i_\alpha = i_a \\ i_\beta = -i_b/\sqrt{3} + i_c/\sqrt{3} \\ v_\alpha = v_a \\ v_\beta = -v_b/\sqrt{3} + v_c/\sqrt{3} \end{cases} \tag{2.10}$$

By manipulating Equation (2.10) and the PMSM model (2.1), the rotor position can be calculated as:

$$\theta_{re} = \tan^{-1}\left(\frac{v_b - v_c - R_s(i_b - i_c) - L_d \frac{d(i_b - i_c)}{dt} - \sqrt{3}\omega_{re}(L_d - L_q)i_a}{\sqrt{3}(v_a - R_s i_a - L_d \frac{di_a}{dt}) + \omega_{re}(L_d - L_q)(i_b - i_c)} \right) \tag{2.11}$$

The accuracy of this method also strongly depends on the accuracy of the PMSM parameters and quality and accuracy of the voltage and current measurements. Since current derivatives also need to be calculated in every switching cycle, the rotor position is subjected to a high level of measurement noise.

***Remarks*:** The open-loop calculation-based PMSM rotor position estimation methods are straightforward and easy to implement. However, the resolution of the rotor position obtained by using these methods is limited by the numerical resolution, which depends on the sampling frequency and control-loop frequency of the control system. The accuracy of these methods strongly depends on the accuracy of the machine parameters and voltage and current measurements. These approaches are still useful but can be improved upon by using the closed-loop observers discussed in the next section.

2.2.3 Closed-Loop Observers

In a closed-loop observer, as illustrated in Figure 2.3, both the inputs of the plant (including the inverter and PMSM) and the error between the measured and estimated

outputs are used as the inputs to the observer. The proper selection of the observer parameters and design of an appropriate internal state adjustment scheme, which can be either linear or nonlinear, is important to ensuring the convergence of the observer outputs to the plant outputs and, consequently, the convergence of the estimated values of the states of interest to their actual values.

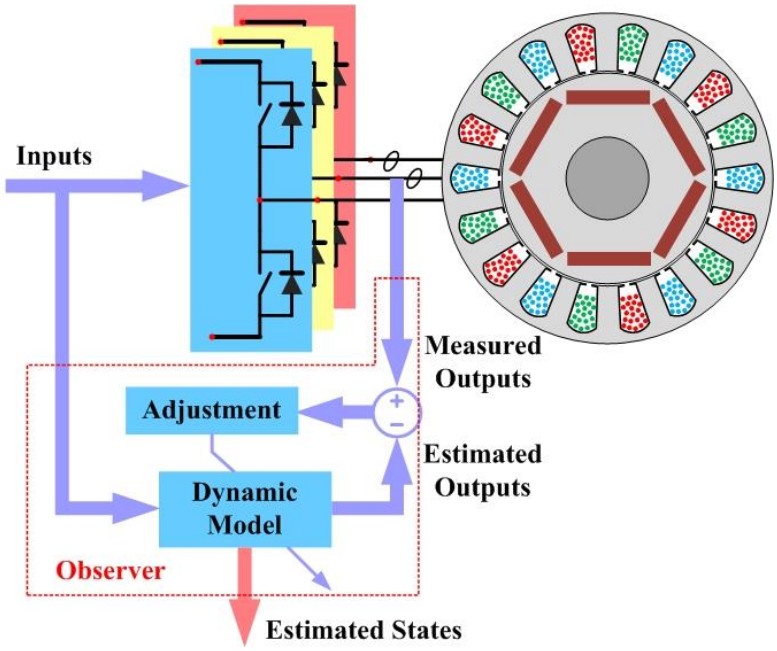

Figure 2.3: An illustration of the closed-loop observer for rotor position estimation.

The dynamic model of the PMSM is critical to the performance of the observer. According to Equations (2.1)-(2.5), the PMSM model can be expressed in either the stationary or the rotor reference frame. When using different models, the structures of the resultant observers will be different. Furthermore, numerous model-based position observers have been proposed in the literature which combine with different state adjustment schemes.

In this section, based on the nature of the internal state adjustment schemes, the representative closed-loop observers, including disturbance observer, SMO, and EKF, are reviewed. In addition, since most observers were designed to estimate the position related signals, e.g., EMF, EEMF, or flux, additional rotor position/speed extraction methods are needed. Therefore, a brief review of the position extraction methods is also presented.

2.2.3.1 Linear State Observers [44]–[48]

The EMF or EEMF components can be estimated by using linear state observers, e.g., disturbance observers, as shown in Figure 2.4(a), in which the EMF is regarded as a kind of disturbance voltage. For an SPMSM, rewriting Equation (2.3) yields:

$$\frac{d}{dt}\begin{bmatrix} i_\alpha \\ i_\beta \end{bmatrix} = \begin{bmatrix} -R_s/L & 0 \\ 0 & -R_s/L \end{bmatrix} \cdot \begin{bmatrix} i_\alpha \\ i_\beta \end{bmatrix} + \frac{1}{L} \cdot \left(\begin{bmatrix} v_\alpha \\ v_\beta \end{bmatrix} - \begin{bmatrix} e_\alpha \\ e_\beta \end{bmatrix} \right) \tag{2.12}$$

where $e = [e_\alpha \; e_\beta]^T = [-\omega_{re}\lambda_m \sin(\theta_{re}) \; \omega_{re}\lambda_m \cos(\theta_{re})]^T$ is the vector of the EMF components. In [44], based on the assumption that $de/dt \approx 0$, a disturbance observer was designed as:

$$\begin{aligned} \frac{d}{dt}\begin{bmatrix} \hat{i}_\alpha \\ \hat{i}_\beta \end{bmatrix} &= \begin{bmatrix} -R_s/L & 0 \\ 0 & -R_s/L \end{bmatrix} \cdot \begin{bmatrix} i_\alpha \\ i_\beta \end{bmatrix} + \frac{1}{L} \cdot \left(\begin{bmatrix} v_\alpha \\ v_\beta \end{bmatrix} - \begin{bmatrix} \hat{e}_\alpha \\ \hat{e}_\beta \end{bmatrix} \right) \\ \frac{d}{dt}\begin{bmatrix} \hat{e}_\alpha \\ \hat{e}_\beta \end{bmatrix} &= G \cdot \frac{d}{dt}\begin{bmatrix} \hat{i}_\alpha - i_\alpha \\ \hat{i}_\beta - i_\beta \end{bmatrix} \end{aligned} \tag{2.13}$$

where ^ denotes the estimated value and G is the observer gain matrix, which can be selected by using the pole assignment scheme to achieve the desired tracking performance. Based on the estimated back EMF, the rotor position can be obtained by $\hat{\theta}_{re} = \tan^{-1}\left(-\hat{e}_\alpha / \hat{e}_\beta\right)$.

For an IPMSM, linear state observers have been proposed for use with the EEMF model in the stationary [45] or rotor [46], [47] reference frame. In [45], the structure of the current observer is the same as that in Equation (2.13), but the expression for the EMF observer is slightly different:

$$\frac{d}{dt}\begin{bmatrix}\hat{e}_\alpha \\ \hat{e}_\beta\end{bmatrix} = A\begin{bmatrix}0 & -1 \\ 1 & 0\end{bmatrix}\begin{bmatrix}\hat{e}_\alpha \\ \hat{e}_\beta\end{bmatrix} + G\cdot\frac{d}{dt}\begin{bmatrix}\hat{i}_\alpha - i_\alpha \\ \hat{i}_\beta - i_\beta\end{bmatrix} \tag{2.14}$$

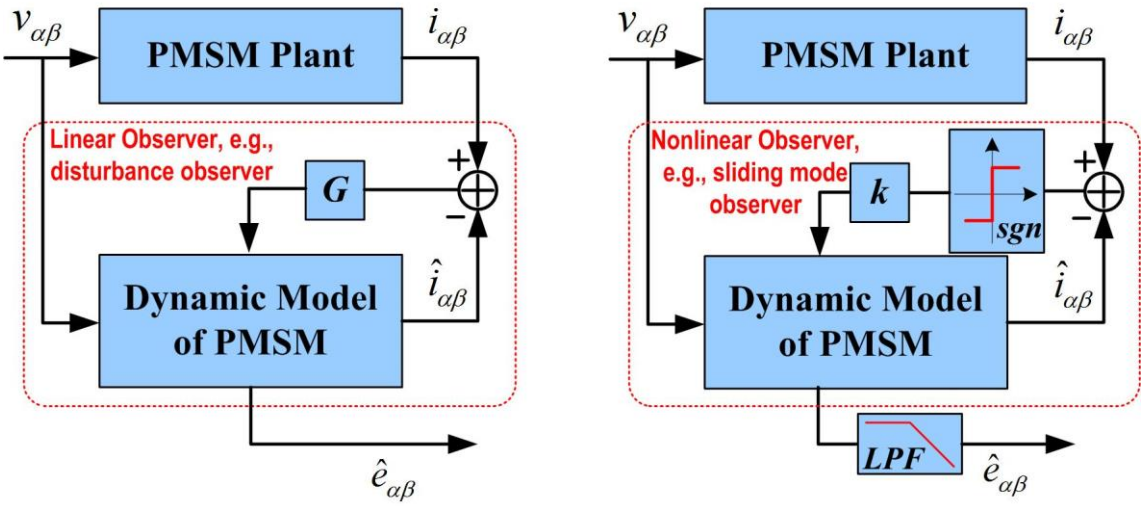

(a) (b)

Figure 2.4: Illustrations of (a) a linear observer, e.g., a disturbance observer; and (b) a nonlinear observer, e.g., an SMO, for back EMF estimation.

When using the PMSM model in the rotor reference frame, the estimated system state is usually the error between the actual and estimated rotor positions $\Delta\theta = \theta_{re} - \hat{\theta}_{re}$. In addition to these EMF-based observers, a state observer was designed in [48] to estimate the flux quantities. The stability of a disturbance observer can be guaranteed by the proper selection of the observer gains. Since the machine parameters are needed in the observers' models, the variations of those parameters will slightly affect the accuracy of

the position estimation, especially due to the cross-coupling effect between the *d*- and *q*-axes. Moreover, the quality of voltage and current measurements, e.g., the measurement noise and DC offset, could also affect the performance of the disturbance observers.

2.2.3.2 Nonlinear State Observers

As shown in Equations (2.13) and (2.14), the disturbance observers were designed based on the linear state space equations and using linear state feedback. In addition, nonlinear observers, which use nonlinear state feedback, are also effective candidates for the rotor position estimation. An SMO is a representative of the nonlinear observers.

An SMO is an observer whose inputs are discontinuous functions of the errors between the estimated and measured outputs. When the trajectories of the desired states reach the well-designed manifold, the sliding mode will be enforced. The dynamics of the desired states under the sliding mode depend only on the surfaces chosen in the state space and are not affected by system structure or parameter accuracy. Advantages such as high robustness to system structure and parameter variations make the SMO a promising solution for the rotor position estimation of PMSMs. In the literature, the SMOs were usually designed based on the PMSM models in the stationary reference frame and were rarely designed based on the PMSM models in the rotor reference frame. For an SPMSM, a typical SMO [49] was designed as:

$$\frac{d}{dt}\begin{bmatrix}\hat{i}_\alpha \\ \hat{i}_\beta\end{bmatrix}=\begin{bmatrix}-R_s/L & 0 \\ 0 & -R_s/L\end{bmatrix}\cdot\begin{bmatrix}\hat{i}_\alpha \\ \hat{i}_\beta\end{bmatrix}+\frac{1}{L}\begin{bmatrix}v_\alpha \\ v_\beta\end{bmatrix}-\left(1+l\frac{\omega_c}{s+\omega_c}\right)\cdot k\cdot\mathrm{sgn}\begin{bmatrix}\hat{i}_\alpha - i_\alpha \\ \hat{i}_\beta - i_\beta\end{bmatrix} \quad (2.15)$$

where ω_c is the cutoff frequency of the low-pass filter (LPF); sgn is the sign function; l is the observer feedback gain; and k is the gain of the switching terms. In this case, the

sliding surface is designed as $S = \left[\hat{i}_\alpha - i_\alpha \quad \hat{i}_\beta - i_\beta \right] = 0$. By properly selecting *l* and *k*, the candidate Lyapunov function $V = S^T \cdot S/2 > 0$ and $dV/dt < 0$ can be guaranteed, so as the observer stability. If the sliding mode is enforced, the back EMF components can be estimated by:

$$\begin{bmatrix} \hat{e}_\alpha \\ \hat{e}_\beta \end{bmatrix} = k(1+l) \cdot \frac{\omega_c}{s+\omega_c} \cdot \text{sgn} \begin{bmatrix} \hat{i}_\alpha - i_\alpha \\ \hat{i}_\beta - i_\beta \end{bmatrix} \tag{2.16}$$

Then the rotor position can be extracted from the estimated EMF components. The block diagram of an SMO-based back EMF estimator is shown in Figure 2.4(b). Many variations of Equation (2.15) can be found in the literature, e.g., using the saturation function [50] or the sigmoid function [51] to replace the sign function to mitigate the chattering problem. The design of the sliding surface can also be different. In addition, several online machine parameter adaption schemes [52] have also been proposed to improve the observer robustness to machine parameter variations. By using the EEMF model, Equation (2.5), in the stationary reference frame, the SMO-based methods can be applied to salient-pole PMSMs [52].

However, in practical applications, the attractive features of the SMO, such as robustness to machine parameters and operating conditions, will degrade if the system has a low sampling frequency and control-loop frequency. As discussed in [54], the performance of the SMO without oversampling is much worse than the case with oversampling. Compared with the disturbance observer, which is an example of linear state observers using a continuous linear state feedback, the SMO is a nonlinear observer using the output of a discontinuous switching function as the feedback. If switching gains are well tuned, the SMO will have better dynamic performance than the disturbance

observers. However, well-designed LPFs are needed in the SMO to mitigate the oscillating position errors due to the unwanted noise introduced by the switching functions. The phase delay caused by LPFs shall be compensated for carefully.

2.2.3.3 MRAS-Based Methods

The MRAS is an effective scheme for rotor speed estimation in motor drives. It can be used either as an independent speed observer or a speed extraction scheme working with other observers. The MRAS-based independent speed observers are discussed in this section. In an MRAS, as shown in Figure 2.5, an adjustable model and a reference model are connected in parallel. The output of the adjustable model is expected to converge with the output of the reference model under a proper adaption mechanism. Since estimated speed is one of the internal states of the adjustable model, the internal system states of these two models should be identical if the output of the adjustable model tracks that of the reference model well. In [55], [56], the reference model is formulated as:

$$\frac{d}{dt}\boldsymbol{x} = A\cdot\boldsymbol{x} + \boldsymbol{u} \tag{2.17}$$

where $\boldsymbol{x} = \begin{bmatrix} x_1 \\ x_2 \end{bmatrix} = \begin{bmatrix} i_d + \dfrac{\lambda_m}{L_d} \\ i_q \end{bmatrix}$, $\boldsymbol{u} = \begin{bmatrix} u_1 \\ u_2 \end{bmatrix} = \begin{bmatrix} \dfrac{\left(v_d L_d + \lambda_m\right)}{L_d^2} \\ \dfrac{v_q}{L_q} \end{bmatrix}$ and $A = \begin{bmatrix} -\dfrac{R_s}{L_d} & \dfrac{L_q\omega_{re}}{L_d} \\ -\dfrac{L_d\omega_{re}}{L_q} & -\dfrac{R_s}{L_q} \end{bmatrix}$. And

the adjustable model is defined as:

$$\frac{d}{dt}\hat{\boldsymbol{x}} = \hat{A}\cdot\hat{\boldsymbol{x}} + \boldsymbol{u} \tag{2.18}$$

where $\boldsymbol{x} = \begin{bmatrix} \hat{x}_1 \\ \hat{x}_2 \end{bmatrix}$ and $\hat{A} = \begin{bmatrix} -R_s/L_d & L_q\hat{\omega}_{re}/L_d \\ -L_d\hat{\omega}_{re}/L_q & -R_s/L_q \end{bmatrix}$. In the adjustable model, the estimated speed information is used as a corrective term in the estimation of matrix *A*. The adaptive mechanism for the speed update is expressed as:

$$\hat{\omega}_{re} = \int_0^t k_1 \left[i_d\hat{i}_q - i_q\hat{i}_d - \lambda_m\left(i_q - \hat{i}_q\right)/L_d \right] d\tau + k_2 \left[i_d\hat{i}_q - i_q\hat{i}_d - \lambda_m\left(i_q - \hat{i}_q\right)/L_d \right] + \omega_{re}(0) \quad (2.19)$$

The stability of the MRAS and the convergence of the speed estimation can be guaranteed by the Popov hyperstability theory [57], [58]. Per previous discussion, if the tracking errors between the states of the adjustable and reference models are close to zero, the estimated speed obtained by Equation (2.19) can be viewed as the actual speed. Then the rotor position can be obtained by using an integrator.

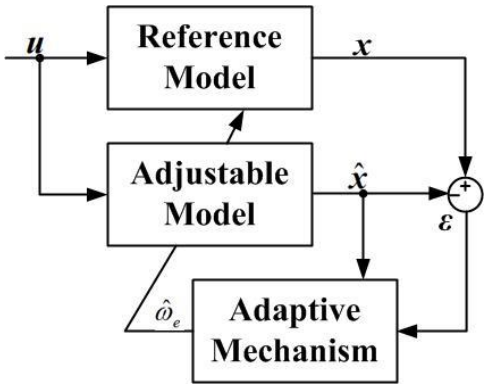

Figure 2.5: The schematic of an MRAS-based rotor speed estimator.

2.2.3.4 Extended Kalman Filter-Based Methods

As an extension of the Kalman filter, which is a stochastic state observer in the least-square sense, the EKF is a viable candidate for the online estimation of the rotor position and speed of a PMSM. In the EKF algorithm, the system state variables can be selected in either the rotor reference frame [59] or the stationary reference frame [60], i.e.,

$\boldsymbol{x} = [i_d\ i_q\ \omega_r\ \theta_{re}]^T$ and $\boldsymbol{x} = [i_\alpha\ i_\beta\ \omega_r\ \theta_{re}]^T$, respectively. A standard EKF algorithm contains three steps: prediction, innovation, and Kalman gain update. Due to the stochastic properties of the EKF, it has great advantages in the areas of robustness to measurement noise and the inaccuracy of machine parameters. However, tuning the covariance matrices of the model and measurement noise is difficult [59]. In addition, the EKF-based algorithms are computationally intensive and time consuming. This drawback makes the EKF hard to implement in industrial drives.

***Remarks*:** Several widely used, closed-loop observers have been discussed in this section. Generally speaking, based on the PMSM model in the stationary reference frame, both linear and nonlinear observers can be utilized to estimate the position-related signals, e.g., the EMF components or flux, from which the rotor position can be extracted. However, due to the alternating, i.e., sinusoidal, nature of the quantities in the stationary reference frame, the delays caused by the observers must be carefully handled. When using the PMSM model in the rotor reference frame, the linear state observers are usually utilized. The observer output is usually an error signal between the estimated and actual rotor positions. An additional observer is required to extract the rotor position from the error signal obtained. When using the MRAS or EKF methods, if properly designed, either the rotor position or the rotor speed can be directly estimated. However, the stability issue and computational cost of these position/speed estimators should be considered in the design stage.

2.2.3.5 Rotor Position/Speed Estimators

Per previous discussions, in most closed-loop, observer-based rotor position/speed estimation methods, the position/speed related states, such as the EMF components or flux, were estimated first. The rotor position and speed information was then extracted from these estimated states using an appropriate observer or algorithm. If two orthogonal signals, e.g., the estimated EMF components $\hat{e}_\alpha$ and $\hat{e}_\beta$ in Equation (2.13), are obtained, the simplest and most straightforward approach to calculate the rotor position is the use of an arctangent algorithm [49]. However, this is an open-loop method, which is quite sensitive to input noise. In addition, if the output of the observer is a position estimation error signal, the arctangent algorithm cannot be utilized.

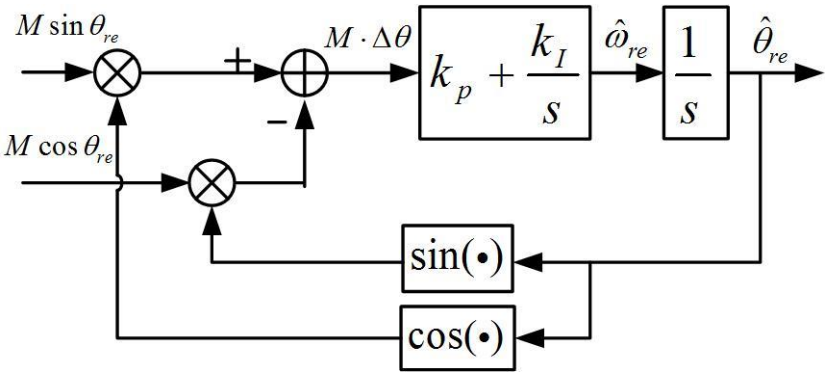

Figure 2.6: The block diagram of a PLL-based position extraction method.

Besides the arctangent algorithm, the phase-locked loop (PLL) and the angle tracking observer [61] are also effective methods. A typical PLL-based position extraction method is shown in Figure 2.6, where $M\sin\theta_{re}$ and $M\cos\theta_{re}$ are two orthogonal input signals, e.g., the estimated EMF components, where M is the amplitude of the

signals. If the difference between the estimated and actual rotor positions is small, the following relationship can be obtained:

$$M\sin\theta_{re}\cos\hat{\theta}_{re} - M\cos\theta_{re}\sin\hat{\theta}_{re} = M\sin\left(\theta_{re} - \hat{\theta}_{re}\right) \approx M\Delta\theta \tag{2.20}$$

Based on $M\Delta\theta$, a proportional-integral (PI) regulator can be designed to estimate the rotor speed. Then the rotor position can be obtained by using an integrator. The transfer function of the PLL can be expressed as:

$$\frac{\hat{\theta}_{re}}{\theta_{re}} = \frac{k_p s + k_i}{s^2 + k_p s + k_i} \tag{2.21}$$

The dynamic behavior of Equation (2.21) depends on the PI gains, which can be determined by appropriately placing the poles of the characteristic polynomial of Equation (2.21). If the output of the observer is already a function of $\Delta\theta$, it can be used directly by the PLL as an equivalent term to $M\Delta\theta$. To improve the position/speed estimation performance, a higher order speed regulator, $G(s)$, was utilized in [46], which was expressed as $G(s) = k_1 + \frac{k_2}{s} + \frac{k_3}{s^2}$. Besides Equation (2.21), the performance of the PLL can be improved by using a saliency observer, presented in [47], [62].

In addition to the PLL, the MRAS has also been utilized to extract rotor speed information from estimated orthogonal signals. For example, an MRAS-based rotor speed estimator was proposed in [63], as illustrated in Figure 2.7. In this estimator, an SMO is properly designed to estimate the back EMF components $\hat{e}_{\alpha\beta} = [\hat{e}_\alpha, \hat{e}_\beta]^T$ in the stationary reference frame, which provides a reference model in the MRAS. If the rotor speed changes slowly, i.e., $d\omega_{re}/dt \approx 0$, which is true when a PMSM operates in the medium- and high-speed regions, the derivatives of $\hat{e}_\alpha$ and $\hat{e}_\beta$ can be calculated as:

$$\dot{\hat{e}}_{\alpha\beta} = \omega_{re} \underbrace{\begin{bmatrix} 0 & -1 \\ 1 & 0 \end{bmatrix}}_{J} \cdot \hat{e}_{\alpha\beta} \tag{2.22}$$

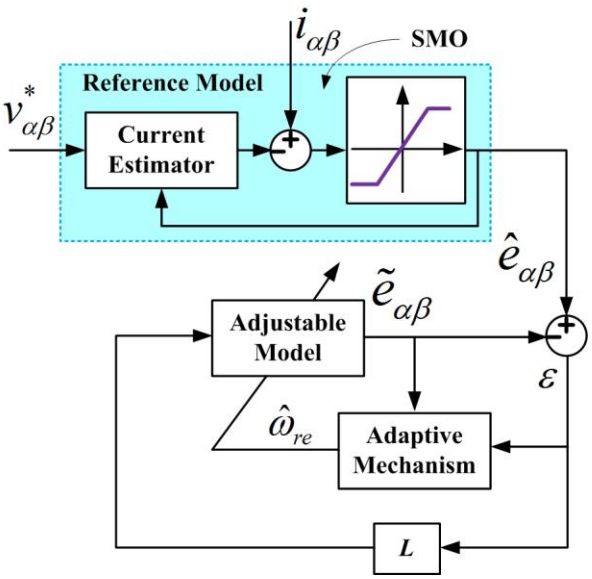

Figure 2.7: Block diagram of a MRAS-based rotor speed estimator.

The adjustable model was then designed in the same form of Equation (2.22) as follows:

$$\dot{\tilde{e}}_{\alpha\beta} = \hat{\omega}_{re} J \cdot \tilde{e}_{\alpha\beta} + L \cdot \left(\hat{e}_{\alpha\beta} - \tilde{e}_{\alpha\beta} \right) \tag{2.23}$$

where $\tilde{e}_{\alpha\beta} = [\tilde{e}_{\alpha}, \tilde{e}_{\beta}]^T$ is the output vector of the adjustable model, which is also a vector of the estimated EMF components; $\hat{\omega}_{re}$ is the estimated rotor electrical speed, which is the output of the adaptive mechanism; and **L** is the MRAS gain matrix, which can be configured by using a linear observer design technique, e.g., pole assignment [44]. In practical applications, the off-diagonal elements of **L** can be set to be zero [44] to

simplify the design procedure. Based on the outputs of the adjustable model and the reference model, the rotor speed can be estimated by using a PI regulator as follows:

$$\hat{\omega}_{re} = \left(k_p + \frac{k_i}{s} \right) \left[\left(\hat{e}_{\alpha\beta} - \tilde{e}_{\alpha\beta} \right)^T \cdot J \cdot \tilde{e}_{\alpha\beta} \right] \tag{2.24}$$

2.3 Saliency-Based Methods

In Section 2.2, the fundamental frequency model-based rotor position/speed estimation techniques for PMSMs are reviewed. These methods are capable of providing highly accurate position/speed estimations for the vector control of PMSMs in medium- and high-speed regions. However, these methods will have poor performance or even fail in the low-speed region and at standstill due to low signal-to-noise ratios (SNRs) of the position-related system states. To overcome this limitation and improve the low-speed operation capability, rotor position/speed estimation methods using machine saliency tracking [64], [65] have been extensively studied. In these methods, an HF excitation, whose frequency is much higher than the fundamental frequency, is usually utilized. Using the measured response of the PMSM under the HF excitation, the position-related saliency signal can be obtained. The HF excitation-based methods can be characterized from the following three aspects.

- *The principle of the machine saliency tracking-based rotor position estimation*. For salient-pole PMSMs, e.g., the IPMSMs [66], the rotor position can be detected by tracking the variation of the position-dependent stator inductance. For the nonsalient-pole PMSMs, e.g., SPMSMs, which have symmetric rotor structures and, therefore, a

nearly zero spatial variation of inductance, the main flux saturation or stator leakage flux saturation-related spatial saliency [67], [68], is usually used for rotor position detection.

- *The method for HF excitation.* Both continuous [69]-[72] and discontinuous [73], [74] HF excitations have been proposed. Different types of HF excitation can be achieved by using either a carrier signal injection [70]-[72] or a pulse-width modulation (PWM) pattern modification [73]. For the carrier signal injection, both sinusoidal waveforms [69]-[71] and square waveforms [72] are available candidates; and they can be injected into either the stationary reference frame or the estimated synchronously rotating reference frame.
- *The signal processing method and saliency tracking observer*. For different types of HF excitation, the saliency-related signals measured could be different; and the signal processing methods used for different saliency-related signals could also vary. To improve rotor position detection performance, closed-loop saliency-tracking observers [75], [76] have been extensively studied in recent years.

In the remainder of this subsection, the dynamic models of the PMSMs under HF excitations are discussed first. Then a brief review of the HF excitation methods and signal processing procedures is presented.

2.3.1 High-Frequency Models of PMSMs

The HF model of a PMSM, i.e., the dynamics of a PMSM under an HF excitation, can be derived based on the fundamental frequency model, Equation (2.1), of the PMSM expressed in a *dq* rotor reference frame. Considering that the HF voltage signals, $v_{d,h}$ and $v_{q,h}$, whose frequency is sufficiently higher than the electrical rotating frequency of the PMSM, are injected into the PMSM stator windings, HF currents, $i_{d,h}$ and $i_{q,h}$, will be generated. To reduce extra losses, vibration, and acoustic noise caused by the HF excitation during normal operation of the drive system, the amplitudes of the injected voltage signals are usually much smaller than those of the fundamental stator voltages, such as the induced currents. However, due to the high frequency, the derivatives of the induced currents can be quite large. Therefore, when considering the HF components while the PMSM is operating in the low-speed region or is at standstill, the off-diagonal cross-coupling terms in Equation (2.1) are much smaller than the diagonal terms and, therefore, can be ignored. Similarly, in the low-speed region or at standstill, the back EMF term can also be neglected. Consequently, the HF model of the PMSM in the low-speed region and at standstill can be expressed as:

$$\begin{bmatrix} v_{d,h} \\ v_{q,h} \end{bmatrix} = \begin{bmatrix} L_d & 0 \\ 0 & L_q \end{bmatrix} \cdot p \begin{bmatrix} i_{d,h} \\ i_{q,h} \end{bmatrix} \tag{2.25}$$

At the early stage of the research for the saliency-based rotor position estimation, most studies assumed a pure inductive behavior of the PMSM, as shown in Equation (2.25). However, it has been already shown that the HF resistance, both in the stator and in the rotor [77], and the eddy current effects [78] are not always negligible. To take these

effects into account, the following HF impedance-based PMSM model [71] has been proposed.

$$\begin{bmatrix} v_{d,h} \\ v_{q,h} \end{bmatrix} = \begin{bmatrix} Z_{d,h} & 0 \\ 0 & Z_{q,h} \end{bmatrix} \begin{bmatrix} i_{d,h} \\ i_{q,h} \end{bmatrix} \tag{2.26}$$

where $Z_{d,h} \approx v_{d,h}/i_{d,h} = R_{d,h} + j\omega_h \cdot L_d$ and $Z_{q,h} \approx v_{q,h}/i_{q,h} = R_{q,h} + j\omega_h \cdot L_q$ are the *d*-axis and *q*-axis HF impedances, respectively; ω_h is the frequency of the injected signals; and $R_{d,h}$ and $R_{q,h}$ are the *d*-axis and *q*-axis HF resistances, respectively.

Similarly, the HF model of a PMSM expressed in the stationary reference frame can be derived based on the fundamental frequency model of PMSM, Equation (2.2), as follows.

$$\begin{bmatrix} v_\alpha \\ v_\beta \end{bmatrix} = \begin{bmatrix} L + \Delta L \cos(2\theta_{re}) & \Delta L \sin\theta_{re} \\ \Delta L \sin\theta_{re} & L - \Delta L \cos(2\theta_{re}) \end{bmatrix} \cdot p \begin{bmatrix} i_{\alpha,h} \\ i_{\beta,h} \end{bmatrix} = \mathbf{L_h} \cdot p \begin{bmatrix} i_{\alpha,h} \\ i_{\beta,h} \end{bmatrix} \tag{2.27}$$

where $\mathbf{L_h}$ is defined as the HF inductance matrix.

2.3.2 Methods of High-Frequency Excitation

The methods of HF excitation can be generally classified into two major categories: continuous and discontinuous. Due to the highly accurate position estimation and the capability of continuous position estimation, the continuous excitation is the dominant method for the HF excitation. However, discontinuous excitation methods, e.g., "Indirect Flux Detection by On-line Reactance Measurement (INFORM)" [79], were investigated during the past two decades. This method can be implemented in a low-cost DSP, which leads to an economic drive solution. The basic idea of the INFORM method is to measure the current response to the voltage space phasors applied in different

directions. This method can be implemented by using a PWM pattern modification and needs additional *di*/*dt* sensors. The position estimation accuracy of the INFORM method is in the range of 3–15 electric degrees, which is not acceptable for high-performance drives. The accuracy could be improved by using the optimized INFORM method [73].

For continuous HF excitation, the carrier signal injection-based methods are the most widely used. Both HF voltage and current signals can be injected. However, due to the utilization of VSIs and the limited control bandwidth of current regulators, the HF current injection-based methods [80] are rarely used. In the HF voltage signal injection-based methods, a sinusoidal or square-wave voltage vector can be injected into either the estimated rotor reference frame or the stationary reference frame.

2.3.2.1 Signal Injection in the Estimated Rotor Reference Frame

An HF sinusoidal voltage vector, also called a pulsating voltage vector, injected into the estimated $\gamma\delta$ rotor reference frame [98] can be expressed as

$$v_{\gamma\delta,h} = \begin{bmatrix} v_{\gamma,h} \\ v_{\delta,h} \end{bmatrix} = V_h \begin{bmatrix} \cos(\omega_h t) \\ 0 \end{bmatrix} \tag{2.28}$$

where ω_h and V_h are the frequency and amplitude of the injected voltage vector. The definition of estimated $\gamma\delta$ rotor reference frame is shown in Figure 2.8. The angle between the γ-axis and the α-axis, which is aligned with the direction of the phase *a* magnetic axis, is defined as the estimated rotor position. The error between the actual and estimated rotor positions is denoted as $\Delta\theta$.

Projecting $v_{\gamma\delta,h}$ onto the *d*- and *q*-axes, the resulting voltage vector, $v_{dq,h}$, can be expressed as:

$$v_{dq,h} = \begin{bmatrix} v_{d,h} \\ v_{q,h} \end{bmatrix} = \begin{bmatrix} \cos(\Delta\theta) & \sin(\Delta\theta) \\ -\sin(\Delta\theta) & \cos(\Delta\theta) \end{bmatrix} \begin{bmatrix} v_{\gamma,h} \\ v_{\delta,h} \end{bmatrix} = v_{\gamma,h} \begin{bmatrix} \cos(\Delta\theta) \\ -\sin(\Delta\theta) \end{bmatrix} \tag{2.29}$$

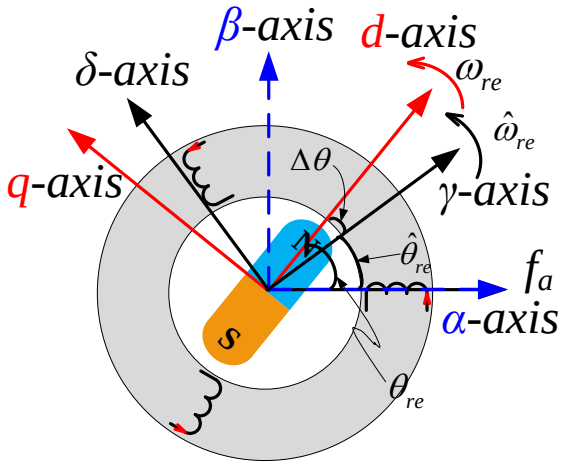

Figure 2.8: Relationships among the $\alpha\beta$ stationary reference frame, the ideal dq rotor reference frame, and the estimated $\gamma\delta$ rotor reference frame.

Then the HF model, Equation (2.25), can be used to derive the expression of the induced HF currents for rotor position estimation. According to Equations (2.25) and (2.29), the induced HF currents in the ideal dq reference frame can be determined by

$$i_{dq,h} = \begin{bmatrix} i_{d,h} \\ i_{q,h} \end{bmatrix} = \int \begin{bmatrix} v_{\gamma,h}\cos(\Delta\theta)/(L_d) \\ -v_{\gamma,h}\sin(\Delta\theta)/(L_q) \end{bmatrix} dt \tag{2.30}$$

Then the saliency signal can be extracted from the induced HF current signals in the $\gamma\delta$ reference frame as follows:

$$i_{\gamma\delta,h} = \begin{bmatrix} i_{\gamma,h} \\ i_{\delta,h} \end{bmatrix} = \begin{bmatrix} \cos(\Delta\theta) & -\sin(\Delta\theta) \\ \sin(\Delta\theta) & \cos(\Delta\theta) \end{bmatrix} \begin{bmatrix} i_{d,h} \\ i_{q,h} \end{bmatrix} = \frac{V_h \sin(\omega_h t)}{\omega_h} \begin{bmatrix} \frac{\cos^2(\Delta\theta)}{L_d} + \frac{\sin^2(\Delta\theta)}{L_q} \\ \frac{(L_q - L_d)}{2L_d L_q}\sin(2\Delta\theta) \end{bmatrix} \tag{2.31}$$

As shown in Equation (2.28), the pulsating voltage vector is equivalent to a sinusoidal signal injected into the γ axis. A study of injecting a sinusoidal voltage signal into the δ axis is presented in [82].

2.3.2.2 Signal Injection in the Stationary Reference Frame

An HF sinusoidal voltage vector, which is also called a rotating voltage vector, injected into the $\alpha\beta$ stationary reference frame can be expressed as

$$v_{\alpha\beta,h} = \begin{bmatrix} v_{\alpha,h} \\ v_{\beta,h} \end{bmatrix} = V_h \begin{bmatrix} -\sin\omega_h t \\ \cos\omega_h t \end{bmatrix} \tag{2.32}$$

where ω_h and V_h are the frequency and amplitude of the injected voltage vector. According to Equation (2.27), the induced HF currents in the $\alpha\beta$ stationary reference frame can be calculated as:

$$i_{\alpha\beta,h} = \begin{bmatrix} i_{\alpha,h} \\ i_{\beta,h} \end{bmatrix} = \int \left(\mathbf{L_h}^{-1} \cdot \begin{bmatrix} v_{\alpha,h} \\ v_{\beta,h} \end{bmatrix} \right) dt \tag{2.33}$$

Substituting Equation (2.32) into Equation (2.33) yields:

$$i_{\alpha\beta,h} = \begin{bmatrix} i_{\alpha,h} \\ i_{\beta,h} \end{bmatrix} = \frac{V_h}{L^2 - \Delta L^2} \begin{bmatrix} \frac{L}{\omega_h}\cos\omega_h t + \frac{\Delta L}{2\omega_{re} - \omega_h}\cos\left(2\theta_{re} - \omega_h t\right) \\ \frac{L}{\omega_h}\sin\omega_h t + \frac{\Delta L}{2\omega_{re} - \omega_h}\sin\left(2\theta_{re} - \omega_h t\right) \end{bmatrix} \tag{2.34}$$

As shown in Equation (2.34), the saliency signal can be extracted from the induced $i_{\alpha\beta,h}$. Similar to Equation (2.31), it is important to observe that the magnitude of the saliency signal contained in the induced HF currents depends on the difference of the HF inductance ΔL.

Recently, a method of injecting a pulsating voltage vector into the stationary reference frame has been presented in [81]. In addition to the sinusoidal HF signals, a HF square-wave voltage vector is also an effective candidate carrier signal, as presented in [72] and [81].

2.3.3 Signal Processing Methods

In most industrial PMSM drive systems, two or three current transducers are required to measure the stator phase currents. The aforementioned saliency-based methods are compatible with the existing drive systems, and no extra current or voltage sensors are required. However, other methods based on the zero-sequence voltage [65] would require extra voltage sensors.

The overall block diagram of a sensorless PMSM drive system using an HF carrier signal injection-based method is illustrated in Figure 2.9. The HF carrier signals can be injected either into the stationary reference frame or the estimated rotor reference frame. In Figure 2.9, the HF carrier signal is injected into the stationary reference frame. When the measured i_a and i_b are transformed into the values in the stationary reference frame, both the fundamental ($i_{\alpha\beta}$) and HF ($i_{\alpha\beta,h}$) components exist. An LPF is utilized to extract $i_{\alpha\beta}$, which is further used for current regulation. According to Equation (2.34), the saliency signal can be extracted from the induced $i_{\alpha\beta,h}$. Therefore, a proper signal processing method and rotor position estimation scheme should be designed to extract the rotor position information from the combination of $i_{\alpha\beta}$ and $i_{\alpha\beta,h}$.

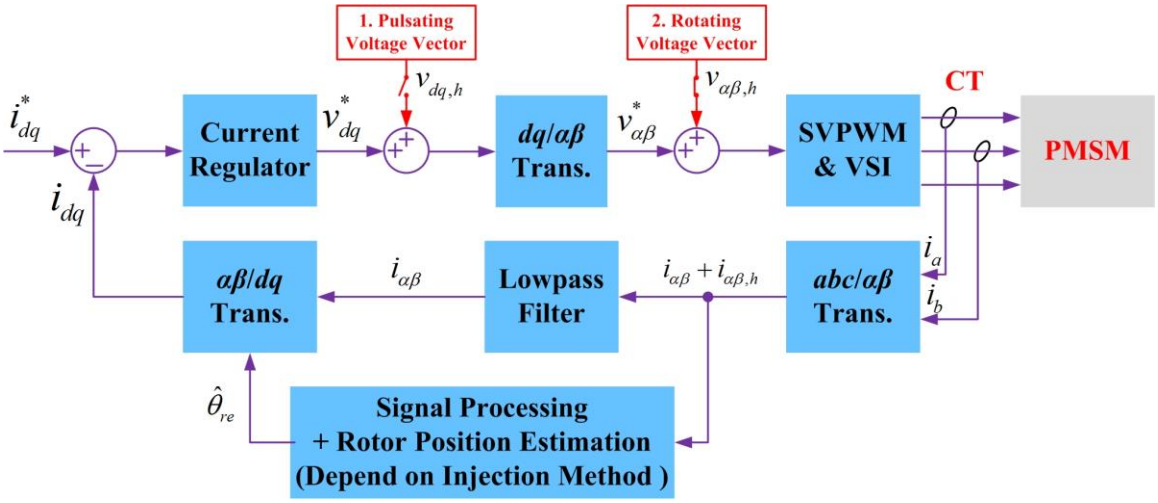

Figure 2.9 Overall block diagram of a sensorless PMSM drive system using an HF signal injection-based method.

Both a high-pass filter and a band-pass filter can be used to obtain $i_{\alpha\beta,h}$. Then, the most effective method to obtain the saliency signal from $i_{\alpha\beta,h}$ is heterodyning, which is similar to Equation (2.20). First, simply denote Equation (2.34) as

$$i_{\alpha\beta,h} = \begin{bmatrix} i_{\alpha,h} \\ i_{\beta,h} \end{bmatrix} = \begin{bmatrix} M_0 \cos\omega_h t + M_1 \cos\left(2\theta_{re} - \omega_h t\right) \\ M_0 \sin\omega_h t + M_1 \sin\left(2\theta_{re} - \omega_h t\right) \end{bmatrix}$$

Then the method via heterodyning can be expressed as

$$i_{\beta,h}\cos\left(2\hat{\theta}_{re} - \omega_h t\right) - i_{\alpha,h}\sin\left(2\hat{\theta}_{re} - \omega_h t\right) = M_0 \sin\left(2\hat{\theta}_{re} - 2\omega_h t\right) + M_1 \sin\left(2\theta_{re} - 2\hat{\theta}_{re}\right) \quad (2.35)$$

The first term on the right-hand side is a HF sinusoidal component, whose frequency is twice the ω_h. The second term on the right-hand side is the saliency signal, which contains information on the rotor position estimation error $\theta_{re} - \hat{\theta}_{re}$. Compared to the first term, the second term can be viewed as a DC component and, therefore, can easily be obtained by using an LPF. With the position estimation error, the PLL or the

saliency tracking observer presented in Section **2.2.3.5** can be utilized to obtain rotor position information.

Similarly, if the HF signal is injected into the estimated rotor reference frame, according to Equation (2.31), the saliency signal can be extracted from $i_{\delta,h}$. By multiplying it with $\sin(\omega_h t)$, the following expression can be obtained:

$$i_{\delta,h}\sin\left(\omega_h t\right)=\frac{\Delta L}{L_d L_q}\frac{V_h\sin^2\left(\omega_h t\right)}{\omega}\sin(2\Delta\theta)=\frac{V_h\Delta L}{2\omega L_d L_q}\sin(2\Delta\theta)-\frac{V_h\Delta L}{2\omega L_d L_q}\sin(2\Delta\theta)\cos\left(2\omega_h t\right) \quad (2.36)$$

Similar to Equation (2.35), the first term on the right-hand side of Equation (2.36) can be easily obtained by using an LPF. Since this term contains the rotor position estimation error, the PLL or the saliency tracking observer presented in Section **2.2.3.5** can be utilized to obtain the rotor position information.

***Remarks*:** A brief literature review on the saliency-based methods using HF excitation is presented in this section. This technique is effective for a PMSM operating in low-speed and standstill conditions, where the magnitude of the back EMF is extremely low. The accuracy of these methods depends strictly on the machine saliency. In addition, in practical applications, the machine inductance saturation, eddy current loss, cross-coupling effect between *d*- and *q*-axes, and inverter nonlinearities will cause considerable error in the rotor position detection.

CHAPTER 3

QUASI-SLIDING-MODE-OBSERVER-BASED ROTOR POSITION/SPEED ESTIMATORS FOR SENSORLESS CONTROL OF SALIENT-POLE PMSMSs

In this chapter, based on different machine models, multiple quasi-sliding-mode observer (QSMO)-based rotor position/speed estimators are proposed for sensorless control of salient-pole PMSMs. First, a mathematical model reconstruction method is proposed to obtain suitable dynamic models for salient-pole PMSMs, which are further used for position observation. Then, based on the reconstructed model, QSMOs are proposed to estimate the position-related quantities, i.e., extended EMF and extended flux. The implementation of the QSMO-based position/speed estimators is also illustrated in this chapter.

3.1 Model Reconstruction for Salient-Pole PMSMs

Due to the machine rotor saliency, the rotor position estimation algorithm for a salient-pole PMSM is generally more complex than that for a nonsalient-pole PMSM. To perform the model-based rotor position estimation for salient-pole PMSMs, several reconstructed EMF- or flux-based machine models have been developed. The "extended EMF (EEMF)" model [45], [46] is the most widely used one, in which the saliency-related voltage terms are converted into the EMF terms. The EEMF is then formed to be a summation of the saliency-related EMF terms and the original back EMF terms. In the

EEMF model, i.e., Equation (2.5), only the EEMF components contain the rotor position information. However, since the magnitude of the EEMF components depends on the machine operating conditions, the dynamic performance of an EEMF-based position estimator may degrade during an abrupt change in the operating conditions. Moreover, since the EEMF model needs information on rotor speed and machine parameters, i.e., stator resistance and inductances, it is difficult to design an observer, which is robust to both load condition variations and machine parameter uncertainties. In addition to the EEMF-based model, models reconstructed based on the flux concept, e.g., the "fictitious flux" model [83] and the "active flux" model [84], provide alternatives to mathematically convert a salient-pole PMSM model into an equivalent nonsalient-pole PMSM model. In the flux-model-based rotor position estimation, an integrator is normally required to calculate the flux. In this case, some practical issues, e.g., current sensor DC offset, integrator DC offset, and initial condition, should be carefully handled.

In this section, reconstruction process for a mathematical model is proposed for the dynamic modeling of a generic salient-pole PMSM. By reconstructing the machine model using the voltage concept, the EEMF-based model can be obtained. By reconstructing the machine model using the flux concept, a new extended flux-based salient-pole PMSM model is derived. Compared to the EEMF model, the extended flux model has the advantages of simpler structure, independence of rotor speed, and less sensitivity to machine parameter variations.

3.1.1 Dynamic Model of a Salient-Pole PMSM

The dynamics of a salient-pole PMSM can be modeled in the *dq* rotor reference frame as in Equation (2.1). Using the inverse Park transformation, the salient-pole PMSM model in the $\alpha\beta$ stationary reference frame can be expressed as Equation (2.2). Due to the difference between L_d and L_q caused by machine rotor saliency, both θ_{re} and $2\theta_{re}$ terms appear in Equation (2.2). Therefore, it is difficult to use Equation (2.2) directly for rotor position observation. A reconstruction of Equation (2.2) is needed to facilitate the rotor position observation for a salient-pole PMSM.

In this chapter, the mathematical reconstruction of the salient-pole PMSM model starts from a voltage/flux model as follows:

$$\begin{aligned} v_\alpha &= R_s i_\alpha + \overbrace{L_d\, p\left(i_d \cos(\theta_{re})\right) - L_q\, p\left(i_q \sin(\theta_{re})\right) + \lambda_m\, p\left(\cos(\theta_{re})\right)}^{p(\lambda_\alpha)} \\ v_\beta &= R_s i_\beta + \underbrace{L_d\, p\left(i_d \sin(\theta_{re})\right) + L_q\, p\left(i_q \cos(\theta_{re})\right) + \lambda_m\, p\left(\sin(\theta_{re})\right)}_{p(\lambda_\beta)} \end{aligned} \tag{3.1}$$

Equation (3.1), which models the voltage/flux dynamics of the PMSM in the stationary reference frame, contains the voltage terms (v_α and v_β) in the stationary reference frame and the derivatives of the flux terms ($p\lambda_\alpha$ and $p\lambda_\beta$) expressed with quantities in the *dq* rotor reference frame. In Equation (3.1), only the θ_{re}-related terms are present; and each term has clear physical meaning, as shown in Figure 3.1. Rearranging Equation (3.1), the following equations can be obtained:

$$\begin{bmatrix} v_\alpha \\ v_\beta \end{bmatrix} = R_s \begin{bmatrix} i_\alpha \\ i_\beta \end{bmatrix} + p \begin{bmatrix} L & 0 \\ 0 & L \end{bmatrix} \begin{bmatrix} i_\alpha \\ i_\beta \end{bmatrix} + \underbrace{\Delta L p \left(\begin{bmatrix} \cos\theta_{re} & \sin\theta_{re} \\ \sin\theta_{re} & -\cos\theta_{re} \end{bmatrix} \begin{bmatrix} i_d \\ i_q \end{bmatrix} \right) + \omega_{re}\lambda_m \begin{bmatrix} -\sin\theta_{re} \\ \cos\theta_{re} \end{bmatrix}}_{\text{Position Related Terms } V(\theta_{re})} \quad (3.2)$$

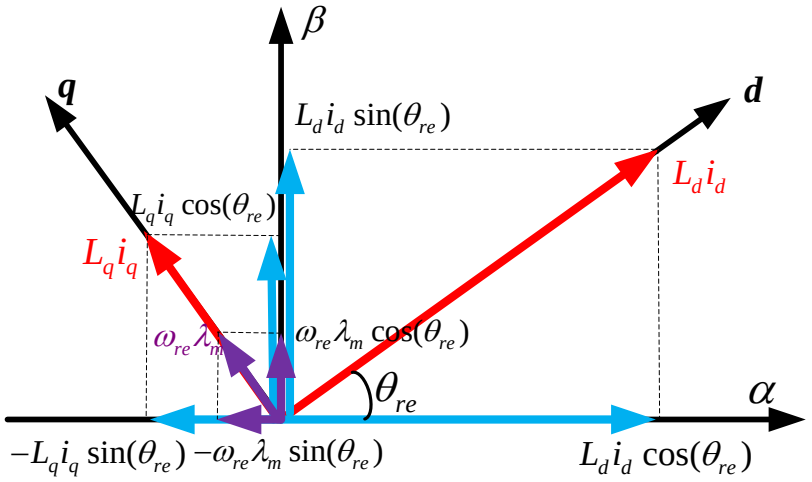

Figure 3.1: Illustration of the salient-pole PMSM model (Equation (3.1)).

3.1.2 Idea of Model Reconstruction

To facilitate the rotor position observation, the objective of reconstructing the model (Equation (3.1)) is to achieve a similar symmetrical model structure, which contains a symmetrical inductance matrix as for the nonsalient-pole PMSMs, as follows:

$$\begin{aligned} \begin{bmatrix} v_\alpha \\ v_\beta \end{bmatrix} &= R_s \begin{bmatrix} i_\alpha \\ i_\beta \end{bmatrix} + p \begin{bmatrix} L_s & 0 \\ 0 & L_s \end{bmatrix} \begin{bmatrix} i_\alpha \\ i_\beta \end{bmatrix} + \omega_{re}\lambda_m \begin{bmatrix} -\sin\theta_{re} \\ \cos\theta_{re} \end{bmatrix} \\ &= R_s \begin{bmatrix} i_\alpha \\ i_\beta \end{bmatrix} + p \begin{bmatrix} L_s & 0 \\ 0 & L_s \end{bmatrix} \begin{bmatrix} i_\alpha \\ i_\beta \end{bmatrix} + p \begin{bmatrix} \lambda_m \cos\theta_{re} \\ \lambda_m \sin\theta_{re} \end{bmatrix} \end{aligned} \quad (3.3)$$

In Equation (3.3), the $\sin(\theta_{re})$- and $\cos(\theta_{re})$-related terms are presented separately in each equation. However, in Equation (3.2), both the $\sin(\theta_{re})$- and $\cos(\theta_{re})$-related terms

are presented simultaneously in each equation. Therefore, further model reconstruction is required for Equation (3.2) to achieve a similar model structure as Equation (3.3). As shown in Equation (3.3), the EMF term can be either written in the form of voltage, i.e., $\omega_{re}\lambda_m[-\sin(\theta_{re}),\ \cos(\theta_{re})]^T$, or in the form of a derivative of flux, i.e., $p[\lambda_m\cos(\theta_{re}),\ \lambda_m\sin(\theta_{re})]^T$. Similarly, Equation (3.2) can be further reconstructed in either a voltage (EMF) form or a flux form.

3.1.3 Model Reconstruction Based on Voltage Concept

Consider the last two terms of Equation (3.2), as follows, which are position related:

$$V(\theta_{re}) = \begin{bmatrix} \Delta L p\left(i_d \cos\theta_{re} + i_q \sin\theta_{re}\right) - \omega_{re}\lambda_m \sin\theta_{re} \\ \Delta L p\left(i_d \sin\theta_{re} - i_q \cos\theta_{re}\right) + \omega_{re}\lambda_m \cos\theta_{re} \end{bmatrix} \tag{3.4-1}$$

By applying the following inverse Park transformation to the currents:

$$\begin{cases} i_\alpha = i_d \cos\theta_{re} - i_q \sin\theta_{re} \\ i_\beta = i_d \sin\theta_{re} + i_q \cos\theta_{re} \end{cases} \tag{3.4-2}$$

Equation (3.4-1) can be reconstructed into the following form:

$$V(\theta_{re}) = \begin{bmatrix} \Delta L p\left(i_\alpha + 2i_q \sin\theta_{re}\right) - \omega_{re}\lambda_m \sin\theta_{re} \\ \Delta L p\left(i_\beta - 2i_q \cos\theta_{re}\right) + \omega_{re}\lambda_m \cos\theta_{re} \end{bmatrix} \tag{3.4-3}$$

In Equation (3.4-3), the $\sin(\theta_{re})$- and $\cos(\theta_{re})$-related terms are presented separately in each equation. However, both voltage terms, e.g., $\omega_{re}\lambda_m\sin(\theta_{re})$, and a derivative of flux terms, e.g., $p(\Delta L i_q \sin(\theta_{re}))$, are still presented in each equation. Since $\sin(\theta_{re})$ and its derivative cannot be combined directly, neither $\cos(\theta_{re})$ and its derivative,

the derivative of flux terms, e.g., $p(\Delta L i_q \sin(\theta_{re}))$, need to be converted into voltage terms in order to complete the reconstruction of Equation (3.4-3) into the voltage form.

Applying Equation (3.4-2) two more times to Equation (3.4-3), the following equations can be obtained:

$$\begin{aligned} V(\theta_{re}) &= \begin{bmatrix} \Delta L p(i_\alpha) + 2\omega_{re}\Delta L i_q \cos\theta_{re} - \left(\omega_{re}\lambda_m - 2\Delta L p(i_q)\right)\sin\theta_{re} \\ \Delta L p(i_\beta) + 2\omega_{re}\Delta L i_q \sin\theta_{re} + \left(\omega_{re}\lambda_m - 2\Delta L p(i_q)\right)\cos\theta_{re} \end{bmatrix} \\ &= \begin{bmatrix} \Delta L p(i_\alpha) + 2\omega_{re}\Delta L i_\beta - \left[\omega_{re}\left(\lambda_m + 2\Delta L i_d\right) - 2\Delta L p(i_q)\right]\sin\theta_{re} \\ \Delta L p(i_\beta) - 2\omega_{re}\Delta L i_\alpha + \left[\omega_{re}\left(\lambda_m + 2\Delta L i_d\right) - 2\Delta L p(i_q)\right]\cos\theta_{re} \end{bmatrix} \end{aligned} \tag{3.4-4}$$

Equation (3.4-4) is a part of the EEMF model proposed in [45].

3.1.4 Model Reconstruction Based on Flux Concept

Consider again the last two terms of Equation (3.2), which can be reconstructed as follows:

$$\begin{aligned} V(\theta_{re}) &= \Delta L p\left(\begin{bmatrix} \cos\theta_{re} & \sin\theta_{re} \\ \sin\theta_{re} & -\cos\theta_{re} \end{bmatrix}\begin{bmatrix} i_d \\ i_q \end{bmatrix}\right) + p\begin{bmatrix} \lambda_m \cos\theta_{re} \\ \lambda_m \sin\theta_{re} \end{bmatrix} \\ &= \begin{bmatrix} \Delta L p\left(i_d \cos\theta_{re} + i_q \sin\theta_{re}\right) + p\left(\lambda_m \cos\theta_{re}\right) \\ \Delta L p\left(i_d \sin\theta_{re} - i_q \cos\theta_{re}\right) + p\left(\lambda_m \sin\theta_{re}\right) \end{bmatrix} \end{aligned} \tag{3.5-1}$$

By using Equation (3.4-2), Equation (3.5-1) can be reconstructed into the following form:

$$V(\theta_{re}) = \begin{bmatrix} \Delta L p\left(2 i_d \cos\theta_{re} - i_\alpha\right) + p\left(\lambda_m \cos\theta_{re}\right) \\ \Delta L p\left(2 i_d \sin\theta_{re} - i_\beta\right) + p\left(\lambda_m \sin\theta_{re}\right) \end{bmatrix} \tag{3.5-2}$$

Different from Equation (3.4-3), only the derivative of flux terms, e.g., $p(\lambda_m \cos(\theta_{re}))$, are presented in Equation (3.5-2). Rearranging Equation (3.5-2) yields

$$V(\theta_{re}) = \begin{bmatrix} -\Delta L p(i_\alpha) + p\left[(\lambda_m + 2\Delta L i_d)\cos\theta_{re}\right] \\ -\Delta L p(i_\beta) + p\left[(\lambda_m + 2\Delta L i_d)\sin\theta_{re}\right] \end{bmatrix} = \begin{bmatrix} -\Delta L p(i_\alpha) + p\left[\lambda_{ext}\cos\theta_{re}\right] \\ -\Delta L p(i_\beta) + p\left[\lambda_{ext}\sin\theta_{re}\right] \end{bmatrix} \quad (3.5\text{-}3)$$

where λ_{ext} is the magnitude of the position-related flux term, which is defined as the extended flux, and $\lambda_{ext} = \lambda_m + 2\Delta L i_d = \lambda_m + (L_d - L_q) i_d$. The vector of the extended flux is defined as $\lambda_{ext,\alpha\beta} = \lambda_{ext} \cdot [\cos\theta_{re}, \sin\theta_{re}]^T$.

3.1.5 Reconstructed Salient-Pole PMSM Models

Substituting Equations (3.4-4) and (3.5-3) into Equation (3.2) yields the EEMF model, i.e., Equation (2.5), proposed in [45] and the extended flux model (Equation (3.6)), respectively.

$$\begin{bmatrix} v_\alpha \\ v_\beta \end{bmatrix} = \begin{bmatrix} R_s & 0 \\ 0 & R_s \end{bmatrix} \cdot \begin{bmatrix} i_\alpha \\ i_\beta \end{bmatrix} + p \begin{bmatrix} L_q & 0 \\ 0 & L_q \end{bmatrix} \begin{bmatrix} i_\alpha \\ i_\beta \end{bmatrix} + p \begin{bmatrix} \lambda_{ext}\cos\theta_{re} \\ \lambda_{ext}\sin\theta_{re} \end{bmatrix} \quad (3.6)$$

A comparison among the nonsalient-pole PMSM model (Equation (3.3)) and the two salient-pole PMSM models, i.e., the EEMF model (Equation (2.5)) and extended flux model (Equation (3.6)), is provided in Table 3.1.

Table 3.1. A comparison of Equations (3.3), (2.5), and (3.6).

Machine Type	Machine Model based on Voltage Concept			Machine Model based on Flux Concept		
	Impedance Matrix	Inductance Matrix	Position-Related Terms	Impedance Matrix	Inductance Matrix	Position-Related Terms
Nonsalient-pole PMSM	$\begin{bmatrix} R_s & 0 \\ 0 & R_s \end{bmatrix}$	$\begin{bmatrix} L_s & 0 \\ 0 & L_s \end{bmatrix}$	$\omega_{re}\lambda_m \begin{bmatrix} -\sin\theta_{re} \\ \cos\theta_{re} \end{bmatrix}$	$\begin{bmatrix} R_s & 0 \\ 0 & R_s \end{bmatrix}$	$\begin{bmatrix} L_s & 0 \\ 0 & L_s \end{bmatrix}$	$p\begin{bmatrix} \lambda_m\cos\theta_{re} \\ \lambda_m\sin\theta_{re} \end{bmatrix}$
Salient-pole PMSM	$\begin{bmatrix} R_s & 2\Delta L\omega_{re} \\ -2\Delta L\omega_{re} & R_s \end{bmatrix}$	$\begin{bmatrix} L_d & 0 \\ 0 & L_d \end{bmatrix}$	$E_{ext} \begin{bmatrix} -\sin\theta_{re} \\ \cos\theta_{re} \end{bmatrix}$	$\begin{bmatrix} R_s & 0 \\ 0 & R_s \end{bmatrix}$	$\begin{bmatrix} L_q & 0 \\ 0 & L_q \end{bmatrix}$	$p\begin{bmatrix} \lambda_{ext}\cos\theta_{re} \\ \lambda_{ext}\sin\theta_{re} \end{bmatrix}$

In addition, a comparison between Equations (2.5) and (3.6) from an observer design aspect is provided as follows:

1. A rotor position observer based on Equation (2.5) needs the values of all machine parameters, including R, L_d, and L_q. However, a rotor position observer based on Equation (3.6) does not need L_d information.
2. In Equation (2.5), both v_α and v_β are functions of i_α and i_β. Therefore, the α- and β-loops are not completely decoupled. However, in Equation (3.6), v_α is a function of i_α only; and v_β is a function of i_β only. Therefore, the α- and β-loops are decoupled.
3. In Equation (2.5), the speed information ω_{re} is needed; while Equation (3.6) does not need ω_{re}.
4. E_{ext} in Equation (2.5) depends on both ω_{re} and $p(i_q)$. Therefore, E_{ext} is sensitive to load variations, which may degrade the dynamic performance of the observer. On the contrary, λ_{ext} in Equation (3.6) depends on neither ω_{re} nor $p(i_q)$. Therefore, an observer designed based on Equation (3.6) should have better dynamic performance.
5. An observer can be designed based on Equation (2.5) to obtain the EEMF components directly, from which the rotor position can be easily estimated. However, an observer based on Equation (3.6) can only be used to obtain the derivatives of the extended flux; and integration is needed to calculate the extended flux components, from which the rotor position can be estimated.

In summary, an observer based on Equation (3.6) is less sensitive to machine parameters, speed, and load variations than one based on Equation (2.5). However, an integrator is required to work with the observer to calculate the extended flux components, from which the rotor position information can be extracted directly.

3.2 Discrete-Time SMO and QSMO

According to the literature of different types of model-based rotor position estimators provided in Chapter 2, the SMO is a promising candidate. If the sliding mode is enforced, the dynamics of the states of interest under the sliding mode depend only on the surfaces chosen in the state space and are not affected by system structure or parameter uncertainties. These features are especially attractive for salient-pole PMSM applications since the machine parameters often vary with operating conditions.

The use of sliding-mode principles for digital control systems has become more and more popular over the last few years due to the widespread use of digital controllers [85]. Fast control-loop frequencies that typically occur in a continuous-time SMO (CSMO) require a very small sampling period to make the controller work properly. Recently, discrete-time SMOs (DSMO) have received more and more attention since discretized reaching laws were proposed [86]-[91], which can be used for nonlinear dynamic models with various model/parameter uncertainties or disturbances. To facilitate DSP or microchip-based applications of a DSMO, a finite sampling period is used; and the DSMO's inputs are calculated once per sampling period and held constant during that interval. For instance, in the DSMO for sensorless control of an IPMSM, the controller will read stator currents from current transducers once per PWM cycle; and the current

values will remain constant within this sampling interval. Then the DSMO will estimate the rotor position for the next step during this time interval. It is obvious that the major difference between a CSMO and a DSMO is the sampling frequency and execution rate. In many practical applications, the sampling ratio is limited by the physical condition, environment, and CPU loading. Under such circumstance, the trajectories of the system states of interest are unable to precisely move along the sliding surface, which will lead to a quasi-sliding-mode motion only [86], [87].

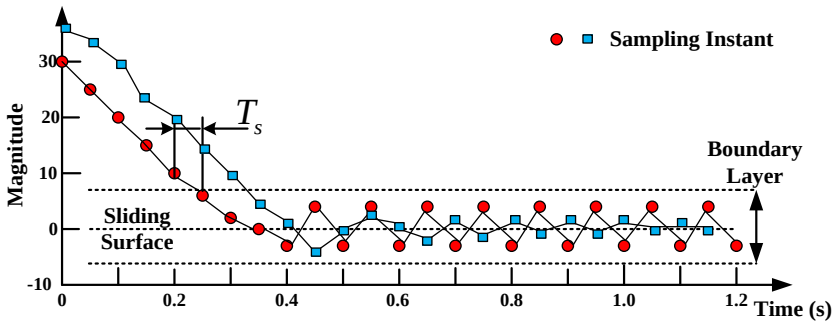

Figure 3.2: State trajectory of a DSMO.

In this dissertation, the definitions of DSMO and QSMO are different. The QSMO is one type of DSMO. In a DSMO, the state trajectory can approach the sliding surface s[k] = 0 asymptotically within finite time steps and continuously stay around the sliding surface by the reaching law. However, because of the limitation of the sampling frequency, the state trajectory cannot exactly move along the sliding surface; and sometimes there will be a chattering problem at steady state. As shown in Figure 3.2, the state trajectory (blue square markers) converges to the sliding surface; however, the other trajectory (red circle markers) has a chattering problem at steady state. In a QSMO, the state trajectory will move from the initial state into a designed boundary layer around the

sliding surface within a finite time. For the QSMO, the reaching law is often different when the magnitude of state is smaller or larger than the width of the boundary layer.

Consider the model of a general nonlinear system:

$$\dot{x} = Ax + Bu + f\left(x\right) \tag{3.7}$$

where x is the state vector of interest; u is the system control input vector; A and B are parameter matrices; and $f(x)$ represents disturbances, parameter uncertainty, or system states to be observed. In order to transform the continuous system model (3.7) into a discrete-time model, the first order Euler approximation is used, which can be expressed as:

$$\dot{x}\left(t\right) \approx \frac{x\left[k+1\right] - x\left[k\right]}{T_s} \tag{3.8}$$

where T_s is the sampling time. Then the discretized version of Equation (3.7) at the $(k+1)^{th}$ step can be expressed as:

$$x\left[k+1\right] = A_d x\left[k\right] + B_d u\left[k\right] + f_d\left[x,k\right] \tag{3.9}$$

where A_d and B_d are parameter matrices, which are calculated from matrices A and B, and depend on T_s; $f_d[x, k]$ is transferred from $f(x)$, which depends on both $x[k]$ and T_s. If $f_d[x, k]$ is bounded and cannot be measured directly, a DSMO can be designed as follows to estimate $f_d[x, k]$.

$$\hat{x}\left[k+1\right] = A_d \hat{x}\left[k\right] + B_d u\left[k\right] + l \cdot Z \tag{3.10}$$

where $\hat{x}\left[k\right]$ is the estimated value of the vector $x[k]$; Z is the output vector of a switching function, e.g., sign function, saturation function, or sigmoid function; and l is the observer gain. It should be pointed out that, for some applications, the parameter matrices

A_d and B_d are not exactly known. Therefore, adaptive or estimation schemes are needed to determine A_d and B_d. In this section, in order to discuss the general design method for DSMO, A_d and B_d are assumed to be known. Let $\varepsilon[k] = x[k] - \hat{x}[k]$, Equation (3.11) can be obtained by subtracting Equation (3.10) from Equation (3.9).

$$\varepsilon[k+1] = A_d \varepsilon[k] + f_d[x,k] - l \cdot Z \tag{3.11}$$

The sliding surface can be simply designed as $\mathbf{s}[k] = \boldsymbol{\varepsilon}[k] = 0$. If the sliding mode is enforced in a CSMO, which means the state trajectory reaches the sliding surface $\mathbf{s}(t) = 0$, the output of the switching function is equal to the state to be observed. However, for a DSMO, $\mathbf{s}[k] = 0$ cannot always be achieved for $k > k^*$, where k^* is a positive finite integer. Since the SMO gain l affects the reaching time and the state behavior around the sliding surface, the following reaching conditions can be achieved [89], [91] if it is well selected.

$$\left|\boldsymbol{\varepsilon}[k+1]\right| < \left|\boldsymbol{\varepsilon}[k]\right| \qquad \text{or} \qquad \left|\boldsymbol{\varepsilon}[k+1]\right| = \Phi \cdot \left|\boldsymbol{\varepsilon}[k]\right| \tag{3.12}$$

where Φ is a diagonal matrix with all entries limited to $[0,1)$. If the motion of the state trajectory obeys Equation (3.12), the tracking error will approach $s[k] = 0$ or reach the designed boundary layer after finite time steps.

3.3 EEMF Model-Based QSMO Design

In this section, a QSMO is designed based on Equation (2.5). Let η denote the $(L_d - L_q)(\omega_{re} i_d - p i_q) + \omega_{re}\lambda_m$ term, which is the amplitude of the EEMF components, the dynamic current equations of a salient-pole PMSM can be expressed as:

$$\begin{cases} \dfrac{di_\alpha}{dt} = \dfrac{v_\alpha}{L_d} - \dfrac{R_s}{L_d} i_\alpha + \omega_{re} \dfrac{L_q - L_d}{L_d} i_\beta + \dfrac{\eta}{L_d} \sin\theta_{re} \\ \dfrac{di_\beta}{dt} = \dfrac{v_\beta}{L_d} - \dfrac{R_s}{L_d} i_\beta - \omega_{re} \dfrac{L_q - L_d}{L_d} i_\alpha - \dfrac{\eta}{L_d} \cos\theta_{re} \end{cases} \tag{3.13}$$

In order to transform the continuous-system model (Equation 3.13) into a discrete-time model, Equation (3.8) is used to represent the derivative terms. Then the discrete-time version of Equation (3.13) at the $(k+1)^{th}$ time step can be expressed as:

$$\begin{cases} \dfrac{i_\alpha[k+1]}{T_s} = \dfrac{v_\alpha[k]}{L_d} - \omega_{re}[k] \dfrac{2\Delta L}{L_d} i_\beta[k] + E_\alpha[k] + \left(\dfrac{L_d - T_s R_s}{T_s L_d} \right) i_\alpha[k] \\ \dfrac{i_\beta[k+1]}{T_s} = \dfrac{v_\beta[k]}{L_d} + \omega_{re}[k] \dfrac{2\Delta L}{L_d} i_\alpha[k] + E_\beta[k] + \left(\dfrac{L_d - T_s R_s}{T_s L_d} \right) i_\beta[k] \end{cases} \tag{3.14}$$

where $E_\alpha = \eta\sin\theta_{re}/L_d$ and $E_\beta = -\eta\cos\theta_{re}/L_d$. A current estimator which has the same structure as a current model (Equation 3.14) of the salient-pole PMSM can be designed as follows:

$$\begin{cases} \dfrac{\hat{i}_\alpha[k+1]}{T_s} = \dfrac{v^*_\alpha[k]}{L_d} - \omega_{re}[k] \dfrac{2\Delta L}{L_d} i_\beta[k] + lZ_\alpha[k] + \left(\dfrac{L_d - T_s R_s}{T_s L_d} \right) \hat{i}_\alpha[k] \\ \dfrac{\hat{i}_\beta[k+1]}{T_s} = \dfrac{v^*_\beta[k]}{L_d} + \omega_{re}[k] \dfrac{2\Delta L}{L_d} i_\alpha[k] + lZ_\beta[k] + \left(\dfrac{L_d - T_s R_s}{T_s L_d} \right) \hat{i}_\beta[k] \end{cases} \tag{3.15}$$

where Z_α and Z_β are the outputs of a switching function, which is a saturation function in this dissertation; and l is the observer gain. In Equation (3.15), the commanded voltage values v^*_α and v^*_β are used, which are obtained from the current-regulated vector control of the salient-pole PMSM, such that the terminal voltages do not need to be measured.

Let $\boldsymbol{\varepsilon}[k]^T = \left[\varepsilon_\alpha[k] \quad \varepsilon_\beta[k] \right] = \left[i_\alpha[k] - \hat{i}_\alpha[k] \quad i_\beta[k] - \hat{i}_\beta[k] \right]$ be the vector of the current tracking errors, and the equations of the current tracking error dynamics can be obtained by subtracting Equation (3.15) from Equation (3.14):

$$\begin{cases} \varepsilon_\alpha[k+1] = \left(1 - \dfrac{T_s R_s}{L_d}\right)\varepsilon_\alpha[k] + T_s E_\alpha[k] - T_s l Z_\alpha[k] \\ \varepsilon_\beta[k+1] = \left(1 - \dfrac{T_s R_s}{L_d}\right)\varepsilon_\beta[k] + T_s E_\beta[k] - T_s l Z_\beta[k] \end{cases} \tag{3.16}$$

The sliding surface is designed as s[k] = $\boldsymbol{\varepsilon}$[k] = 0. A variable switching function for the QSMO is defined as follows:

$$Z_{\alpha\beta} = \begin{cases} Z_0 & \varepsilon[k] \geq Z_0 \\ \varepsilon[k] & -Z_0 < \varepsilon[k] < Z_0 \\ -Z_0 & \varepsilon[k] \leq -Z_0 \end{cases} \tag{3.17}$$

where Z_0 is the width of the boundary layer, and $Z_0 > 0$. The switching function will change its output according to the movement of the state, i.e., the current tracking error, and force the state trajectory to move toward the sliding surface and remain in a quasi-sliding mode. If the quasi-sliding mode is enforced, the current tracking error will be limited within a certain boundary; the output of the switching function will be equal to the EEMF with harmonics.

3.4 Parameter Adaption Scheme

The two parameters, i.e., the observer gain l and the width Z_0 of the boundary layer of the saturation function, are critical to the performance of a QSMO. In this section, an online parameter adaption methodology is proposed for the QSMO. The proposed method originated from system stability verification.

3.4.1 Stability Analysis

A stability analysis is provided to verify that, if the parameters are selected properly, the QSMO will exhibit a quasi-sliding-mode behavior after a finite time step. In order to force the state trajectory to move from the initial state to the sliding surface, the following two conditions should be satisfied simultaneously, and the corresponding schematic diagrams are shown in Figures 3.3 and 3.4, respectively.

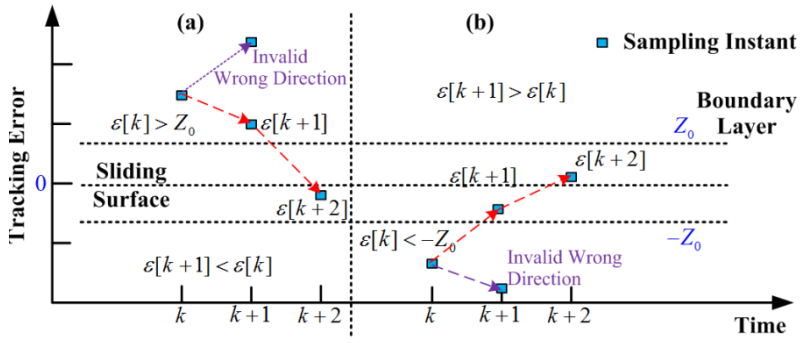

Figure 3.3: Illustration of the state trajectory for Condition 1.

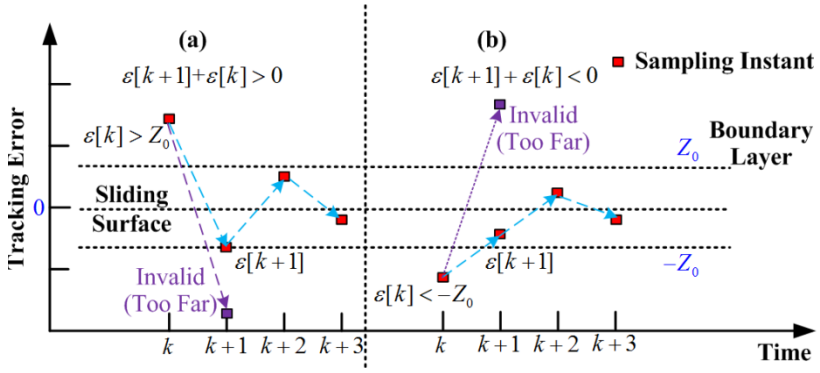

Figure 3.4: Illustration of the state trajectory for Condition 2.

1. The state trajectory should move towards the sliding surface when the state magnitude is larger than the width of the boundary layer, i.e.,

$|\boldsymbol{\varepsilon}[k]| > Z_0$), which means (a) when $\boldsymbol{\varepsilon}[k] > Z_0$, $\boldsymbol{\varepsilon}[k+1] < \boldsymbol{\varepsilon}[k]$; (b) while when $\boldsymbol{\varepsilon}[k] < -Z_0$, $\boldsymbol{\varepsilon}[k+1] > \boldsymbol{\varepsilon}[k]$.

2. The state trajectory should not move too far in the approaching direction in each step. In order to limit the change of the state trajectory between the k^{th} and $(k+1)^{\text{th}}$ steps, the following condition should be satisfied: (a) when $\boldsymbol{\varepsilon}[k] > Z_0$, $\boldsymbol{\varepsilon}[k+1] + \boldsymbol{\varepsilon}[k] > 0$; (b) while when $\boldsymbol{\varepsilon}[k] < -Z_0$, $\boldsymbol{\varepsilon}[k+1] + \boldsymbol{\varepsilon}[k] < 0$.

If both conditions are satisfied, not only the discretized convergence but also the stability of the observer can be guaranteed, where the discretized stability criterion can be expressed as $1/2\cdot(\boldsymbol{\varepsilon}[k+1]-\boldsymbol{\varepsilon}[k])\cdot\boldsymbol{\varepsilon}[k] < 0$. In order to satisfy these two conditions, the following constraints for the parameters of the QSMO can be obtained:

$$\left|E_\alpha[k]\right| < lZ_0 < \left(\frac{2}{T_s} - \frac{R}{L_d}\right)Z_0 - \left|E_\alpha[k]\right| \tag{3.18-I}$$

$$Z_0 > \frac{2|\eta|}{2L_d f_s - R} \tag{3.18-II}$$

The derivation of Equation (3.18-I) and Equation (3.18-II) is provided in Appendices A and B. Since the amplitudes and frequencies of E_α and E_β are identical, except that they have a 90° phase shift, Equation (3.18-I) is also applicable to E_β. In Equation (3.18-I), the inequality on the left-hand side indicates that lZ_0 should be larger than the amplitude of the EEMF. If this inequality is satisfied, Condition 1 can be guaranteed. This requirement has been mentioned in the previous work [49], [63]. However, the inequality on the right-hand side of Equation (3.18-I) should be satisfied simultaneously, which is derived from Condition 2 and indicates that lZ_0 should also have

an upper boundary. Otherwise, a phase shift will present in the rotor position estimated from the QSMO when the load changes. Furthermore, without proper parameters, a discretized chattering problem or even system instability will occur.

In order to guarantee the existence of l and Z_0, the upper boundary in Equation (3.18-I) should always be greater than the lower boundary, which is used to derive Equation (3.18-II). It is known that the SMO has a high gain effect, i.e., a large observer gain can help suppress the tracking error caused by disturbances. Therefore, in this dissertation, the tracking error, ε, can theoretically be reduced by increasing the observer gain l. However, as shown in Equation (3.18-II), for a discrete-time system, the tracking error cannot be reduced by arbitrarily increasing the observer gain l; because the minimum tracking error depends on the sampling frequency f_s.

3.4.2 Parameter Adaption Scheme

Let $Z_{\min}$ denote the minimum value of Z_0. According to Equation (3.18-II), $Z_{\min}$ is defined as:

$$Z_{\min} = \frac{2|\eta|}{2L_d f_s - R} \tag{3.19}$$

If a constant PWM frequency is adopted and currents are sampled once per PWM cycle, the sampling frequency f_s can be viewed as a constant. Assume that the machine parameters have no large variations. Therefore, $Z_{\min}$ is a function of η. At low-speed or light-load operating conditions, η will be small and, therefore, $Z_{\min}$ will be relatively small. On the other hand, at high-speed or heavy-load conditions, η will be large and $Z_{\min}$ will also be relatively large. In order to satisfy both Equation (3.18-I) and Equation (3.18-II),

Z_0 should be larger than the maximum value of $Z_{\min}$ corresponding to the highest speed and maximum torque condition. However, for low-speed and light-load conditions, a small Z_0 is desired to ensure good current tracking performance. The best method for solving this dilemma is using an adaptive Z_0 not only to satisfy Equation (3.18) but also to guarantee the best current tracking performance for each load condition.

Consider again the magnitude of the EEMF η, in steady state di_q/dt can be assumed to be 0. Thus, if the values of i_d and ω_{re} are known, the value of η can be determined. In practice, the value of i_d can be obtained from the electromagnetic torque command. For a salient-pole PMSM, the electromagnetic torque T_e can be expressed as:

$$T_e = \frac{3}{2} p_o i_q \left[\left(L_d - L_q \right) i_d + \lambda_m \right] \tag{3.20}$$

where p_o is the number of magnetic pole pairs of the salient-pole PMSM. The relationship between i_d and i_q depends on the control algorithm used for the IPMSM. For example, if the maximum torque per ampere (MTPA) control is used, a simplified relationship between i_d and i_q can be obtained by taking advantage of Taylor's series expansion [92] as follows:

$$i_d^* = \frac{(L_d - L_q)}{\lambda_m} i_q^2 \tag{3.21}$$

According to Equations (3.20) and (3.21), once the torque command is given, the values of i_d and i_q can be uniquely determined. In practice, the relationship between the commanded torque T_e^* and currents i_d and i_q can be implemented by using look-up tables or high-order polynomials.

According to the above analysis, η can be expressed as a function of the electromagnetic torque T_e and speed ω_{re} of the IPMSM, i.e., $\eta = \eta(T_e, \omega_{re})$. If both the

speed and torque commands are given, i.e., ω^*_{re} and T_e^*, the value of η can be uniquely determined. Then $Z_{\min}$ can be calculated by using Equation (3.19), and Z_0 can be simply set to be equal to $Z_{\min}$. However, the method of directly setting $Z_0 = Z_{\min}$ has some limitations. First, since the machine parameters L_d and R_s may change significantly with operating conditions, it will require extra effort to obtain the accurate information of these parameters for determining Z_{min} using Equation (3.19). Second, Equations (3.18-I), (3.18-II), and (3.19) are derived for steady-state operating conditions. During transient conditions, the exact value of the current derivative term, di_q/dt, is difficult to obtain. Considering these two uncertainties, this work proposes the following methods to ensure that the QSMO is robust to both load transients and machine parameter variations.

First, in industrial drives, the maximum slew rate limit of the current change is usually set in the controller. Thus, the current derivative is a bounded value. To handle current transients during load variations, the values of l and Z_0 are adaptively determined from $Z_{\min}$ online as follows.

$$Z_0 = \alpha Z_{\min} \tag{3.22}$$

where α is a new coefficient, which is always greater than 1. The method to determine α based on the slew rate limit of the current change will be discussed later. Furthermore, according to (3.18-I), lZ_0 should be greater than the magnitude of the EEMF, which can be guaranteed if $l \cdot Z_{\min}$ is set to be equal to the amplitude of the estimated EEMF $\hat{\eta}$. Therefore,

$$l = \hat{\eta} / Z_{\min} \tag{3.23}$$

To guarantee Z_0, determined by Equation (3.22), will always satisfy Equation (3.18-I) and (3.18-II) in the transient, a sufficiently large α should be selected, i.e.,

$\alpha - 1 \geq \left| \dfrac{(L_d - L_q) p i_q}{(L_d - L_q)(\omega_{re} i_d) + \omega_{re} \lambda_m} \right|$, where the sum of the numerator and denominator is the magnitude of the EEMF η, and the denominator is the value of η at steady state. Therefore, during a large load transition, the value of (α−1) indicates the maximum percentage of the uncertainty in η with respect to its steady-state value caused by the current transient term pi_q, which can be further written as follows:

$$\left| p i_q \right| \leq (\alpha - 1) \underbrace{\left| \omega_{re} \left(i_d + \frac{\lambda_m}{L_d - L_q} \right) \right|}_{\beta} \tag{3.24}$$

In Equation (3.24), the maximum value of the current derivative can be determined from the slew rate limit of the current. Then the relationship between the magnitudes of the actual and estimated EEMF will be:

$$\begin{aligned} |\eta| &= \left| (L_d - L_q)(\omega_{re} i_d) + \omega_{re} \psi_m - (L_d - L_q) p i_q \right| \\ &\leq \left| (L_d - L_q)(\omega_{re} i_d) + \omega_{re} \psi_m \right| + \left| (L_d - L_q) p i_q \right| \\ &\leq \alpha \left| (L_d - L_q)(\omega_{re} i_d) + \omega_{re} \psi_m \right| \\ &= \alpha \left| \hat{\eta} \right| \end{aligned} \tag{3.25}$$

Therefore, with a sufficiently large α, the observer parameters calculated by Equations (3.22) and (3.23) will always satisfy Equations (3.18-I) and (3.18-II). In Equation (3.24), the value of β can be calculated by using the steady-state values of i_d and ω_{re}. In normal cases, there is $L_d < L_q$, and i_d is always negative for flux weakening; otherwise, it is equal to zero. Thus, i_d and $\lambda_m/(L_d - L_q)$ have the same sign. To ensure that Equation (3.24) is always valid for all of the current conditions, a large value is obtained

for α by using the minimum value of β when $i_d = 0$. Therefore, α can be determined as follows.

$$\alpha = 1 + \frac{(L_d - L_q)|pi_q|_{\max}}{\omega_{re}\lambda_m} \tag{3.26}$$

where $|pi_q|_{\max}$ is the maximum slew rate limit of the current derivative, and $(\alpha - 1)$ is inversely proportional to the rotor electrical speed. The block diagram of the proposed parameter adaption scheme and the resulting adaptive QSMO are shown in Figure 3.5.

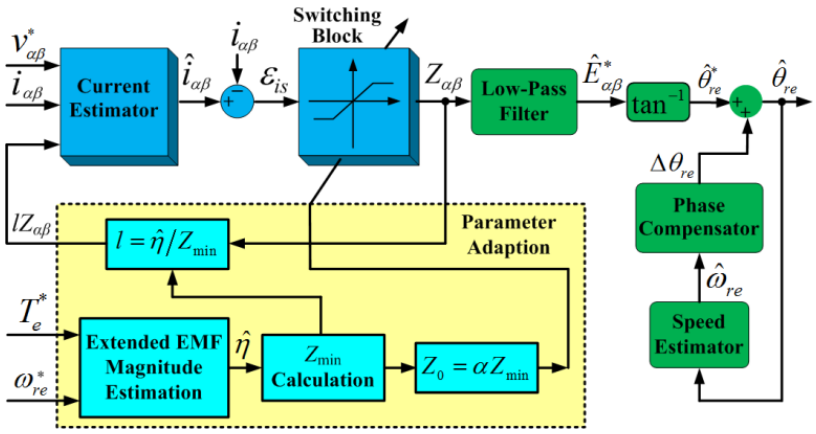

Figure 3.5: Block diagram of the adaptive QSMO.

Second, machine parameter variations are always one of the most critical issues in the salient-pole PMSM position estimation. In high power applications, the machine parameters, e.g., stator resistance R_s and inductances L_d and L_q, have large variations when the operating point changes. In the denominator of Equation (3.19), R_s is much smaller than the term $2L_df_s$. Therefore, the variation of R_s has little influence on the observer's performance, especially in medium- and high-speed conditions. To consider the effect of L_d and L_q variations on the QSMO performance, lookup tables are utilized to obtain their values in real time according to the load conditions. For example, a finite

element analysis (FEA)-based method can be used to find the relationships between the inductances and the stator currents and gamma angle, which is defined as the angle between the phase current vector and negative *d*-axis. Such relationships can be expressed by lookup tables, as shown in Figure 3.6 for L_q of the salient-pole PMSM used in this work. The lookup tables can then be used to calculate the QSMO parameters based on Equation (3.19). By using the coefficient α and the inductance lookup tables, the proposed adaptive QSMO is robust to both machine parameter variations and load transients.

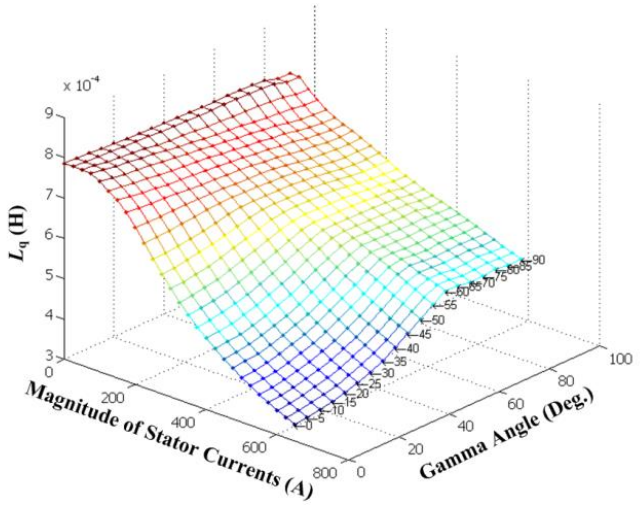

Figure 3.6: L_q lookup table generated by a FEA method.

3.5 Extended Flux Model-Based QSMO Design

To design an observer based on Equation (3.6) without using an integrator, the most straightforward approach is to further process the derivative of the extended flux to obtain a voltage term that contains the rotor position explicitly. The derivative of the

extended flux can be viewed as a voltage term or EMF term, which is denoted as $e'_{\alpha\beta}$ and can be calculated as:

$$\begin{aligned} e'_{\alpha\beta} &= \begin{bmatrix} e'_\alpha \\ e'_\beta \end{bmatrix} = p\begin{bmatrix} \lambda_{ext}\cos\theta_{re} \\ \lambda_{ext}\sin\theta_{re} \end{bmatrix} = \begin{bmatrix} \cos\theta_{re}\,p(\lambda_{ext}) + \lambda_{ext}\,p(\cos\theta_{re}) \\ \sin\theta_{re}\,p(\lambda_{ext}) + \lambda_{ext}\,p(\sin\theta_{re}) \end{bmatrix} \\ &= \omega_{re}\lambda_{ext}\begin{bmatrix} -\sin\theta_{re} \\ \cos\theta_{re} \end{bmatrix} + (L_d - L_q)\,p(i_d)\begin{bmatrix} \cos\theta_{re} \\ \sin\theta_{re} \end{bmatrix} \end{aligned} \tag{3.27}$$

As shown in Equation (3.27), both $\cos\theta_{re}$ and $\sin\theta_{re}$ related terms are present simultaneously in the expressions of e'_α and e'_β. Therefore, it is still complex to estimate the rotor position using Equation (3.27) directly. However, in some applications if $(L_d - L_q)\,p(i_d) \ll \omega_{re}\lambda_{ext}$ is satisfied, the last term in Equation (3.27) can be ignored and the position estimation will be notably simplified [93]. However, this method has obvious limitations due to the assumption $(L_d - L_q)\,p(i_d) \ll \omega_{re}\lambda_{ext}$. To eliminate the limitation, $e'_{\alpha\beta}$ is processed in the phasor form as follows:

$$\begin{aligned} & e'_\beta - je'_\alpha = \omega_{re}\lambda_{ext}(\cos\theta_{re} + j\sin\theta_{re}) + p(\lambda_{ext})(-j\cos\theta_{re} + \sin\theta_{re}) \\ & = \omega_{re}\lambda_{ext}e^{j\theta_{re}} - jp(\lambda_{ext})e^{j\theta_{re}} = Ae^{j(\theta_{re}+\varphi)} \end{aligned} \tag{3.28}$$

where: $A = \sqrt{(p(\lambda_{ext}))^2 + (\omega_{re}\lambda_{ext})^2}$ and $\varphi = \tan^{-1}\left[\dfrac{-p(\lambda_{ext})}{\omega_{re}\lambda_{ext}}\right]$. If $p(\lambda_{ext}) = 0$, $|\varphi|$ will be equal to zero, which means that the position calculated from $e'_{\alpha\beta}$, $\tilde{\theta} = \tan^{-1}\left[-\dfrac{p(\lambda_{ext}\cos\theta_{re})}{p(\lambda_{ext}\sin\theta_{re})}\right]$ is equal to the actual rotor position. However, in practical applications when the salient-pole PMSM operates in the low-speed region or has a large variation in the extended flux, e.g., caused by an abrupt i_d change, φ will not be exactly equal to zero, and a phase error will exist.

In this section, a QSMO based on the extended flux model (Equation 3.6) is proposed to estimate the derivatives of extended flux components, from which $\tilde{\theta}$ can be obtained. Since $\tilde{\theta}$ is not an accurate estimation of the actual rotor position, a dynamic position compensator is further proposed to eliminate the error between $\tilde{\theta}$ and the actual rotor position to improve the rotor position estimation performance during low-speed operations and large load transients. The overall block diagram of the proposed rotor position estimator is shown in Figure 3.7, which contains three major parts: a QSMO, an envelope detector, and a dynamic position compensator. The QSMO is designed as follows:

$$\begin{cases} \hat{i}_\alpha[k+1] = T_s\left(\dfrac{v^*_\alpha}{L_q} + lZ_\alpha[k]\right) + \left(1 - \dfrac{T_s R_s}{L_q}\right)\hat{i}_\alpha[k] \\ \hat{i}_\beta[k+1] = T_s\left(\dfrac{v^*_\beta}{L_q} + lZ_\beta[k]\right) + \left(1 - \dfrac{T_s R_s}{L_q}\right)\hat{i}_\beta[k] \end{cases} \tag{3.29}$$

where T_s is the sampling period of the QSMO; v^*_α and v^*_β are the voltage commands generated by the current controllers; and $Z_\alpha[k]$ and $Z_\beta[k]$ are the outputs of the switching function at the k^{th} time step, which contain $e'_{\alpha\beta}$ components, if the sliding mode is enforced. The angle between the vector $e'_\beta - je'_\alpha$ and the α-axis can be estimated as:

$$\tilde{\theta} = \tan^{-1}\left(-\frac{Z_\alpha}{Z_\beta}\right).$$

However, per previous discussion, $\tilde{\theta}$ needs to be compensated for the phase error to handle low-speed and transient conditions; and the phase error φ can be calculated as follows:

$$\varphi[k] = \tan^{-1}\left[\frac{\hat{\lambda}_{ext}[k-1] - \hat{\lambda}_{ext}[k]}{\hat{\omega}_{re}[k]\hat{\lambda}_{ext}[k]T_s}\right] \tag{3.30}$$

where $\hat{\omega}_{re}$ and $\hat{\lambda}_{ext}$ are the estimated rotor speed and magnitude of the estimated extended flux, respectively. A dynamic position compensator, as shown in Figure 3.7, is designed to obtain φ based on Equation (3.30). The estimated rotor position $\hat{\theta}_{re}$ is obtained by adding φ to $\tilde{\theta}$. The estimated rotor speed $\hat{\omega}_{re}$ can then be obtained from $\hat{\theta}_{re}$ by using a moving average (MA) or PLL.

An envelope detector is designed to extract the product of $\hat{\omega}_{re}$ and $\hat{\lambda}_{ext}$ in Equation (3.30), which can be expressed as:

$$Z_\beta \cos\hat{\theta}_{re} - Z_\alpha \sin\hat{\theta}_{re} \approx \hat{\omega}_{re}\hat{\lambda}_{ext} + p\left(\lambda_{ext}\right)\sin\left(\theta_{re} - \hat{\theta}_{re}\right) \xrightarrow{\theta_{re} \approx \hat{\theta}_{re}} \approx \hat{\omega}_{re}\hat{\lambda}_{ext} \tag{3.31}$$

According to Equation (3.31), if the error between the estimated and actual rotor positions is small enough, the $\sin\left(\theta_{re} - \hat{\theta}_{re}\right)$ term can be ignored, such that $\hat{\omega}_{re}\hat{\lambda}_{ext}$ is obtained. Once the rotor speed is estimated, $\hat{\lambda}_{ext}$ can then be calculated.

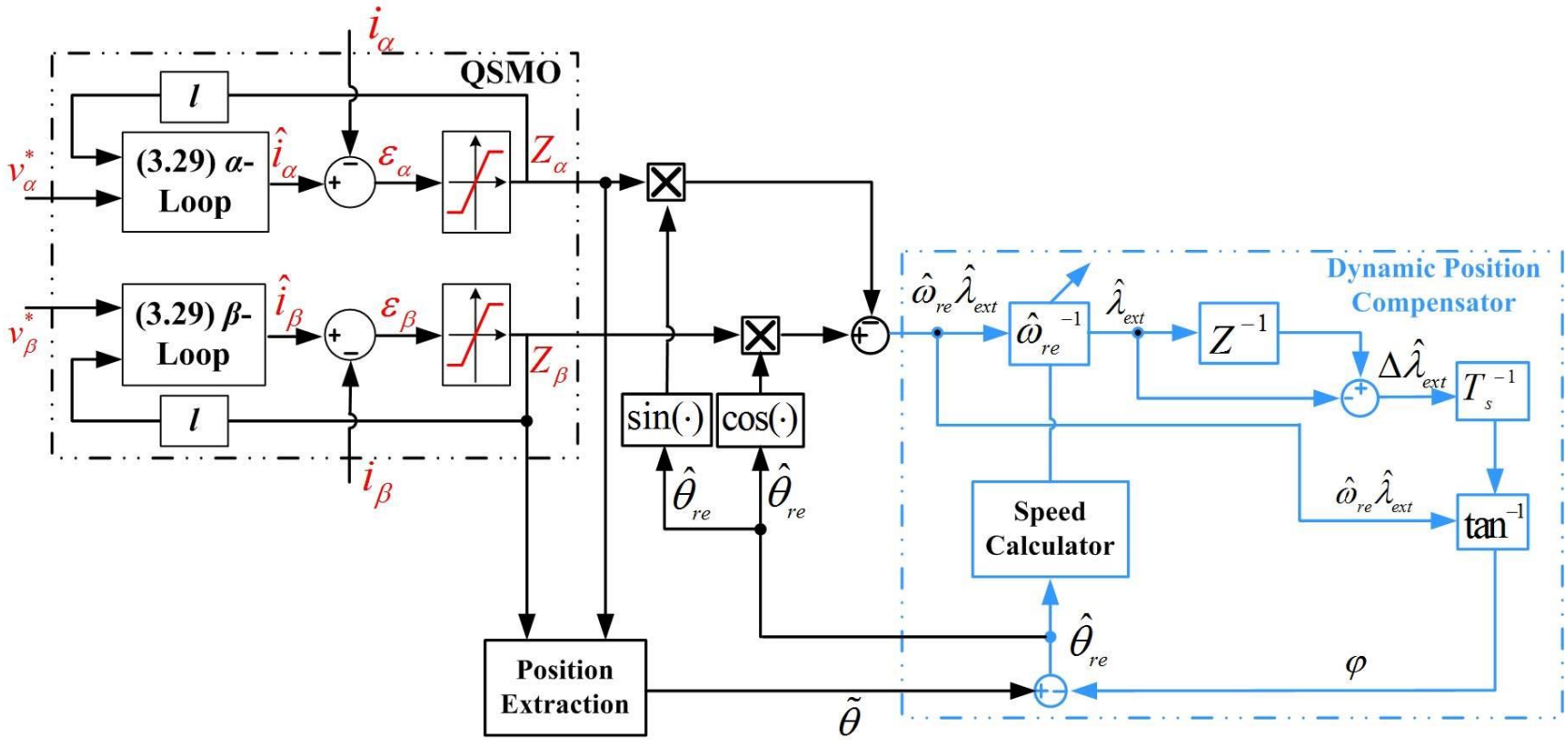

Figure 3.7: Schematic diagram of the proposed rotor position estimator.

3.6 Summary

In this chapter, multiple adaptive QSMOs have been proposed for sensorless control of salient-pole PMSMs operating in medium and high-speed conditions. The first QSMO was designed based on the EEMF model of the salient-pole PMSMs. The rotor position was then extracted from the output of the QSMO, which contains the EEMF components. Using the proposed observer parameter adaption scheme, the QSMO is robust to load variations and allows the state trajectory to quickly converge into the designed boundary layer around the sliding surface. The global stability and quasi-sliding-mode motion are guaranteed using the proposed adaptive switching function. The performance of the adaptive QSMO has no degradation even using a low sampling ratio in high-speed and heavy-load conditions. These capabilities, however, could not be achieved by using the conventional DSMO without the parameter adaption scheme.

The second QSMO is based on the extended flux model of the salient-pole PMSMs. The novel extended flux model was derived by using a mathematical model reconstruction process, which was proposed for dynamic modeling of a generic salient-pole PMSM. The extended flux model has notable advantages including a simpler structure and improved robustness to the variations in machine parameters and operating conditions (both speed and torque), when compared to the EEMF-based model. The rotor position extracted from the output quantities of the QSMO was compensated by the output of a dynamic position compensator, which further improved the dynamic performance and low-speed operating capability of the sensorless control system.

CHAPTER 4

IMPROVED ROTOR POSITION/SPEED ESTIMATORS FOR SENSORLESS CONTROL OF SALIENT-POLE PMSMS

A rotor position/speed estimation system usually contains three major parts: a state observer, a position estimator, and a speed estimator. In Chapter 3, QSMOs were proposed to estimate the EEMF components and the derivatives of the extended flux components. Since QSMOs belong to model-based observers, the common problems for this category of observers in regard to practical applications are discussed first. Then, two major schemes were proposed to achieve the improved position and speed estimation. First, the rotor speed is estimated independently using a MRAS-based method, which is decoupled from the position estimation. To reduce the noise content in the estimated speed, an adaptive line enhancer (ALE) was proposed to work with a QSMO, leading to an improved reference model for the speed estimation. The proposed MRAS-based speed estimator has two operating modes, which are suitable for generator and motor applications, respectively. Second, the estimated rotor speed is used as a feedback input signal to mitigate the oscillating error in the estimated rotor position, leading to an integrated position and speed estimation system.

4.1 Problem Description

In the medium- and high-speed regions of sensorless PMSM drive systems, the rotor position and speed are commonly estimated by using model-based methods, which

were reviewed in Chapter 2. Generally speaking, there are three major parts in those model-based position/speed estimators:

1. State observer to estimate the position/speed related system states.
2. Position estimator to extract the rotor position information from the estimated states or rotor speed.
3. Speed estimator to extract the rotor speed from the estimated states or rotor position.

Two major types of state observers were designed based on the reduced-order machine models, as illustrated in Figure 4.1(a) and (b). The method presented in [46] was performed in the rotor reference frame, where the rotor speed was first estimated from the estimated system states; and then the rotor position was obtained by integrating the estimated rotor speed. In contrast, the methods presented in [45], and also the QSMO-based methods presented in Chapter 3, were performed in the stationary reference frame, where the rotor position was extracted directly from the estimated system states using an arctangent, PLL or Luenberger observer. Then, rotor speed was obtained from the estimated rotor position.

In practical applications, due to the cascaded structure, the performance of the position and speed estimators may not be acceptable during large load transient and machine parameter variations. For example, there are several inherent drawbacks in the position/speed estimation method in Figure 4.1(a).

First of all, since the position estimator and the speed estimator are connected sequentially without feedback or other adjustment schemes, any error will propagate in the loop. For instance, if the state observer has improper gains, the performance of the

following position and speed estimators will be affected. Since the speed estimator is the last module in the loop, it will be affected by the performance of all of the subsystems prior to it.

Second, the position estimation is sensitive to load variations. Since the speed is calculated from the estimated position, the speed estimation is also sensitive to load variations. An effective solution to the problems of the estimators shown in Figure 4.1(a) and (b) is to decouple the rotor speed and position estimation, i.e., speed and position are estimated independently.

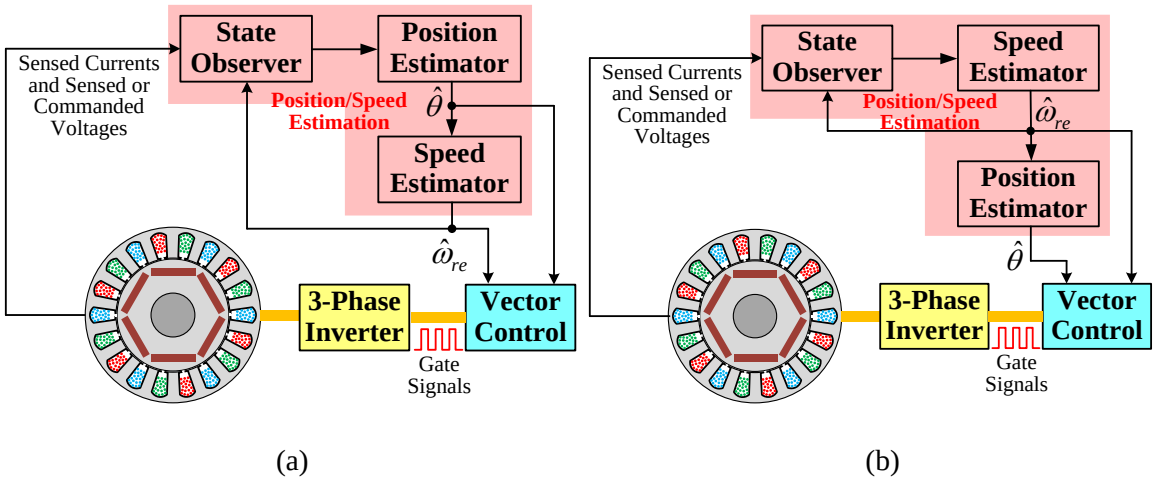

Figure 4.1: Illustrations of different types of rotor position/speed estimation methods.

In industrial applications, such as generators in electric vehicles, considering switching losses as well as thermal and EMI issues, the switching frequency of the rectifiers/inverters is usually selected such that there are 10-20 switching cycles per electric revolution. In vector control, the phase currents are usually sensed once per switching cycle. If the sensed currents are used in position/speed estimation, the low sampling ratio of the phase current poses challenges to the application of a QSMO, where

the sampling ratio is defined as the number of current samples per electric revolution. As a result, the waveforms of the estimated EEMF components have distortions, including both phase shift and magnitude variation. In this case, conventional position estimators, e.g., PLL, suffer an oscillation problem when extracting the rotor position information from the distorted EEMF components. The estimated rotor position has a large amount of noise and errors. To solve this problem and further improve the quality of position estimation, effective schemes are needed to mitigate the position oscillation caused by using a low sampling ratio.

4.2 Proposed MRAS-Based Rotor Speed Estimator

In this section, the QSMO presented in Chapter 3 is utilized to estimate the EEMF of a salient-pole PMSM. Based on the estimated EEMF, rotor position and speed are estimated separately. An MRAS-based speed estimator is proposed to estimate the rotor speed using a heterodyning speed adaption mechanism. An ALE is proposed to filter the estimated EEMF without introducing any phase delay between the original and filtered EEMF components. Compared to the case without ALE, the SMO plus the ALE provides an improved reference model in an MRAS. The proposed MRAS speed estimator has two different operating modes, which can be utilized for different applications in vehicles, such as traction motors and generators.

4.2.1 Conventional MRAS-Based Rotor Speed Estimator

The MRAS [57], [58], [94]-[96] is an effective scheme for speed estimation in drive systems of different motors, e.g., PMSMs [31], [50], IMs [57], [58], [94]-[96], and

BLDC motors [44]. In an MRAS, an adjustable model and a reference model are connected in parallel. The structure of a typical MRAS-based speed estimator is shown in Figure 2.7.

In this section, the EEMF is estimated by using the QSMO, which contains information on the rotor speed and is a good candidate for the reference model. Then, an adjustable model should be designed to output the EEMF as well as use the rotor speed as an internal state whose value is updated (estimated) by an adaptive mechanism. With a proper adaptive mechanism, the output of the adjustable model is expected to converge to the output of the reference model. In this case, the internal states of the two models should be identical. Thus, the rotor speed estimated by the adaptive mechanism converges to the actual rotor speed contained in the reference model. From this point of view, the adjustable model is a kind of adaptive filter/observer.

The design of the adjustable model originated from the EEMF model (Equation 2.5), which can be rewritten as:

$$\begin{bmatrix} v_\alpha \\ v_\beta \end{bmatrix} = \begin{bmatrix} R_s + pL_d & \omega_{re}(L_d - L_q) \\ \omega_{re}(L_q - L_d) & R + pL_d \end{bmatrix} \begin{bmatrix} i_\alpha \\ i_\beta \end{bmatrix} + \begin{bmatrix} E_\alpha \\ E_\beta \end{bmatrix} \tag{4.1}$$

where the EEMF vector $E_{\alpha\beta} = [E_\alpha, E_\beta]^T$ is defined as:

$$\begin{bmatrix} E_\alpha \\ E_\beta \end{bmatrix} = \left[(L_d - L_q)(\omega_{re} i_d - p i_q) + \omega_{re} \lambda_m \right] \begin{bmatrix} -\sin\theta \\ \cos\theta \end{bmatrix} \tag{4.2}$$

By using a properly designed QSMO, the estimated EEMF components, $\hat{E}_{\alpha\beta} = [\hat{E}_\alpha, \hat{E}_\beta]^T$, can be obtained. If the rotor speed changes slowly, i.e., $d\omega_{re}/dt \approx 0$, the derivatives of the estimated EEMF components are calculated as:

$$\begin{cases} \dot{\hat{E}}_\alpha = -\omega_{re}\hat{E}_\beta \\ \dot{\hat{E}}_\beta = \omega_{re}\hat{E}_\alpha \end{cases} \tag{4.3}$$

The adjustable model was designed by following the form of Equation (4.3) as follows:

$$\begin{bmatrix} \dot{\tilde{E}}_\alpha \\ \dot{\tilde{E}}_\beta \end{bmatrix} = \hat{\omega}_{re} \underbrace{\begin{bmatrix} 0 & -1 \\ 1 & 0 \end{bmatrix}}_{J} \cdot \begin{bmatrix} \tilde{E}_\alpha \\ \tilde{E}_\beta \end{bmatrix} + \underbrace{\begin{bmatrix} L_{11} & L_{12} \\ L_{21} & L_{22} \end{bmatrix}}_{\mathbf{L}} \cdot \begin{bmatrix} \hat{E}_\alpha - \tilde{E}_\alpha \\ \hat{E}_\beta - \tilde{E}_\beta \end{bmatrix} \tag{4.4}$$

where $\tilde{E}_{\alpha\beta} = [\tilde{E}_\alpha, \tilde{E}_\beta]^T$ is the output vector of the adjustable model, which is also a vector of estimated EEMF components; $\hat{\omega}_{re}$ is the estimated electrical rotor speed, which is the output of the adaptive mechanism; **L** is the MRAS gain matrix, which can be configured by using a linear observer design technique, e.g., pole assignment [44]. In practical applications, the off-diagonal elements, L_{21} and L_{12}, can be set to be zero [44] to simplify the design procedure. Based on the outputs of the adjustable model and the reference model, the rotor speed can be estimated by using a PI speed regulator as follows:

$$\hat{\omega}_{re} = \left(k_p + \frac{k_i}{s}\right)\left[\left(\hat{E}_{\alpha\beta} - \tilde{E}_{\alpha\beta}\right)^T \cdot J \cdot \tilde{E}_{\alpha\beta}\right] \tag{4.5}$$

4.2.2 Basic Concept for a New MRAS-Based Rotor Speed Estimator

In Section 4.2.1, the conventional MRAS-based rotor speed estimator using a QSMO as the reference model was discussed. However, in a practical drive system, a QSMO may not be an effective reference model for several reasons. First, the inherent nonlinearity of the switching function, e.g., the sign function or saturation function, used in the QSMO brings noisy content into the output of the QSMO. Second, the EEMF

components of a salient-pole PMSM are both torque- and speed-dependent. The expression of the EEMF vector defined in Equation (4.2) can be rewritten in the following form:

$$\begin{bmatrix} E_\alpha(t) \\ E_\beta(t) \end{bmatrix} = \eta(t) \cdot \begin{bmatrix} -\sin\left[\omega_{re}(t) \cdot t + \theta_0\right] \\ \cos\left[\omega_{re}(t) \cdot t + \theta_0\right] \end{bmatrix} \tag{4.6}$$

where θ_0 is the initial rotor position. The amplitude of the EEMF, $\eta(t)$, is time variant and depends on the magnitudes of both currents and rotor speed. Under fast varying load conditions, the current derivative term, pi_q, can be a large and varying component, which results in a larger variation in $\eta(t)$. In addition, when the torque is not constant, the rotor speed, ω_{re}, has an oscillation due to imperfect rotor speed regulation.

Considering these issues, an ALE is designed to effectively filter out the noisy content from the estimated EEMF components. The resulting QSMO with the ALE provides an improved reference model for the MRAS. Moreover, a heterodyning speed adaption mechanism replaces the adaptive mechanism (4.5). Compared to (4.5), the heterodyning speed adaption mechanism has the following advantages: 1) it has a lower computational cost, and 2) it is easier to design its PI gains because it only relies on the normalized values of the estimated EEMF components.

4.2.3 Adaptive Line Enhancer

Consider a noisy signal, which consists of a few desired sinusoidal components. When the frequencies of the sinusoidal components in the noisy signal are known, a fixed filter will be sufficient to extract the sinusoidal components. However, when the sinusoidal frequencies of the noisy signal, e.g., the EEMF components in Equation (4.6),

are unknown or time varying, an adaptive filter is required. The ALE [97] is a good candidate for such an adaptive filter. Consider that a noisy ALE input signal $x(n)$ contains X sinusoidal components and can be modeled as follows:

$$x(n) = \sum_{i=1}^{X} a_i \sin\left[\omega_i n + \theta_i\right] + v(n) \tag{4.7}$$

where ω_i, a_i, and θ_i are the frequency, amplitude, and phase angle of the i^{th} sinusoidal component; and $v(n)$ is the noise, which may not be white. Suppose that any two samples of the noise term which are more than M sampling intervals apart do not correlate with each other. In this case, the ALE is an M-step-ahead predictor. Figure 4.2 depicts the block diagram of the ALE, which predicts the sinusoidal components in $x(n)$, while filtering out the noise component. When the filter $W(z)$ is adapted to minimize the mean-square error between the output and input signals, the ALE will be a filter tuned to only extract the sinusoidal components. The output of the filter, $y(n)$, will be an approximation of the sum of the sinusoidal components. Consider Equation (4.6) again, if the currents and rotor speed are time-variant, the EEMF components can be modeled as the sums of all the sinusoidal components with different frequencies as follows:

$$\begin{bmatrix} E_\alpha(t) \\ E_\beta(t) \end{bmatrix} = \sum_{i=1}^{H} \begin{Bmatrix} -a_i \sin\left[\omega_i t + \theta_i(t)\right] + v_i(t) \\ a_i \cos\left[\omega_i t + \theta_i(t)\right] + v_i(t) \end{Bmatrix} \tag{4.8}$$

where ω_i, a_i, and $\theta_i(t)$ are the frequency, amplitude, and time-varying phase angle of the i^{th} component; $v_i(t)$ is the corresponding noise; and H is the number of sinusoidal components. The number of the filter taps, K, in Figure 4.2 should be greater than H; and the tap weight matrix, $\mathbf{w} = [w_0, w_1, \cdots, w_K]$, can be calculated online by using the well-known least-mean-square algorithm:

$$\mathbf{w}(n+1) = \mathbf{w}(n) + 2\mu e(n)x(n) \tag{4.9}$$

where μ is the step size for **w** adaption.

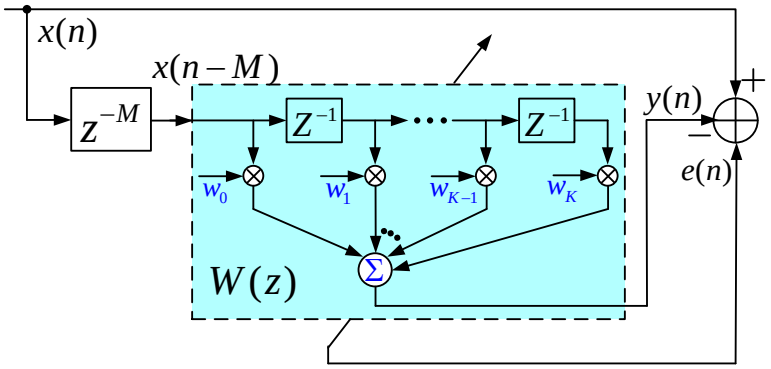

Figure 4.2: Block diagram of the ALE.

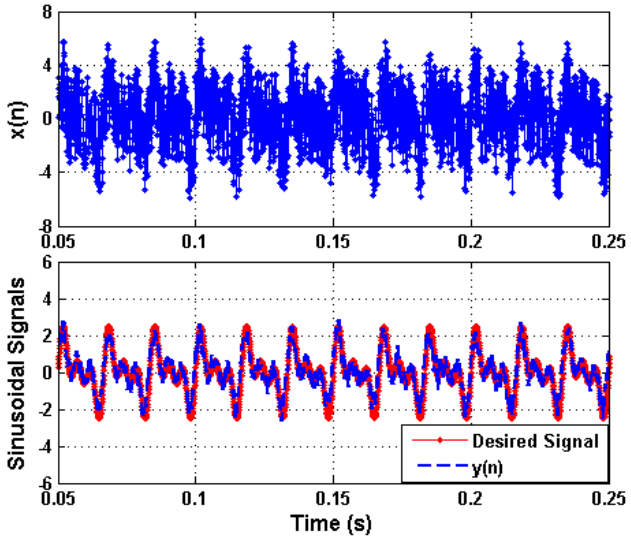

Figure 4.3: Simulation result of the filtering performance of ALE for artificial data input.

The simulation result for a simple case study is shown in Figure 4.3. The desired signal consists of three sinusoidal components with the frequencies of 60 Hz, 120 Hz, and 180 Hz, respectively. The power of the noise is equal to that of the desired signal. The

sampling frequency is 6 kHz. As the result shows, the ALE effectively filters out the noise content without any phase shift or magnitude decrease. The output of the ALE converges to the desired signal within 30 samples.

4.2.4 Heterodyning Speed Adaption Mechanism

In addition to the ALE, a heterodyning speed adaption mechanism is designed to replace Equation (4.5). Based on the two estimated EEMF components in the MRAS, $\hat{E}_{\alpha\beta}$ and $\tilde{E}_{\alpha\beta}$, the heterodyning speed adaption scheme can be expressed as:

$$\hat{\omega}_{re} = \left(k_p + \frac{k_i}{s} \right) \left(\hat{E}_\beta^n \tilde{E}_\alpha^n - \hat{E}_\alpha^n \tilde{E}_\beta^n \right) \tag{4.10}$$

where the superscript *n* stands for the normalized values of the quantities with respect to their amplitudes. Let $\hat{\theta}$ and $\tilde{\theta}$ represent the rotor positions obtained from $\hat{E}_{\alpha\beta}$ and $\tilde{E}_{\alpha\beta}$, respectively, and define:

$$\hat{E}_{\alpha\beta}^n = \begin{bmatrix} -\sin\hat{\theta} & \cos\hat{\theta} \end{bmatrix}^T \quad \text{and} \quad \tilde{E}_{\alpha\beta}^n = \begin{bmatrix} -\sin\tilde{\theta} & \cos\tilde{\theta} \end{bmatrix}^T \tag{4.11}$$

Substituting Equation (4.11) into Equation (4.10) yields:

$$\begin{aligned} \hat{\omega}_{re} = s\tilde{\theta} &= \left(k_p + \frac{k_i}{s} \right) \left(-\cos\hat{\theta}\sin\tilde{\theta} + \sin\hat{\theta}\cos\tilde{\theta} \right) \\ &= \left(k_p + \frac{k_i}{s} \right) \sin\left(\hat{\theta} - \tilde{\theta} \right) \xrightarrow{\Delta\theta = \hat{\theta} - \tilde{\theta} \approx 0} \approx \left(k_p + \frac{k_i}{s} \right) \Delta\theta \end{aligned} \tag{4.12}$$

Then the transfer function can be expressed as:

$$\frac{\tilde{\theta}}{\hat{\theta}} = \frac{k_p s + k_i}{s^2 + k_p s + k_i} \tag{4.13}$$

Equation (4.13) represents a second-order system which has one zero. The dynamic behavior of Equation (4.13) depends on the PI gains, which can be determined by properly placing the poles of the characteristic polynomial of the transfer function. Compared to the conventional speed adaption mechanism, Equation (4.5), the proposed scheme, Equation (4.10), consumes less computational time and is easier for digital system implementation. In addition, since Equation (4.10) relies on the normalized values of the estimated EEMF components whose amplitudes are limited within [−1, 1], it will be easier to design the PI gains compared to those when using Equation (4.5), which relies on the estimated EEMF components with varying amplitudes.

4.2.5 Overall Rotor Speed Estimator

The overall schematic diagram of the proposed rotor speed estimator, including the QSMO presented in Chapter 3, the ALE, the heterodyning speed adaption mechanism, and the adjustable model are shown in Figure 4.4. Proof of the stability of the proposed speed estimator using Popov's hyperstability criterion is provided in Appendix C. The proposed speed estimator has two operating modes, which are suitable for different applications. In Mode I (M1), the error feedback to the adjustable model is the difference between the normalized $\hat{E}^n_{\alpha\beta}$ and $\tilde{E}^n_{\alpha\beta}$. Due to the filtering effect of the ALE, the dynamic response of speed tracking will be slightly affected. However, the estimated speed will have less noise content, which results in a smooth speed profile. Therefore, M1 is suitable for generator applications in which the rotor speed of the generator is normally maintained by a prime mover machine; and the sensorless control performance is not sensitive to the estimated rotor speed.

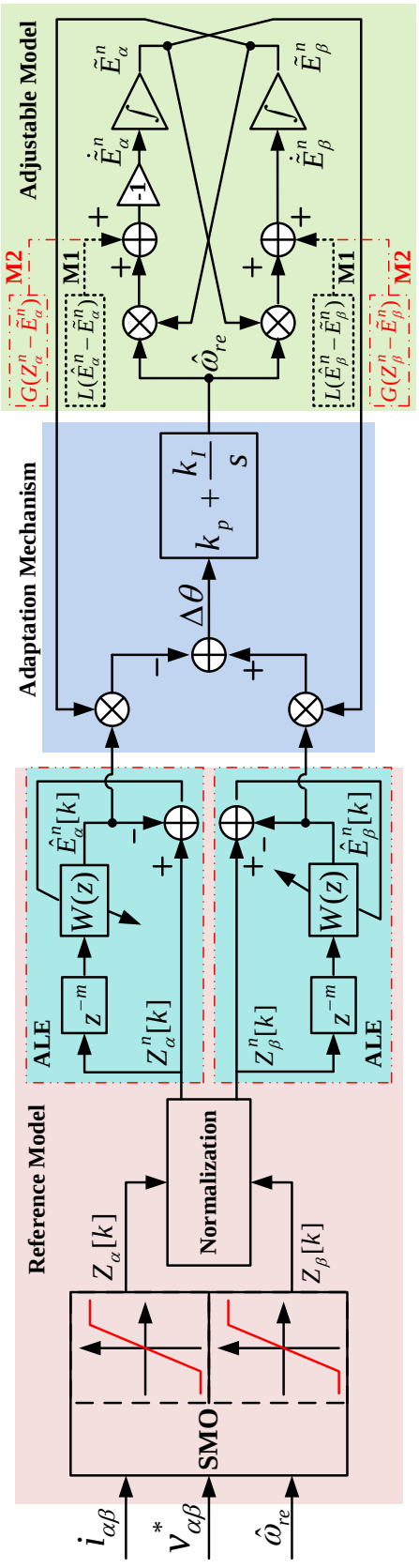

Figure 4.4: Schematic diagram of the proposed MRAS-based rotor speed estimator.

In Mode II (M2), the error feedback to the adjustable model is the difference between $Z_{\alpha\beta}^{n}$ and $\tilde{E}_{\alpha\beta}^{n}$. Since $Z_{\alpha\beta}^{n}$ is the unfiltered normalized output of the QSMO, sending $Z_{\alpha\beta}^{n}$ back to the adjustable model will force the output of the adjustable model to approach the unfiltered EEMF estimated from the QSMO. This scheme does not have the misadjustment caused by the ALE during abrupt speed changes and improves the dynamic response of speed tracking. However, the estimated rotor speed will have relatively larger noise content compared to that in M1, which will result in ripples in the estimated rotor speed. Mode II is suitable for motor drive applications, in which the sensorless control requires accurate rotor speed information without any delay, especially when the drive system is operated in the speed control mode.

4.3 Oscillation Mitigation Scheme for Rotor Position Estimation Using Estimated Rotor Speed Feedback

In a practical electric drive system, due to switching losses, EMI, and thermal issues in the inverter, as well as limited computational resources, the sampling ratio should be selected appropriately according to the system dynamics to guarantee fast response instead of for the sake of the control algorithms. When designing the rotor position estimator, there will be an oscillating error between the actual and estimated rotor positions if the rotor position is extracted from the EEMF estimated by a QSMO, which has a chattering problem. An appropriate method is needed to mitigate the oscillating rotor position estimation error.

As presented in Section 4.2.2, the rotor speed can be estimated by the proposed MRAS-based speed estimator. Note the estimated rotor speed in the i^{th} sampling period is $\hat{\omega}_{re}[i]$. In the steady state, suppose that the rotor speed is maintained as a constant during one sampling period, the change in the position during the i^{th} sampling period, $\Delta\theta_{\omega}[i]$, can be estimated as:

$$\Delta\theta_{\omega}[i] = \hat{\omega}_{re}[i] \times T_s[i] \tag{4.14}$$

where T_s is the sampling period. Equation (4.14) provides additional information on the change in the rotor position, which can be used to mitigate the oscillating problem of the rotor position obtained from the estimated EEMF.

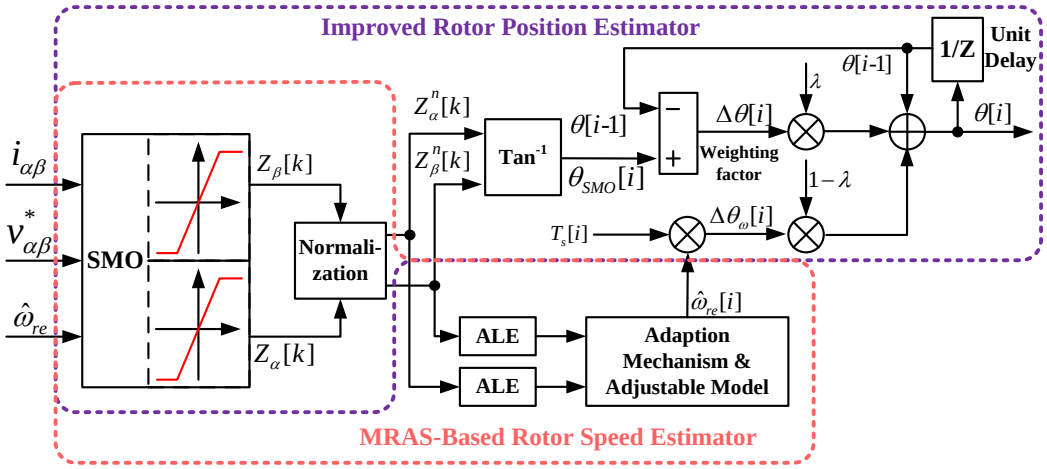

Figure 4.5: Schematic of the proposed improved rotor position estimator.

By using the rotor speed as a feedback input signal, the rotor position can be estimated as follows:

$$\theta[i] = \theta[i-1] + \lambda \times \Delta\theta[i] + (1-\lambda) \times \Delta\theta_{\omega}[i] \tag{4.15}$$

where $\theta[i]$ is the estimated rotor position in the i^{th} sampling period; $\theta[i–1]$ is the estimated rotor position in the previous sampling period; $\Delta\theta[i] = \theta_{SMO}[i] – \theta[i–1]$, where $\theta_{SMO}[i]$ is the rotor position obtained directly from the SMO-estimated EEMF components using the arctangent operation; and λ is a weighting factor used to adjust the contribution of the estimated speed in the position update. If λ=1, then $\theta[i] = \theta_{SMO}[i]$, which means that there is no speed feedback. Otherwise, if λ=0, the rotor position is updated by using the estimated speed feedback only. Figure 4.5 illustrates the schematic of the proposed improved rotor position estimator.

4.4 Summary

In this chapter, a robust MRAS-based rotor speed estimator using a heterodyning speed adaption mechanism for sensorless PMSM drives was discussed. The MRAS contains an improved reference model, which uses an ALE to provide a better noise cancellation capability for the EEMF estimated from a QSMO. The rotor speed estimator has two operating modes, which are suitable for generator and motor applications, respectively. Furthermore, a novel oscillation mitigation algorithm using the estimated rotor speed as a feedback input signal can work with the conventional inverse tangent method for rotor position estimation. This algorithm can mitigate the oscillations in the estimated rotor position caused by the noisy content in the estimated EEMF. The implementation of the proposed method is simple and has a low computational cost and, therefore, has great potential for industrial applications.

CHAPTER 5

SENSORLESS CONTROL OF NONSALIENT-POLE PMSMS AT LOW-SPEED USING HIGH-FREQUENCY SQUARE-WAVE VOLTAGE INJECTION

5.1 Introduction

In the Chapters 3 and 4, QSMO-based rotor position/speed estimators were discussed. However, similar to other model-based methods, the method investigated has poor performance or may even fail in the low-speed region and come to a standstill due to the low signal-to-noise ratio (SNR) of the system states. The saliency-based methods, which are particularly effective in the low-speed range, utilize the anisotropic properties of the PMSMs, e.g., the rotor saliency and/or the saturation of the stator iron. By using a pulsating [98] or rotating [99] HFSI, the anisotropic properties can be extracted, from which the rotor position can be estimated. Both sinusoidal and square waves [72], **Error! Reference source not found.** are effective candidates for the injected signals.

The conventional HFSI methods rely on a rotor position-dependent spatial saliency. For a salient-pole PMSM, e.g., an IPMSM, a position dependent spatial inductance distribution inherently exists. Thus, the HFSI methods are well suited for sensorless IPMSM drives. However, for a nonsalient-pole PMSM, e.g., a SPMSM, the spatial saliency is related to the saturation effect of the stator leakage flux or main flux **Error! Reference source not found.**. Due to the symmetric rotor structure of the SPMSM, the dependence of the inductance on the rotor position is weak. This leads to a

low SNR of the saliency-related signals, e.g., the amplitudes of the induced high-frequency (HF) current components in the dq or $\alpha\beta$ reference frame. Thus, when applying an HFSI method to an SPMSM, a narrow-bandwidth saliency tracking observer is required to extract the saliency-related signal. This results in a degradation of the performance of the sensorless drive. To solve this problem and improve the rotor position estimation performance, several adaptive or nonlinear observers have been proposed in [102], [103]. In recent years, instead of tracking the flux saturation, other physical attributes, e.g., the HF impedance [103] and the rotor and stator resistances related to the eddy current losses [104], [105], have been utilized for rotor position estimation.

This chapter describes injecting a pulsating voltage vector into an estimated $\gamma\delta$ rotor reference frame. In conventional methods [98] when a pulsating signal is injected into the γ axis, a position-related signal, i.e., the error between the estimated and actual rotor positions, can be detected from the induced HF δ-axis current. However, the magnitude of the induced HF δ-axis current depends on the machine asymmetry. Therefore, conventional methods are not effective for SPMSMs.

This chapter describes a method of extracting the rotor position from the envelopes of the HF current signals induced in the stationary reference frame. This method is much less dependent on the machine asymmetry than the conventional method and, therefore, is well suited for SPMSMs, especially when the difference between the HF impedances on different axes is negligible. Since only the envelopes of the HF currents are used, the method injects a HF square-wave voltage signal, instead of a HF sinusoidal voltage signal. This increases the upper bandwidth of the sensorless speed controller, which is desired in practical applications.

5.2 High-Frequency Model of Nonsalient-pole PMSM

The dynamics of a nonsalient-pole PMSM can be expressed in a *dq* rotating reference frame as:

$$\begin{bmatrix} v_d \\ v_q \end{bmatrix} = \begin{bmatrix} R_s + L_s p & -\omega_{re} L_s \\ \omega_{re} L_s & R_s + L_s p \end{bmatrix} \begin{bmatrix} i_d \\ i_q \end{bmatrix} + \begin{bmatrix} 0 \\ \omega_{re} \lambda_m \end{bmatrix} \tag{5.1}$$

where p is the derivative operator; v_d and v_q are the stator voltages; i_d and i_q are the stator currents; ω_{re} is the rotor electrical angular rotating speed in rad/s; L_s is the stator inductance; and R_s is the stator resistance. If HF voltage signals, $v_{d,h}$ and $v_{q,h}$, whose frequency is sufficiently higher than the electrical rotating frequency of the machine, are injected into the machine stator windings, HF currents, $i_{d,h}$ and $i_{q,h}$, will be generated. To reduce extra losses, vibration, and acoustic noise during the normal operation of the drive system, the amplitudes of the injected voltage signals are usually much smaller than that of the fundamental stator voltages, so as the amplitudes of the induced currents. However, due to the high frequency, the derivatives of the induced currents can be quite large. Therefore, when considering the HF components of a machine operating in the low-speed region and at standstill, the off-diagonal cross-coupling terms in Equation (5.1) are much smaller than the diagonal terms and, therefore, can be ignored. Similarly, in the low-speed region and at standstill, the back EMF term can also be ignored. Consequently, the HF model of the nonsalient-pole PMSM in the low-speed region and standstill can be expressed as:

$$\begin{bmatrix} v_{d,h} \\ v_{q,h} \end{bmatrix} = \begin{bmatrix} Z_{d,h} & 0 \\ 0 & Z_{q,h} \end{bmatrix} \begin{bmatrix} i_{d,h} \\ i_{q,h} \end{bmatrix} \tag{5.2}$$

where $Z_{d,h} = R_{d,h} + j\omega_h \cdot L_{d,h}$ and $Z_{q,h} = R_{q,h} + j\omega_h \cdot L_{q,h}$ are the d-axis and q-axis HF impedances, respectively; ω_h is frequency of the injected signals; $R_{d,h}$ and $R_{q,h}$ are the d-axis and q-axis HF resistances, respectively; and $L_{d,h}$ and $L_{q,h}$ are the d-axis and q-axis HF inductances, respectively.

5.3 High-Frequency Pulsating Signal Injection

In this section, the HF impedance model, Equation (5.2), is used to derive the expression of the induced HF currents for rotor position estimation. The HF pulsating voltage vector is injected into the estimated $\gamma\delta$ rotating reference frame. The angle between the γ axis and the α axis, which is aligned with the direction of the phase A magnetic axis, is defined as the estimated rotor position, as shown in Figure 5.1. The error between the actual and estimated rotor positions is denoted as $\Delta\theta$.

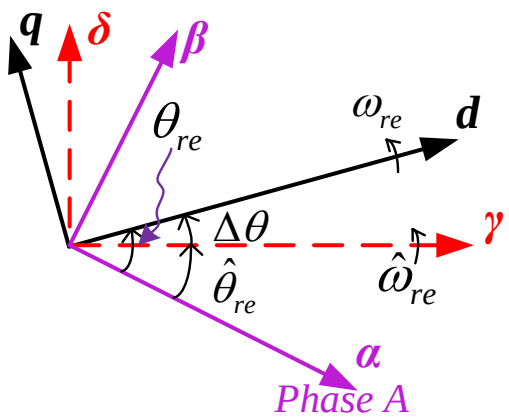

Figure 5.1: Relationships among the $\alpha\beta$ stationary reference frame, the ideal dq rotor reference frame, and the estimated $\gamma\delta$ rotor reference frame.

The conventional rotor position estimator using the HF sinusoidal voltage injection is briefly presented in this section. This method highly depends on the rotor

saliency and, thus, is not effective for nonsalient-pole PMSMs. To solve this problem, a rotor position estimator which is much less dependent on the rotor spatial saliency was investigated. The estimator is first discussed based on a HF sinusoidal voltage injection. A HF square-wave voltage injection scheme to replace the sinusoidal voltage injection scheme to improve the upper bandwidth of the sensorless speed control is then discussed.

5.3.1 High-Frequency Sinusoidal Signal Injection

A HF sinusoidal voltage vector, described by Equation (5.3), is injected into the $\gamma\delta$ reference frame.

$$v_{\gamma\delta,h} = \begin{bmatrix} v_{\gamma,h} \\ v_{\delta,h} \end{bmatrix} = V_h \begin{bmatrix} \cos(\omega_h t) \\ 0 \end{bmatrix} \tag{5.3}$$

where ω_h and V_h are the frequency and amplitude of the injected voltage vector. Projecting $v_{\gamma\delta,h}$ onto the *d*- and *q*- axes, the resulting voltage vector, $v_{dq,h}$, can be expressed as:

$$v_{dq,h} = \begin{bmatrix} v_{d,h} \\ v_{q,h} \end{bmatrix} = \begin{bmatrix} \cos(\Delta\theta) & \sin(\Delta\theta) \\ -\sin(\Delta\theta) & \cos(\Delta\theta) \end{bmatrix} \begin{bmatrix} v_{\gamma,h} \\ v_{\delta,h} \end{bmatrix} = v_{\gamma,h} \begin{bmatrix} \cos(\Delta\theta) \\ -\sin(\Delta\theta) \end{bmatrix} \tag{5.4}$$

According to Equations (5.2) and (5.4), the induced HF currents in the ideal *dq* reference frame can be determined.

$$\begin{bmatrix} i_{d,h} \\ i_{q,h} \end{bmatrix} = v_{\gamma,h} \begin{bmatrix} \cos(\Delta\theta)/Z_{d,h} \\ -\sin(\Delta\theta)/Z_{q,h} \end{bmatrix} \tag{5.5}$$

In the conventional method, the rotor position information is extracted from the induced HF current signals in the $\gamma\delta$ reference frame as follows:

$$\begin{bmatrix} i_{\gamma,h} \\ i_{\delta,h} \end{bmatrix} = \begin{bmatrix} \cos(\Delta\theta) & -\sin(\Delta\theta) \\ \sin(\Delta\theta) & \cos(\Delta\theta) \end{bmatrix} \begin{bmatrix} i_{d,h} \\ i_{q,h} \end{bmatrix} = v_{\gamma,h} \begin{bmatrix} \dfrac{\cos^2(\Delta\theta)}{Z_{d,h}} + \dfrac{\sin^2(\Delta\theta)}{Z_{q,h}} \\ \dfrac{\left(Z_{q,h} - Z_{d,h}\right)}{2Z_{d,h}Z_{q,h}} \sin(2\Delta\theta) \end{bmatrix} \tag{5.6}$$

As shown in Equation (5.6), the rotor position estimation error, $\Delta\theta$, is contained in $i_{\delta,h}$. However, the magnitude of $i_{\delta,h}$ depends on the rotor saliency, which is small for an SPMSM. To illustrate this, finite-element analysis was performed to investigate the spatial saliency property of an SPMSM with HF voltage signals injected. The SPMSM had 6 poles, 18 slots, and distributed windings. A 1-V, 400-Hz sinusoidal pulsating voltage vector was injected into the *d* axis. The spatial distribution of the HF impedance, as shown in Figure 5.2(a), presented a rotor position-dependent characteristic. For this case, $(Z_{q,h} - Z_{d,h})/(Z_{q,h} + Z_{d,h}) = 5.15\%$. Such a rotor saliency ratio, however, is too small for accurate position estimation. Increasing the magnitude and frequency, e.g., using 800 Hz, of the injected signal increased the saliency ratio, as shown in Figure 5.2(b), which, however, resulted in higher losses and increased harmonics in the terminal voltages of the inverter.

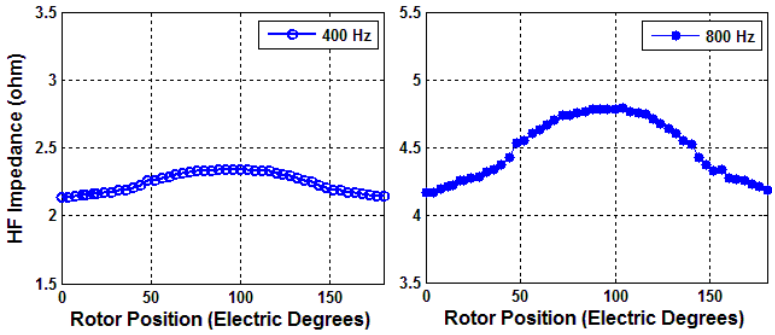

Figure 5.2: Comparisons of spatial distributions of HF impedance with 400 Hz and 800 Hz injected signals.

5.3.2 Position Estimation Using Envelopes of $i_{\alpha\beta,h}$

Since the rotor saliency of an SPMSM is small, i.e., $(Z_{q,h} - Z_{d,h}) \ll (Z_{q,h} + Z_{d,h})$, as discussed in Section 5.3.1, Equation (5.6) is not effective for rotor position estimation due to the low SNR of the saliency-related signal. To solve this problem, a better position observation method which has lower dependence on the rotor saliency is needed for SPMSMs in the low-speed region.

In the method investigated, the rotor position was obtained from the induced current vector, $i_{\alpha\beta,h}$, in the $\alpha\beta$ reference frame as follows:

$$\begin{aligned} i_{\alpha\beta,h} &= \begin{bmatrix} i_{\alpha,h} \\ i_{\beta,h} \end{bmatrix} = \begin{bmatrix} \cos(\theta_{re}) & -\sin(\theta_{re}) \\ \sin(\theta_{re}) & \cos(\theta_{re}) \end{bmatrix} \begin{bmatrix} i_{d,h} \\ i_{q,h} \end{bmatrix} \\ &= V_h \cos(\omega_h t) \begin{bmatrix} \dfrac{\cos(\Delta\theta)}{Z_{d,h}} \cos(\theta_{re}) + \dfrac{\sin(\Delta\theta)}{Z_{q,h}} \sin(\theta_{re}) \\ \dfrac{\cos(\Delta\theta)}{Z_{d,h}} \sin(\theta_{re}) - \dfrac{\sin(\Delta\theta)}{Z_{q,h}} \cos(\theta_{re}) \end{bmatrix} \end{aligned} \tag{5.7}$$

If the position error, $\Delta\theta$, is small enough such that $\sin(\Delta\theta) \approx 0$ and $\cos(\Delta\theta) \approx 1$, then Equation (5.7) can be simplified as:

$$\begin{bmatrix} i_{\alpha,h} \\ i_{\beta,h} \end{bmatrix} \approx \frac{V_h \cos(\omega_h t)}{Z_{d,h}} \begin{bmatrix} \cos(\theta_{re}) \\ \sin(\theta_{re}) \end{bmatrix} \tag{5.8}$$

As shown in Equation (5.8), if the rotating frequency of the machine is much smaller than the frequency of the injected signal, the envelopes of $i_{\alpha\beta,h}$ are position-dependent signals. Thus, if the envelopes are extracted, the rotor position can be obtained.

Since for an SPMSM, the difference between $Z_{d,h}$ and $Z_{q,h}$ can be ignored (i.e., $Z_{d,h} \approx Z_{q,h} \approx Z_{s,h}$), Equation (5.7) can be simplified as follows:

$$\begin{bmatrix} i_{\alpha,h} \\ i_{\beta,h} \end{bmatrix} = \frac{V_h \cos(\omega_h t)}{Z_{s,h}} \begin{bmatrix} \cos(\theta_{re} - \Delta\theta) \\ \sin(\theta_{re} - \Delta\theta) \end{bmatrix} = \frac{V_h \cos(\omega_h t)}{Z_{s,h}} \begin{bmatrix} \cos(\hat{\theta}_{re}) \\ \sin(\hat{\theta}_{re}) \end{bmatrix} \tag{5.9}$$

Equations (5.8) and (5.9) are both simplified versions of Equation (5.7). Although they are derived based on different assumptions, both of them indicate that the rotor position information can be directly obtained from the envelopes of $i_{\alpha\beta,h}$, if a HF pulsating voltage vector is injected in the $\gamma\delta$ reference frame.

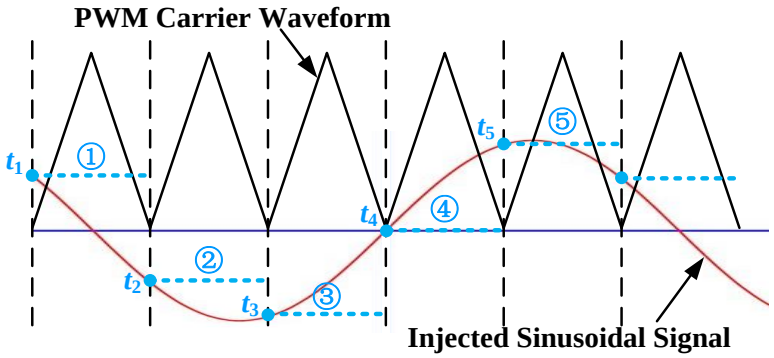

Figure 5.3: Relationships between a PWM carrier signal and an injected sinusoidal signal.

In practical applications, the conventional HFSI method, which injects a sinusoidal voltage signal, often suffers from the problem of a narrow bandwidth, due to the limited PWM switching frequency. Figure 5.3 illustrates the relationship between an injected sinusoidal signal and a PWM carrier waveform. Assume that at standstill and in the low-speed region, the PWM switching frequency, which is the same as the current sampling frequency, is 2.5 kHz. As shown in Figure 5.3, the frequency of the injected signal is 500 Hz, such that there are only five samples in one period of the injected sinusoidal signal. Thus, the resulting discrete-time waveform, i.e., the dash-line waveform, is far from a sinusoidal signal. This will become worse if the frequency of the injected signal further increases. As a consequence, the analysis presented early in this

section will no longer be valid. Therefore, the highest frequency of the injected sinusoidal signal is limited by the PWM switching frequency, which further limits the upper bandwidth of the sensorless speed controller [72].

5.3.3 High-Frequency Square-Wave Signal Injection

As described by Equations (5.8) and (5.9), only the envelopes of $i_{\alpha\beta,h}$ are needed to extract the rotor position information. The envelopes are mainly made up of the extremes of the current waveforms, which correspond to the maxima and minima of the injected voltage signal, i.e., the values at t_5 and t_3, respectively. Other values of the injected voltage signal, e.g., the values at t_1, t_2 and t_4, are not critical. To increase the bandwidth of the sensorless speed controller, this chapter describes a method of injecting a square-wave voltage signal, as shown in Figure 5.4. The highest frequency of the injected square-wave signal is more than twice the frequency of the injected sinusoidal signal. If the sampling frequency and control loop frequency are doubled, i.e., the reference values of the voltages v_d and v_q are updated twice per PWM cycle, the highest frequency of the injected square-wave signal will be equal to the PWM frequency.

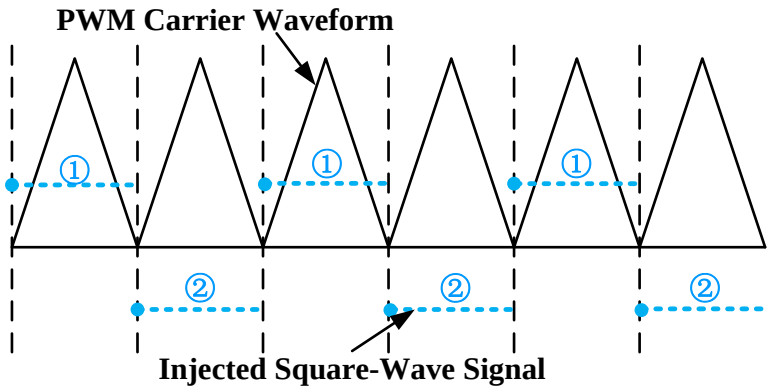

Figure 5.4: Relationships between a PWM carrier signal and an injected square-wave signal.

A square-wave voltage vector, as illustrated in Figure 5.4 and expressed as

$$v_{\gamma\delta,h} = \begin{bmatrix} v_{\gamma,h} \\ v_{\delta,h} \end{bmatrix} = V_h \begin{bmatrix} (-1)^n \\ 0 \end{bmatrix} \tag{5.10}$$

is injected into the γ and δ axes, where n is the index of the PWM cycles. When n is odd,

$$\begin{bmatrix} v_{d,h} \\ v_{q,h} \end{bmatrix} = V_h \begin{bmatrix} -\cos(\Delta\theta) \\ \sin(\Delta\theta) \end{bmatrix} \quad \text{and} \quad \begin{bmatrix} i_{d,h} \\ i_{q,h} \end{bmatrix} = V_h \begin{bmatrix} -\cos(\Delta\theta)/Z_{d,h} \\ \sin(\Delta\theta)/Z_{q,h} \end{bmatrix} \tag{5.11}$$

Then,

$$\begin{bmatrix} i_{\alpha,h} \\ i_{\beta,h} \end{bmatrix} = V_h \begin{bmatrix} -\dfrac{\cos(\Delta\theta)}{Z_{d,h}}\cos(\theta_{re}) - \dfrac{\sin(\Delta\theta)}{Z_{q,h}}\sin(\theta_{re}) \\ -\dfrac{\cos(\Delta\theta)}{Z_{d,h}}\sin(\theta_{re}) + \dfrac{\sin(\Delta\theta)}{Z_{q,h}}\cos(\theta_{re}) \end{bmatrix} \tag{5.12}$$

If $Z_{d,h} \approx Z_{q,h} \approx Z_{s,h}$, Equation (5.12) can be further simplified as:

$$\begin{bmatrix} i_{\alpha,h} \\ i_{\beta,h} \end{bmatrix} = \frac{V_h}{Z_{s,h}} \begin{bmatrix} -\cos(\theta_{re} - \Delta\theta) \\ \sin(\theta_{re} - \Delta\theta) \end{bmatrix} = \frac{V_h}{Z_{s,h}} \begin{bmatrix} -\cos(\hat{\theta}_{re}) \\ \sin(\hat{\theta}_{re}) \end{bmatrix} \tag{5.13}$$

When n is even,

$$\begin{bmatrix} v_{d,h} \\ v_{q,h} \end{bmatrix} = V_h \begin{bmatrix} \cos(\Delta\theta) \\ -\sin(\Delta\theta) \end{bmatrix} \quad \text{and} \quad \begin{bmatrix} i_{d,h} \\ i_{q,h} \end{bmatrix} = V_h \begin{bmatrix} \cos(\Delta\theta)/Z_{d,h} \\ -\sin(\Delta\theta)/Z_{q,h} \end{bmatrix} \tag{5.14}$$

Then,

$$\begin{bmatrix} i_{\alpha,h} \\ i_{\beta,h} \end{bmatrix} = V_h \begin{bmatrix} \dfrac{\cos(\Delta\theta)}{Z_{d,h}}\cos(\theta_{re}) + \dfrac{\sin(\Delta\theta)}{Z_{q,h}}\sin(\theta_{re}) \\ -\dfrac{\cos(\Delta\theta)}{Z_{d,h}}\sin(\theta_{re}) - \dfrac{\sin(\Delta\theta)}{Z_{q,h}}\cos(\theta_{re}) \end{bmatrix} \tag{5.15}$$

If $Z_{d,h} \approx Z_{q,h} \approx Z_{s,h}$, Equation (5.15) can be further simplified as:

$$\begin{bmatrix} i_{\alpha,h} \\ i_{\beta,h} \end{bmatrix} = \frac{V_h}{Z_{s,h}} \begin{bmatrix} \cos(\theta_{re} - \Delta\theta) \\ -\sin(\theta_{re} - \Delta\theta) \end{bmatrix} = -\frac{V_h}{Z_{s,h}} \begin{bmatrix} -\cos(\hat{\theta}_{re}) \\ \sin(\hat{\theta}_{re}) \end{bmatrix} \tag{5.16}$$

According to Equations (5.13) and (5.16), the final expression for the $i_{\alpha\beta,h}$ is expressed as:

$$\begin{bmatrix} i_{\alpha,h} \\ i_{\beta,h} \end{bmatrix} = \frac{V_h}{Z_{s,h}} \begin{bmatrix} \cos(\theta_{re} - \Delta\theta) \\ -\sin(\theta_{re} - \Delta\theta) \end{bmatrix} = (-1)^n \frac{V_h}{Z_{s,h}} \begin{bmatrix} -\cos(\hat{\theta}_{re}) \\ \sin(\hat{\theta}_{re}) \end{bmatrix} \tag{5.17}$$

Then by detecting the envelopes of the current components in Equation (5.17), the estimated rotor position can be extracted as follows:

$$\begin{cases} \tilde{i}_{\alpha,h} = -\dfrac{V_h}{Z_{s,h}} \cos(\hat{\theta}_{re}) \\ \tilde{i}_{\beta,h} = +\dfrac{V_h}{Z_{s,h}} \sin(\hat{\theta}_{re}) \end{cases} \quad \text{and} \quad \hat{\theta}_{re} = -\tan^{-1}\left(\frac{\tilde{i}_{\beta,h}}{\tilde{i}_{\alpha,h}}\right) \tag{5.18}$$

where $\tilde{i}_{\alpha,h}$ and $\tilde{i}_{\beta,h}$ are the envelopes of $i_{\alpha,h}$ and $i_{\alpha,h}$, respectively.

5.3.4 Integrated Rotor Position and Speed Observer

As shown in Equation (5.18), the arctangent algorithm is the most straightforward rotor position extraction method, which, however, is easily affected by the measurement and process noise. To solve this problem, an improved, integrated, rotor position and speed observer is designed in this section. Define $\tilde{i} = \begin{bmatrix} \tilde{i}_{\alpha,h} & \tilde{i}_{\beta,h} \end{bmatrix}^T$. Since $\dot{\tilde{i}} = \hat{\omega}_{re} J \cdot \tilde{i}$, where $J = \begin{bmatrix} 0 & -1 \\ 1 & 0 \end{bmatrix}$, a linear observer can be designed as follows:

$$\dot{\hat{i}} = \hat{\omega}_{re} J \cdot \hat{i} + G \cdot \left(\tilde{i} - \hat{i}\right) \tag{5.19}$$

where $\hat{i} = \begin{bmatrix} \hat{i}_{\alpha,h} & \hat{i}_{\beta,h} \end{bmatrix}^T$ is the output of the observer, Equation (5.19), which is a vector of sinusoidal currents; $\hat{\omega}_{re}$ is the estimated electrical rotor speed; $G = \begin{bmatrix} G_{11} & G_{12} \\ G_{21} & G_{22} \end{bmatrix}$ is the gain

matrix of the observer, Equation (5.19), which can be configured by using a linear observer design technique, e.g., pole assignment. Then the rotor speed is estimated by using double integration of the observer tracking error as follows.

$$\hat{\omega}_{re} = \left(k_p + \frac{k_i}{s} \right) \frac{k_s}{s} \left(\tilde{i} \times \hat{i} \right) \tag{5.20}$$

where × denotes cross-product. The rotor position is then estimated from the estimated rotor speed as follows.

$$\hat{\theta}_{re} = \frac{1}{s} \left[\hat{\omega}_{re} + k \left(\tilde{i} \times \hat{i} \right) \right] \tag{5.21}$$

Based on (5.19)-(5.21), the transfer function from the actual rotor position to the estimated rotor position can be derived as:

$$\frac{\hat{\theta}_{re}}{\theta_{re}} = \frac{k s^2 + k_p k_i s + k_i^2}{s^3 + k s^2 + k_p k_i s + k_i^2} \tag{5.22}$$

According to the characteristic polynomial of Equation (5.22), the key parameters, k, k_p, and k_i, of the position/speed observer, can be selected properly according to the requirements, e.g., frequency response, of the position/speed observer.

5.4 Summary

In this chapter, a HF square-wave voltage injection-based rotor position estimator for nonsalient-pole PMSMs, e.g., SPMSMs, operating in the low-speed range has been presented. In the estimator, the HF square-wave voltage signal is injected in the estimated rotor reference frame; the rotor position is then estimated from the envelopes of the induced HF current components in the stationary reference frame. Compared to conventional methods, the proposed position estimator is much less dependent on the rotor spatial saliency. Therefore, it is well suited for SPMSM applications. By using the square-wave signal injection, the operating speed range of the speed controller can be at least twice higher than that when using sinusoidal signal injection.

CHAPTER 6

SIMULATION MODEL AND EXPERIMENT TEST SETUP

Simulation studies performed in Matlab Simulink® and experimental tests were utilized to validate the effectiveness of all methods presented in this dissertation. There were three major sets of Simulink models, including (1) a model used to verify the sensorless drive using EEMF-based QSMO, (2) a model used to verify the sensorless drive using extended flux-based QSMO, and (3) a model used to validate a sensorless SPMSM drive in low-speed operation. Accordingly, there were three sets of experimental test setups, including (1) a 150 kW IPMSM test stand, (2) a 200 W salient-pole PMSM test stand, and (3) a 2.4 kW SPMSM test stand. In this chapter, the simulation models, e.g., overall sensorless drive system and control software, and the test stands, e.g., the parameters of motors, the structure and connection of the stands, are described.

6.1 Simulation Model of Sensorless IPMSM Drive Using EEMF-Based QSMO

The adaptive EEMF-based QSMO was integrated into the current-regulated space vector control of the IPMSM, leading to a sensorless control system for the IPMSM, as shown in Figure 6.1. This sensorless control system was simulated using Matlab Simulink®. The machine parameters were measured from the test IPMSM, and specifications for the IPMSM are shown in Table 6.1. The rotor position was obtained from the QSMO-based position estimator; the rotor speed was then calculated by using the estimated rotor position. A PI speed regulator was used to generate the torque

command from the speed tracking error. If the IPMSM was operated in the torque control mode, the torque percentage could be commanded directly instead of being generated from the outer-loop speed control. The base torque is the maximum torque at each speed point and was obtained by using a 2-dimensional (2-D) lookup table. Since the inverter DC-link voltage also affected the current command, a speed-voltage ratio was used. The current commands were generated by two lookup tables based on torque percentage and speed-voltage ratio. Other modules of the control system included current PI regulators with feedforward voltage compensation, Park transformation, SVPWM generator, etc.

Table 6.1. Specifications for the IPMSM.

Maximum power	150 kW	Stator resistance	0.01 Ω
Maximum torque	300 Nm	Base speed	5000 RPM
Flux linkage	0.095 Wb	Pole pairs number	4
Average *d*-axis inductance	0.2 mH	Average *q*-axis inductance	0.55 mH

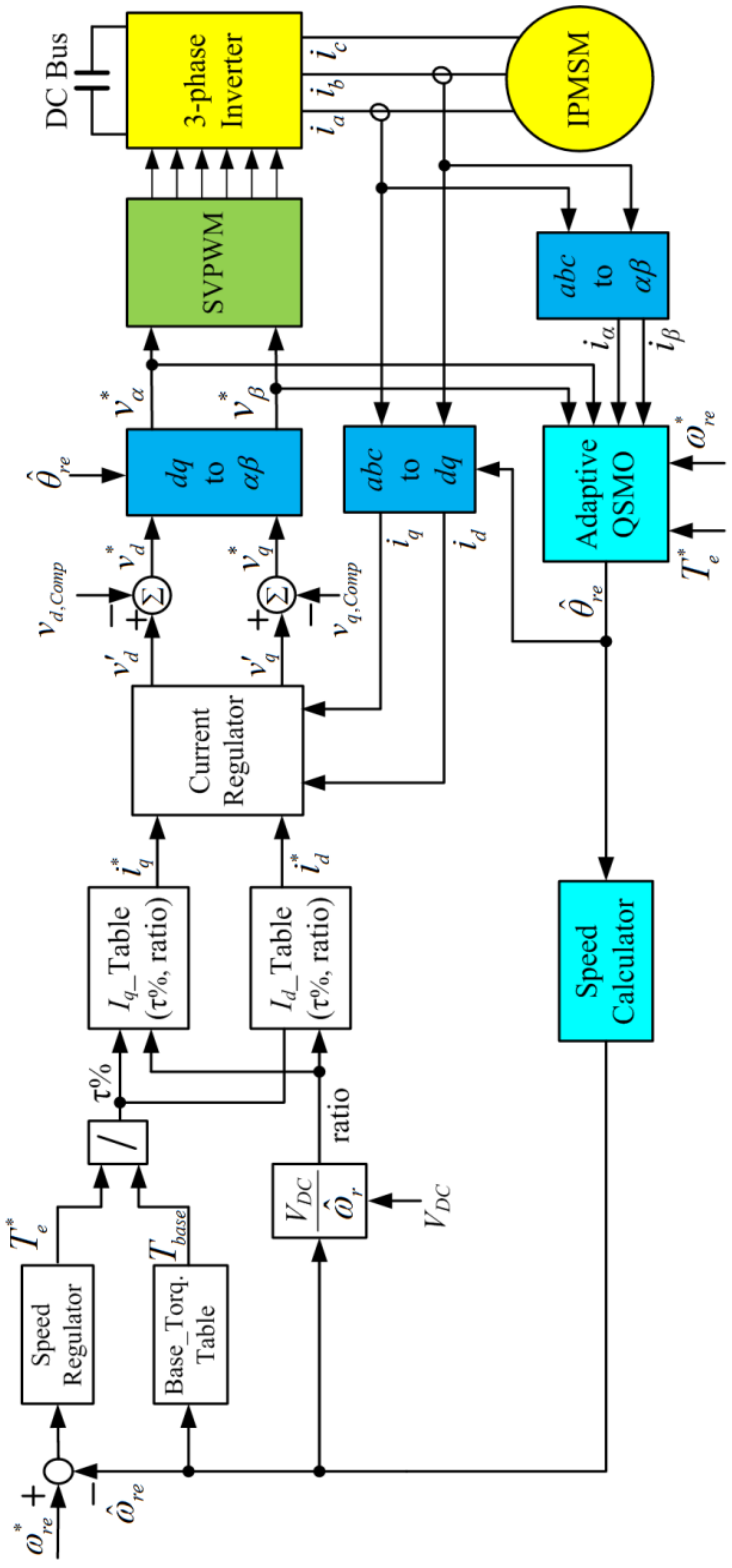

Figure 6.1: Block diagram of the sensorless IPMSM drive using EEMF based QSMO.

6.2 Simulation Model of Sensorless PMSM Drive Using Extended Flux-Based QSMO

As presented in Section 3.5, the sensorless drive system using an extended-flux-based QSMO should have better dynamic performance and low-speed operating capability than the sensorless drive using EEMF-based methods. Therefore, the simulation studies were conducted to compare the performance of three different rotor position estimators: the rotor position estimator using extended flux-based QSMO, the rotor position estimator without the dynamic position compensator, and the EEMF-based rotor position estimator proposed in [107]. The corresponding estimated rotor positions are denoted as $\hat{\theta}_1$, $\hat{\theta}_2$, and $\hat{\theta}_3$, respectively. The parameters of the salient-pole PMSM used in the simulation are listed in Table 6.2. The overall sensorless control framework was the same as the one presented in Section 6.1. However, the rotor position/speed estimators, machine parameters, and 2-D current lookup tables were changed accordingly.

Table 6.2. Specifications for the salient-pole PMSM.

Rated power	3 hp	Stator resistance	3.1 Ω
Rated torque	12 Nm	Rated speed	1250 RPM
Flux linkage	0.452 Vs/rad	Pole pairs number	3
Average *d*-axis inductance	38.6 mH	Average *q*-axis inductance	58.1 mH

6.3 Simulation Model of Sensorless SPMSM Drive Using HF Square-Wave Signal Injection

Figure 6.2 shows the overall block diagram of the sensorless control system for an SPMSM operating in the low-speed region. The HF square-wave signal injection-based rotor position/speed estimator was integrated with a standard space vector control system, similar to the control system described in Section 6.1.

To estimate the rotor position in the low-speed region, a HF square-wave voltage signal, described by Equation (5.10), was added to the fundamental *d*-axis reference voltage generated by the current regulator. The resultant phase currents, i_a, i_b and i_c, contained HF components. Low-pass filters were used to filter out the HF components; the resultant fundamental current components were sent back to the current regulators. Therefore, the control performance was not affected by the injected signals.

In the rotor position/speed estimator, the currents $i_{\alpha\beta}$ were obtained from the unfiltered i_a, i_b, and i_c. A band-pass filter (BPF) was used to extract the current components $i_{\alpha\beta,h}$ at the frequency of the injected signal. The envelope detector was then used to obtain the envelopes of $i_{\alpha\beta,h}$, which contained the information on the rotor position. The envelope detector can be designed by using a squaring and low-pass filtering scheme or the Hilbert transform [108]. In practical applications, a suitable zero-order hold is also an alternative to envelope detection [108].

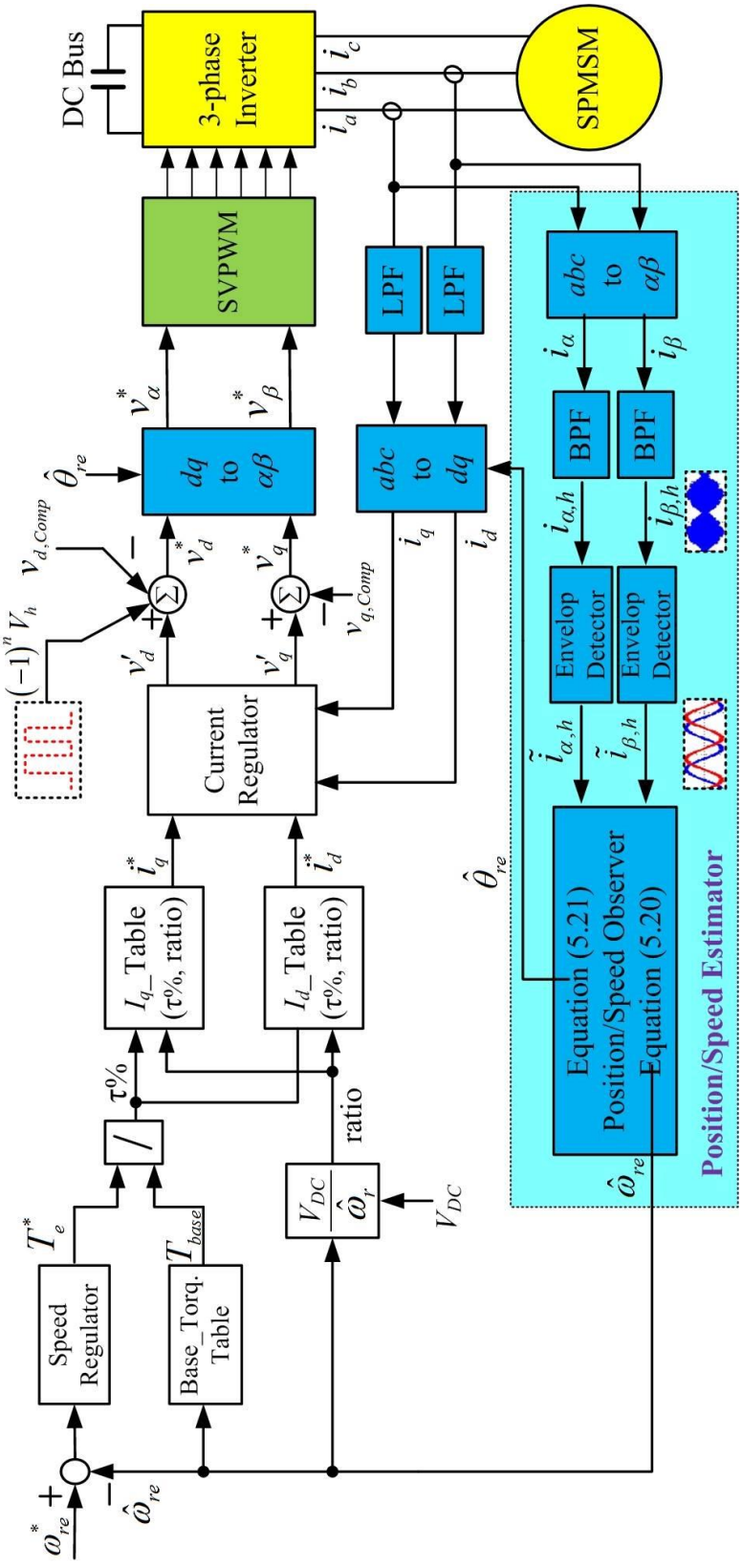

Figure 6.2: The overall block diagram of the proposed sensorless SPMSM drive system for low-speed operation.

6.4 Test Setup for Sensorless IPMSM Drive Using EEMF-Based QSMO

An experimental stand was designed to validate the adaptive EEMF-based QSMO, as shown in Figure 6.3. In the test stand, a prime mover machine and an IPMSM were connected back to back sharing a common DC-bus from a power supply. The DC-bus voltage was 700 V. The prime mover machine maintained the shaft speed while the IPMSM worked in the torque control mode. The parameters of the IPMSM are listed in Table 6.1. Considering current regulation quality, switching losses, system efficiency, switching noise, and EMI issues, the PWM frequency was selected as 6 kHz. The sampling frequency for the currents was the same as the PWM switching frequency. The QSMO was executed once per PWM cycle. Since the commanded voltages were used in the QSMO instead of the measured IPMSM terminal voltages, the IGBT dead-time effect caused a phase shift between the estimated and measured rotor positions. In the test stand, the IGBT dead-time effect of the inverter was fully compensated. Therefore, using the commanded voltages is the same as using the measured IPMSM terminal voltages [109]. In this test stand, a high-resolution resolver is mounted on the rotor shaft to measure the rotor position information. However, the measured position is only used to evaluate the performance of proposed position estimation system.

According to the parameters listed in Table 6.1, a suitable value was determined for α, according to (3.26). Suppose that the highest torque slew rate for the IPMSM drive system is 20000 Nm/s at the base speed. When the commanded torque increases with the maximum slew rate form 0 Nm to the full load of 300 Nm within 15 ms and i_q^* correspondingly increases from 0 A to 350 A, then pi_q = 23 kA/s. If i_d = 0, then $\beta = \omega_{re}\psi_m$

/(L_d−L_q) = 142 kA/s. Therefore, α was calculated to be 1.16 and was chosen to be 1.2 in the experiments.

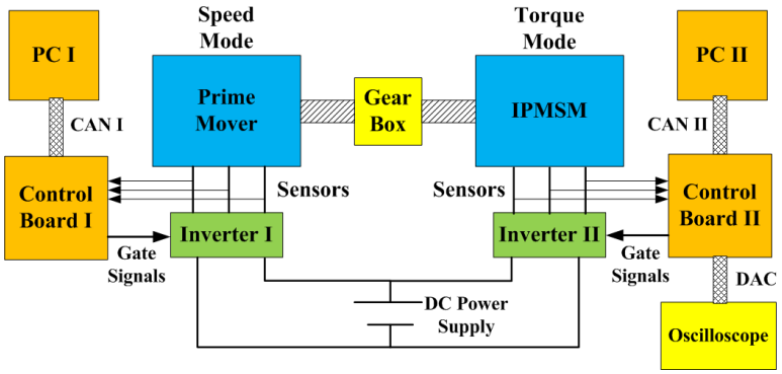

Figure 6.3: Schematic of the test stand for the sensorless IPMSM drive.

6.5 Test Setup for Sensorless PMSM Drive Using Extended Flux-Based QSMO

An experimental test stand, Figure 6.4(a), was designed to validate the proposed rotor position/speed sensorless control system using the extended flux-based QSMO. A schematic of the overall test stand setup is shown in Figure 6.4(b), which includes a 200-W salient-pole PMSM connected back to back with a 200-W DC machine. The DC machine can work as either a prime mover machine (motor) or a load machine (DC generator). The two machines shared one common DC-bus, whose voltage was maintained at 40 V by a DC power supply. The specifications for the DC motor and the PMSM are listed in Table 6.3. The overall control algorithm was implemented in a dSPACE 1104 real-time control system. The PWM switching frequency at the rated speed was 5 kHz. The phase currents were sampled twice per PWM cycle; and the main control software, e.g., basic vector control, rotor position estimation, etc., was also executed twice per PWM cycle. All of the experimental results were recorded by using

ControlDesk installed on a laboratory computer, which was connected with the dSPACE system. Two different rotor position estimators, i.e., the proposed extended flux-based rotor position estimator and the EEMF-based rotor position estimator proposed in [107], were both implemented in the control software. In the experiments, when the rotor position estimated by one of the two position estimators was used as the control angle, the other position estimator was disabled. The rotor position was also measured by an encoder, which was mounted on the rotor shaft of the PMSM. However, the measured rotor position was only used for evaluation purposes and was not used by the sensorless control algorithm.

Table 6.3. Specifications for the DC motor and the test salient-pole PMSM.

Specifications	DC Motor	Salient-Pole PMSM
Rated Speed	3500 RPM	3000 RPM
Rated Power	200 W	200 W
EMF Constant	0.0087 V/RPM	0.0095 V/RPM
Stator Resistance	0.39 Ω	0.23 Ω
Inductance(s)	Armature Inductance 0.67 mH	Ld = 0.275 mH; L_q = 0.364 mH
No. of Pole Pairs	N/A	4

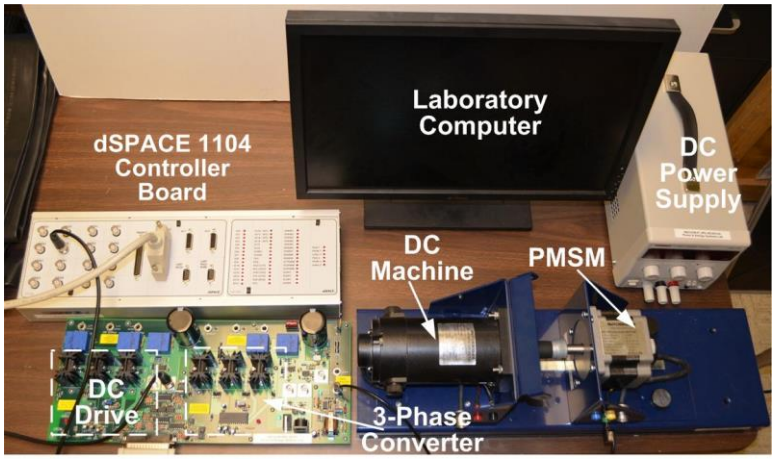

(a)

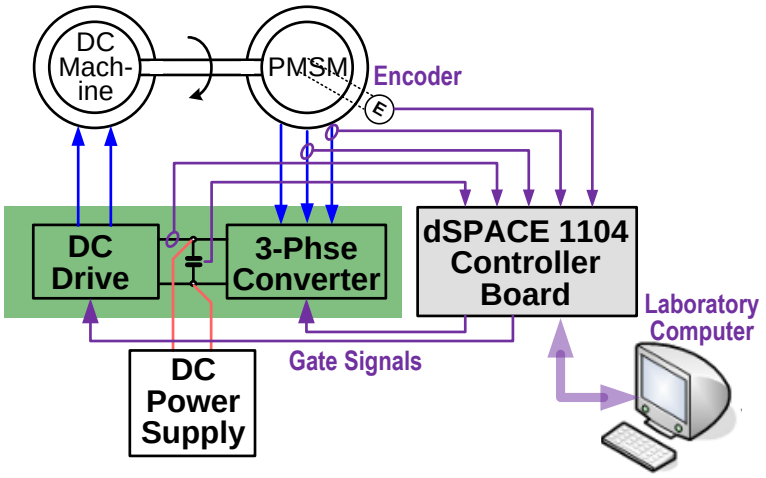

(b)

Figure 6.4: Overall test stand setup (a) an experimental setup and (b) a schematic.

6.6 Test Setup for Sensorless SPMSM Drive Using HF Square-Wave Signal Injection

An experimental test stand, as shown in Figure 6.5(a), was designed to verify the effectiveness of the HF square-wave voltage injection-based rotor position/speed estimator and overall sensorless drive system. In the test stand, two identical 2.4-kW SPMSMs were connected back to back. The test machine (SPMSM No. 1) had its own controller and converter (inverter/rectifier) board. The test machine worked as a generator or a motor; and both the sensorless speed and torque controls were performed on the test machine. Figure 6.5(b) illustrates the schematic diagram of the test stand when test machine worked under sensorless torque control mode as a generator. In this setup, the shaft speed was maintained by SPMSM No. 2 using a synchronous drive. The converter was used as a rectifier connected with a DC electronic load. When the test machine

worked under sensorless speed control mode as a motor, the converter board was used as an inverter and connected to the DC power supply.

The test SPMSM has 42 magnetic poles, and its cross-section is shown in Figure 6.5(c). Other machine parameters are listed in Table 6.4. In the experiments, the rotor position was measured from an absolute encoder with 8192 steps per mechanical revolution for comparison purposes. The overall control algorithm was implemented in a dSPACE 1005 real-time control system with a sampling period of 100 μs. All of the experimental results were recorded using ControlDesk interfaced with dSPACE 1005 and a laboratory computer.

Table 6.4. Specifications for the SPMSM and sensorless drive system,

Nominal power	2.4 kW	Stator resistance	1.5 Ω
Number of pole-pairs	21	Base speed	300 RPM
d-axis inductance	0.87 mH	*q*-axis inductance	0.91 mH
Saliency ratio	2.25%	DC bus voltage	80 V

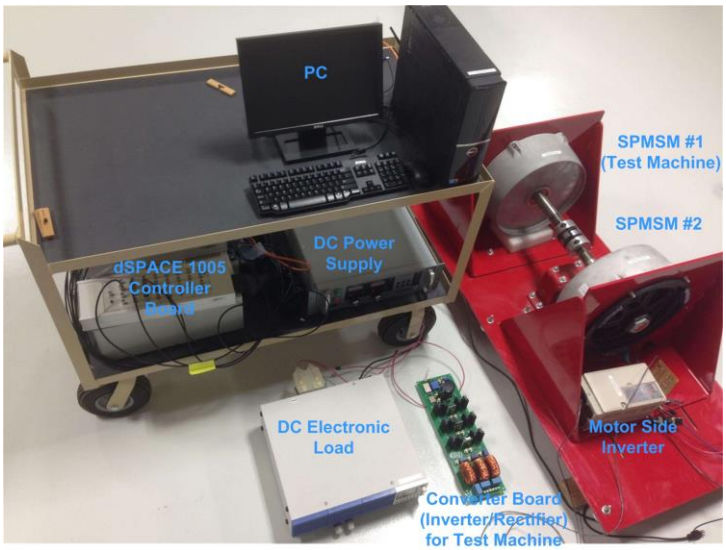

(a)

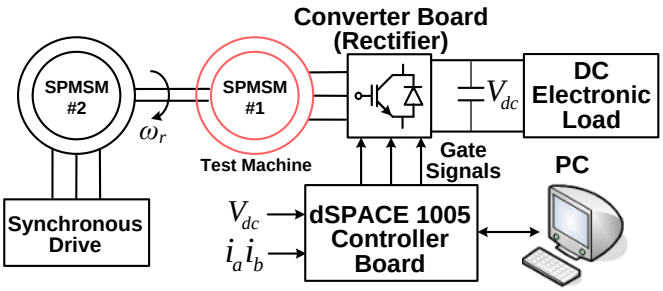

(b)

(c)

Figure 6.5: Test stand setup: (a) overall test stand, (b) schematic of the overall test stand, and (c) cross section of the 42-pole test SPMSM.

CHAPTER 7

SIMULATION AND EXPERIMENTAL VALIDATION

In this chapter, numerous simulation and experimental results are presented to verify the effectiveness of the methods developed and the associated algorithms. In addition, the problems observed during the simulations and experiments are also discussed. Corresponding root cause analysis and solutions are also included.

7.1 Simulation Studies for Sensorless IPMSM Drive Using EEMF-Based QSMO

7.1.1 Effect of Different Widths of the Boundary Layer

The IPMSM was operated under free shaft condition at 4,000 RPM with a PWM frequency of 6,000 Hz. According to Equation (3.19), $Z_{\min} = 28$. Three groups of Z_0 and l were selected by keeping lZ_0 as a constant:

1. $Z_0 = 30$ and $l = 12{,}000$, where Z_0 was slightly larger than $Z_{\min}$; and the resulting QSMO should have had the best tracking performance.
2. $Z_0 = 60$ and $l = 6{,}000$, where Z_0 was larger than $2Z_{min}$; and the resulting QSMO should have had larger tacking errors than that of the first group, but the tracking errors were smaller than 60.
3. $Z_0 = 15$ and $l = 24{,}000$, where Z_0 was smaller than $Z_{\min}$, which meant that the upper boundary of lZ_0 specified by Equation (3.18-II) was not satisfied.

According to the discussions in the Section 3.4.2, for the last group, the estimated currents could still track the measured current i_α and i_β in the right direction; however, the

tracking errors would not be limited by the designed boundary layer. The simulation results in Figure 7.1 verify the previous discussion. When Z_0 = 30, the α-axis current tracking error was limited within 30 A. hen Z_0 = 60, the α-axis current tracking error was also limited by the defined boundary, which, however, was larger than the previous one. When Z_0 = 15, the α-axis current tracking error could not be limited within 15 A and diverged to more than 100 A. The β-axis current tracking errors demonstrated similar features for the three cases.

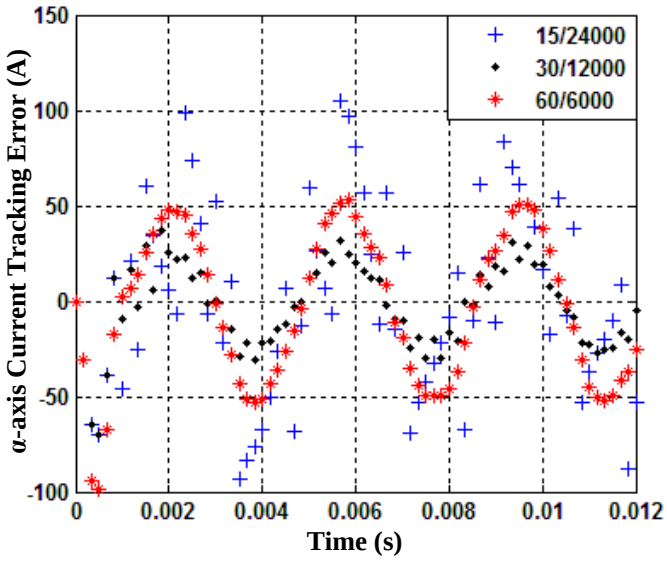

Figure 7.1: Simulation comparison of current tracking errors for different combinations of Z_0 and l (constant lZ_0) when the IPMSM operated under free shaft condition at 4,000 RPM.

7.1.2 Adaptive QSMO During Rotor Speed Variations

In the QSMO, the value of Z_0 was adapted to the change in the rotor speed, as shown in Figure 7.2. In the low- and medium-speed region, e.g., 0 ~ 2,500 RPM, Z_0 was kept as a constant of 20 for convenience, since in this speed range decreasing Z_0 had no obvious effect on the performance of the QSMO. In the higher speed region, e.g., from 2,500 to 5,500 RPM, Z_0 was selected as a linear function of the speed. The adaptive Z_0 was used for the simulation, where the rotor speed increased linearly from the initial value of 2,000 RPM at 0.5 s to the final value of 5,500 RPM at 4 s and then remained constant at this speed.

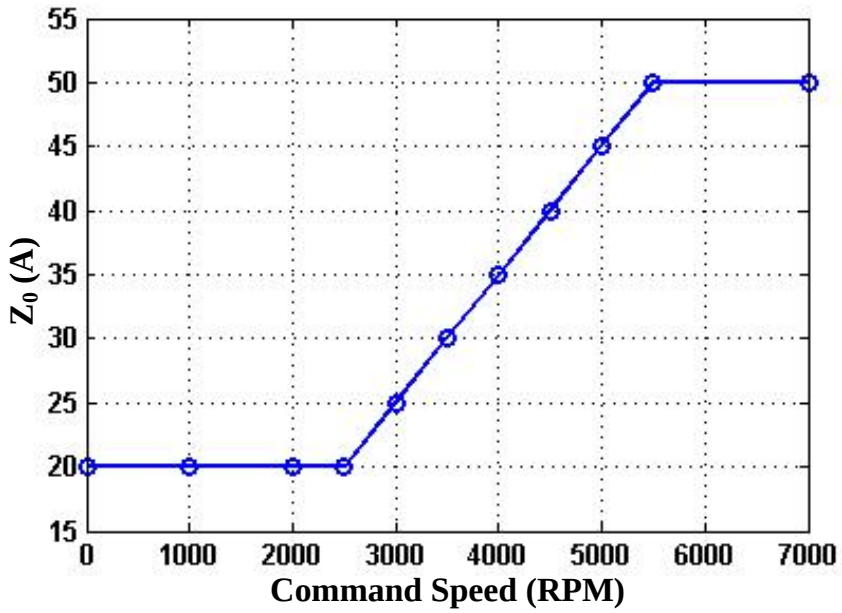

Figure 7.2: Adaption of Z_0 to speed variation.

During the simulation, the load was kept at a constant of 100 Nm. Figure 7.3(a) shows the profile of the commanded speed. The corresponding EEMF estimated by the

adaptive QSMO is shown in Figure 7.3(b), whose amplitude increased with the speed. According to Figure 7.3(c), the error between the QSMO-estimated and the measured positions was always limited within +/−3 electrical degrees. This indicates that the QSMO with the adaptive Z_0 could limit the current tracking errors within the designed boundary and had excellent performance over a wide speed range, i.e., is robust to speed variations. These results cannot be achieved by using classic SMOs [54].

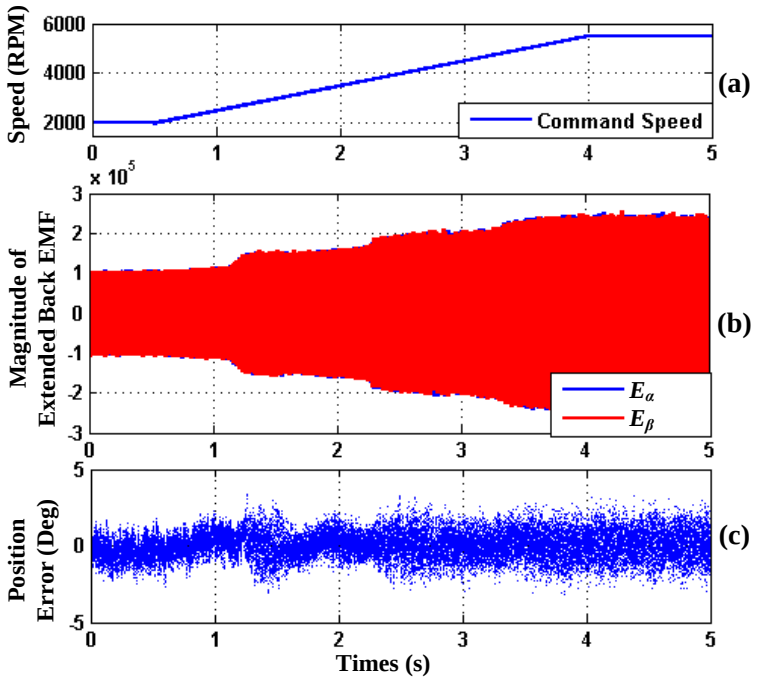

Figure 7.3: Simulation results during ramp change in rotor speed: (a) commanded speed, (b) estimated EEMF, and (c) position estimation error.

7.1.3 Adaptive QSMO During Torque Variations

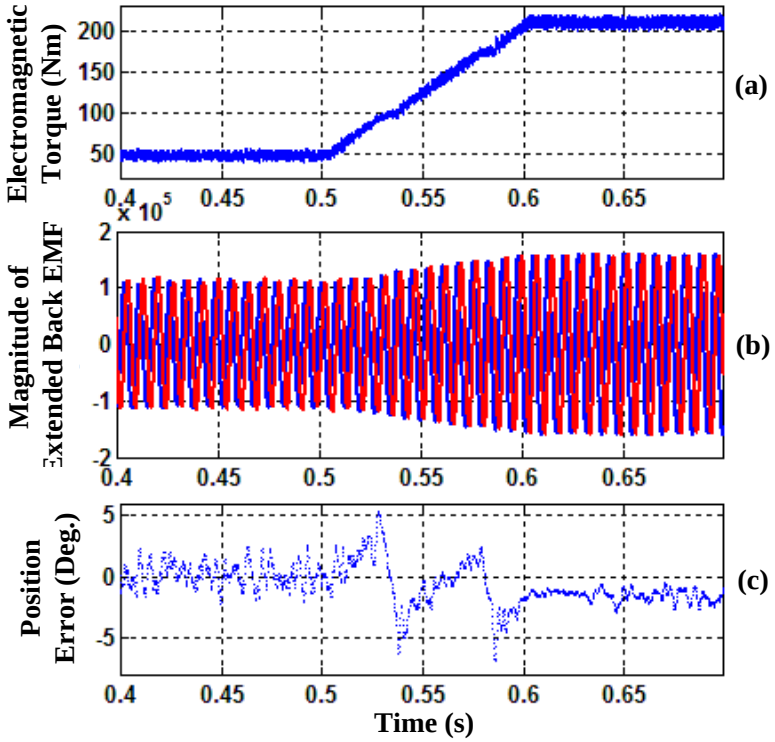

Figure 7.4: Simulation results during load variation: (a) electromagnetic torque, (b) estimated EEMF, and (c) position estimation error.

In this simulation, the electromagnetic torque produced by the IPMSM increased almost linearly from a steady-state value of 50 Nm at 0.5 s to another steady-state value of 200 Nm at 0.6 s. The slew rate for torque increase was 1,500Nm/s, and the speed of the IPMSM was maintained at 2,000 RPM. The torque profile is shown in Figure 7.4(a). As Figure 7.4(b) shows, the amplitude of EEMF increased with the torque. According to Equations (3.22) and (3.23), the QSMO parameters were selected as follows: l = 10,000 and Z_0 = 7.5 when T_e = 50 Nm; and l = 10,000 and Z_0 = 30 when T_e = 200 Nm. The resulting position error profile is shown in Figure 7.4(c). Since the QSMO parameters

were properly adapted by using the proposed method, the performance of the QSMO had no degradation in steady state when the load changed. The position error was a little larger during the load transition but was still limited within +/− 5 electrical degrees.

7.2 Experimental Results for Sensorless IPMSM Drive Using EEMF-Based QSMO

To fully validate the performance of the sensorless drive system using the proposed adaptive QSMO, four groups of testing results were presented.

1. *System steady-state performance*: verified the zero-phase-lag (between the estimated and measured positions) behavior for different load levels at the base speed, where zero phase lag meant that the average position estimation error was zero.
2. *System dynamic performance* under ramp load changes with different slew rates, including 400 Nm/s, 2000 Nm/s, and 4000 Nm/s.
3. *System steady-state and dynamic performance* in four quadrants of operation: verified the symmetrical operation characteristics of the sensorless drive system
4. *System dynamic performance* under complete torque reversals: verified the ride-through capability of the sensorless drive system during large load variations.

Furthermore, experimental results for the sensorless drive system using the conventional DSMO, i.e., using a conventional discretized reaching law and without the parameter adaption scheme in Figure 3.5, under a torque ramp change and complete torque reversal with the highest slew rate of 4000 Nm/s are provided at the end of this

section to further demonstrate the steady-state and dynamic performance and stability improvement of the sensorless drive system using the adaptive QSMO.

7.2.1 Steady-State Performance

In order to evaluate the zero-phase-lag behavior of the adaptive QSMO over the full load range, a set of torque ramp change tests were performed at base speed by increasing the torque command linearly with the same slew rate of 400 Nm/s from zero to different steady-state values, as shown in Figure 7.5. First, the parameters of the QSMO, l and Z_0, were designed for the free-shaft condition. The QSMO with the fixed parameters, i.e., without the parameter adaption scheme, was used for sensorless control of the IPMSM for each torque ramp change test; the resulting position estimation errors are shown in Figure 7.5 as well. The QSMO without the parameter adaption scheme could guarantee a zero phase lag under the free-shaft condition where the parameters were designed. However, phase lags, i.e., negative position estimation errors, were observed at other loading conditions. As shown in Figure 7.5, the phase lag increased nonlinearly with the steady-state torque level. At the maximum torque, the phase lag reached 50 electric degrees. In comparison, the adaptive QSMO was also applied for sensorless control of the IPMSM for each torque ramp change test; and the resulting position estimation errors are shown in Figure 7.6. The position estimation error always oscillated within +/− 5 degrees around zero degree and had no phase lags in any torque ramp change case.

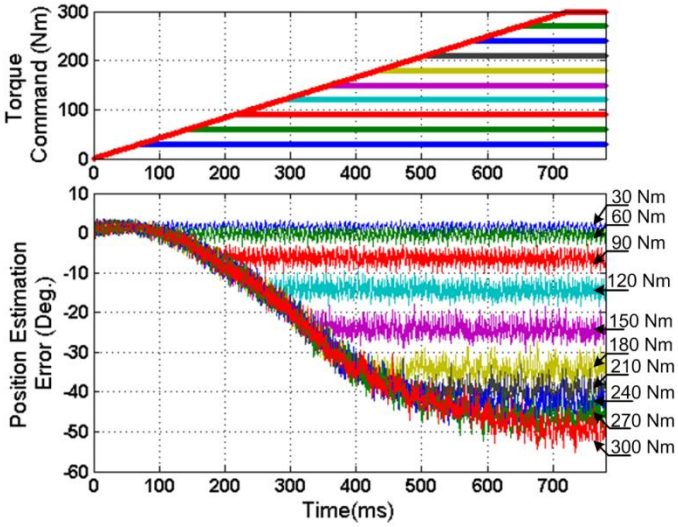

Figure 7.5: Phase lags, i.e., negative position estimation errors, at different steady-state torque levels using the QSMO without the parameter adaption scheme.

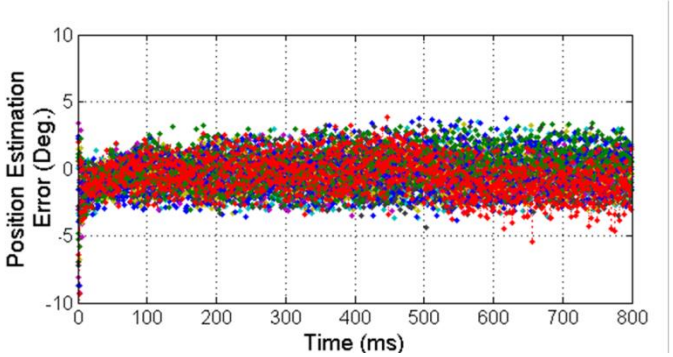

Figure 7.6: Position estimation errors showing zero-phase-lag behavior in torque ramp change tests using the adaptive QSMO.

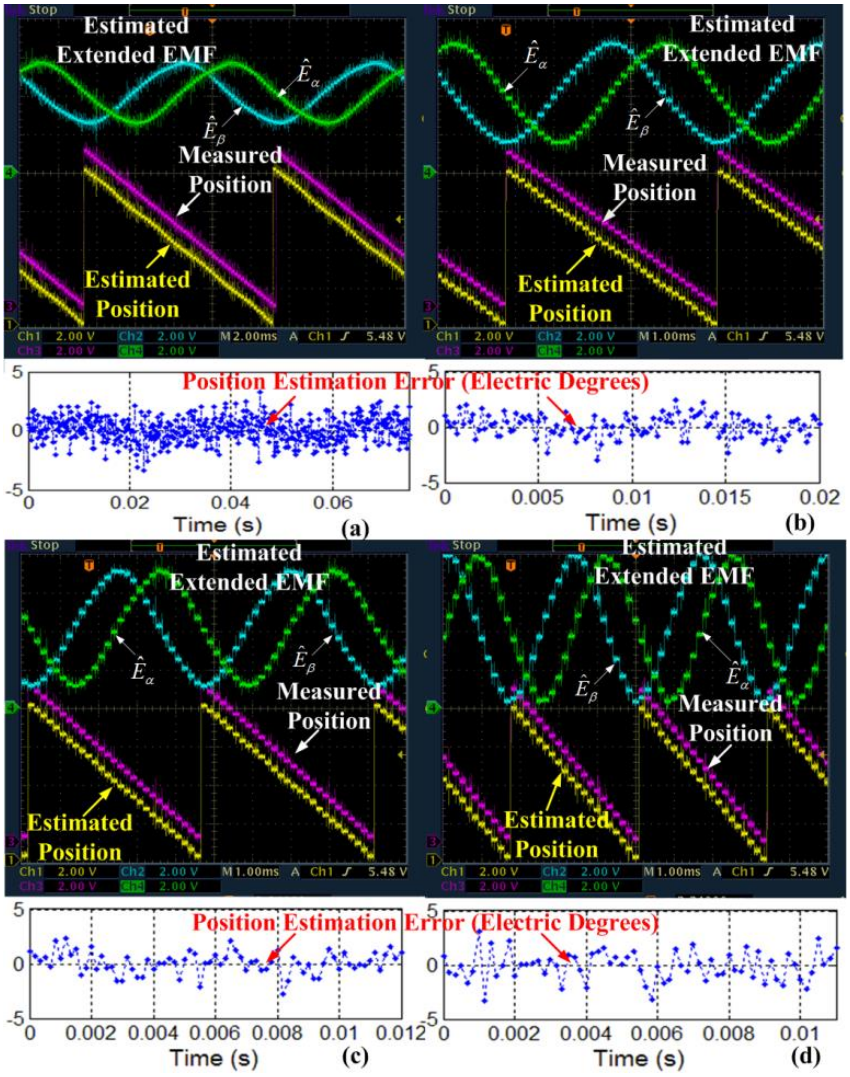

Figure 7.7: Experimental results of the estimated EEMF components, estimated and measured rotor positions, and position estimation errors under different speeds when f_s = 6 kHz: (a) 500 RPM, (b) 1500 RPM, (c) 3000 RPM, and (d) 4500 RPM.

Figure 7.7 shows the performance of the proposed adaptive QSMO under free shaft condition at different operating speed. The PWM frequency was maintained at 6 kHz to evaluate the impact of speed variations on the QSMO performance at a constant sampling frequency. Since the fundamental frequency of the EEMF components increased proportionally with the speed but the sampling frequency was the same for

different speed conditions, the number of control cycles per electrical revolution of the QSMO for the highest speed case (4,500 RPM), in Figure 7.7(d), was only 1/9 of that for the lowest speed case (500 RPM), in Figure 7.7(a). Therefore, the estimated EEMF components became more discontinuous when the speed increased. However, by using the parameter adaption scheme, the performance of the QSMO, as demonstrated by the position estimation errors in Figure 7.7, had no degradation from low speed to high speed. It should be pointed out that the sampling frequency for the QSMO should be high enough to ensure accurate position estimation but should not be a very large value for the sake of algorithm implementation. In practice, a reasonable sampling ratio between 15 and 20 can ensure acceptable position estimation accuracy, e.g., position estimation errors less than 4 electric degrees, for the QSMO, where the sampling ratio was defined to be the number of samples per electrical revolution. This can be obtained from the testing results shown in Figure 7.7.

7.2.2 Dynamic Performance under Torque Ramp Changes

In this set of tests, positive ramp changes from zero to the maximum value of 300 Nm with different slew rates were applied to the torque command. Since the prime mover machine maintained a negative speed, i.e., $d\theta_{re}/dt < 0$, when the torque is positive, the IPMSM worked in the braking mode as a generator. The current tracking performance, including the trajectories of the current commands i_d^* and i_q^*, as well as the actual currents i_d and i_q, is shown in Figure 7.8 for three torque ramp change cases with the slew rate of 400 Nm/s, 2000 Nm/s and 4000 Nm/s, respectively. In all of the scenarios, the sensorless drive system presented consistent steady-state current tracking errors. To observe the dynamic performance clearly, the trajectories of the actual currents corresponding to three different cases and the trajectory of the current command are shown in Figure 7.9. Since the same PI gains were used for the feed-forward current regulators in Figure 6.1 for all cases, the system had a relatively larger current tracking error at the beginning for the torque ramp change case with a higher slew rate. However, all three current trajectories converged towards the command current trajectory and tracked the current command precisely.

The initial stage, which is the area in the blue dashed-line circle in Figure 7.9, was critical to the sensorless drive, especially under fast changing load conditions [110]. In this region, the current regulation experienced a transient stage, which further introduced an oscillating error to the position estimation and may have causes instability of the system. The proposed parameter adaption scheme made the QSMO have zero-phase-lag

behavior at different load levels. This ensured that the QSMO worked in the desired sliding surface regardless of the load conditions [110].

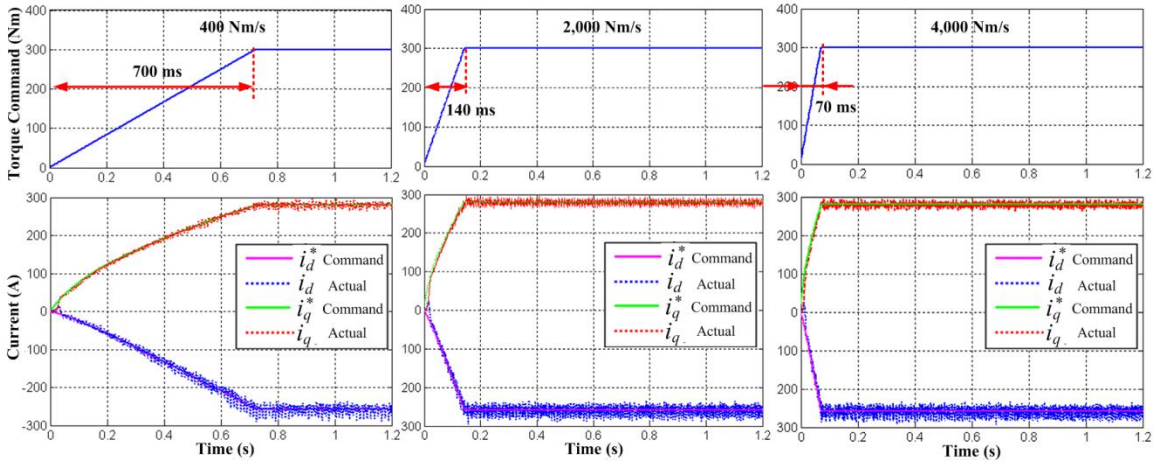

Figure 7.8: Current tracking performance under three torque ramp change scenarios.

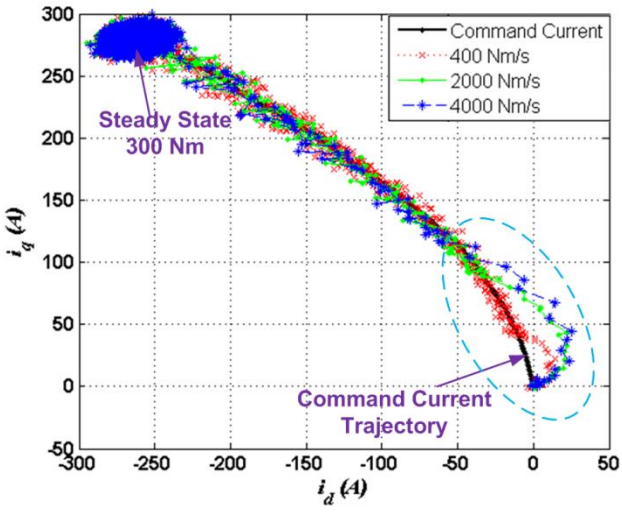

Figure 7.9: Current trajectories for three torque ramp change scenarios.

7.2.3 Four-Quadrant Operations

As shown in Figure 6.1, lookup tables are used to generate commanded currents from torque command. The lookup tables were first generated from the MTPA profile and then tuned on the test stand to guarantee proper operating points. For the test stand used in this work, the operating points for the motoring mode and braking mode were symmetrical in the lookup tables. Therefore, the sensorless drive system was expected to have symmetrical behavior under four-quadrant operations, where the four-quadrant operating conditions were defined as:

- *Q1 Motoring* with positive speed and positive torque
- *Q2 Braking* with negative speed and positive torque
- *Q3 Motoring* with negative speed and negative torque
- *Q4 Braking* with positive speed and negative torque

In this set of tests, a ramp change with a slew rate of −4000 Nm/s or 4000 Nm/s was applied to the torque command for each quadrant of operation. As Figure 7.10 shows, the sensorless drive system was always stable, and the errors between the estimated and measured rotor positions had no steady-state offset for all of the cases. The position estimation error was also in an acceptable range during the load transient of each case.

The responses, i.e., speed and position estimation error, of the system in the two motoring modes (Q1 and Q3) and two braking modes (Q2 and Q4) were symmetrical with each other. However, the transient stages, i.e., the position tracking settling time of the QSMO, of the motoring modes were slightly longer than those of the braking modes. This was caused by the variation of DC bus voltage. In the braking modes, the DC bus

voltage was higher than 700 V. However, in the motoring modes, due to the large inertia, the prime mover machine did not have fast enough dynamic response to supply power needed for IPMSM motoring, which resulted in both relatively larger speed oscillations and DC bus voltage drops. The DC-bus voltage drops will further affect the transient performance of the sensorless IPMSM drive in the motoring modes.

7.2.4 Complete Torque Reversal

Complete torque reversal is always one of the toughest tests for evaluating the ride-through capability of a sensorless drive system under a large load transient. In a complete torque reversal test, the fast changing load, the cross-zero of torque, and sudden shaft speed change will significantly affect the performance of the sensorless control system. What's worse, if the IPMSM transmits from the full, i.e., maximum torque and base speed, braking mode to the full motoring mode, it will always consume DC power, which will cause a larger DC voltage drop than when the IPMSM transmits from the full motoring mode to the full braking mode. As discussed in the Section 7.2.2, this will introduce disturbances into the drive system and result in a relatively longer transient stage. If the sensorless drive system is not robust enough, instability will occur, which will easily trigger over current faults.

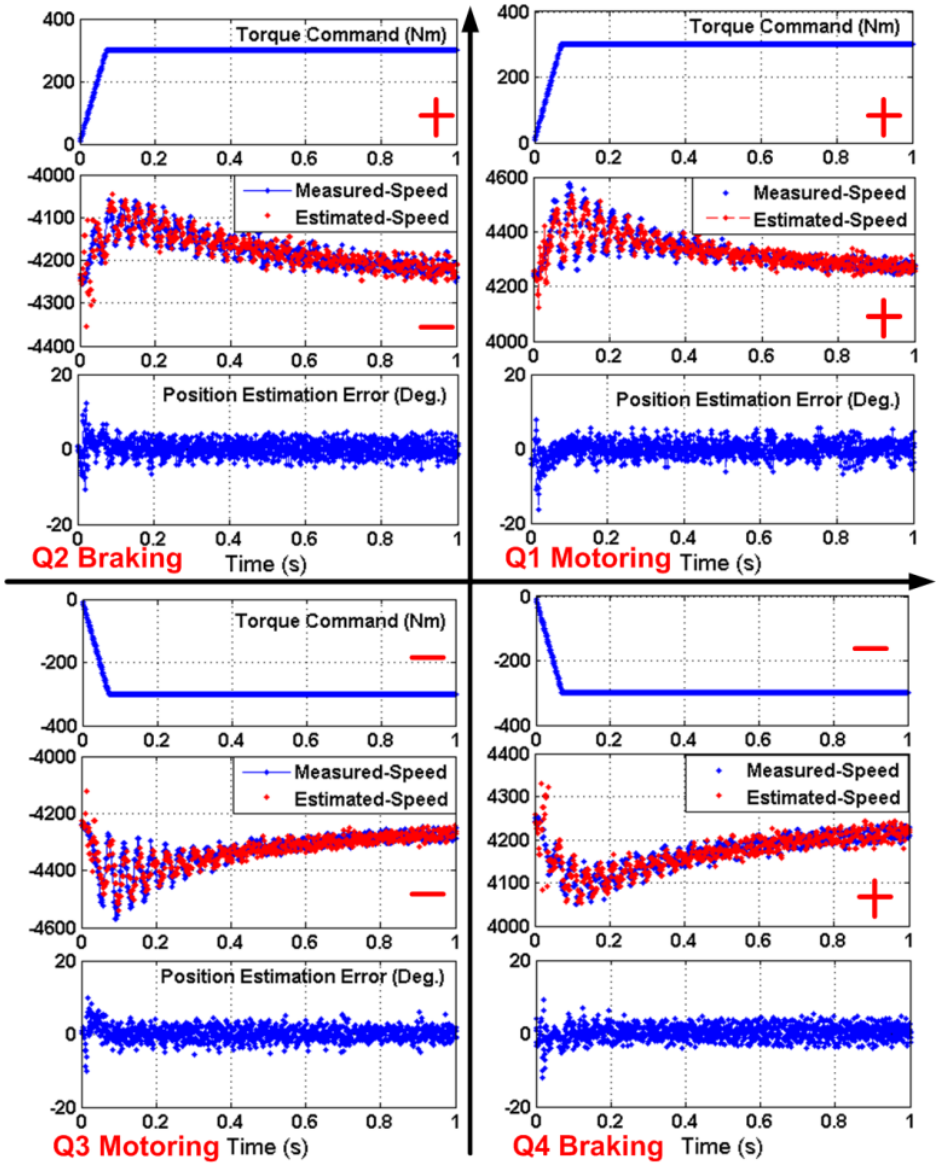

Figure 7.10: Performance of the sensorless drive under four-quadrant operations.

Figure 7.11 shows the testing results for two cases of complete torque reversal, i.e., (a) from full motoring to full braking and (b) from full braking to full motoring, where the slew rate of the torque changes was 4000 Nm/s. Because of the sudden change in the torque command, the shaft speed increased/dropped 450 RPM in both cases. However, the position and speed estimations exhibited good ride-through performance

under complete torque reversals. Although the position estimation had a relatively large maximum error of 10 electric degrees in the transient, the estimated position converged towards the measured position quickly.

The DC-bus voltage in full motoring to full braking transition is shown in Figure 7.12. From 1.95 s to 2.1 s, the commanded torque increased from −300 Nm to 300 Nm. Prior to 1.95 s, the DC bus voltage was around 700 V, and then increased because electric power was fed back to the DC bus when the IPMSM was in the braking mode. When the DC bus voltage reached 750 V, the DC chopper turned on and the DC voltage began to drop. The DC chopper turned off when the DC bus voltage was below 725 V. This explained why the DC bus voltage increased and decreased back and forth several times during the torque reversal. When the torque reached steady state, the DC-bus voltage will dropped to 700 V again.

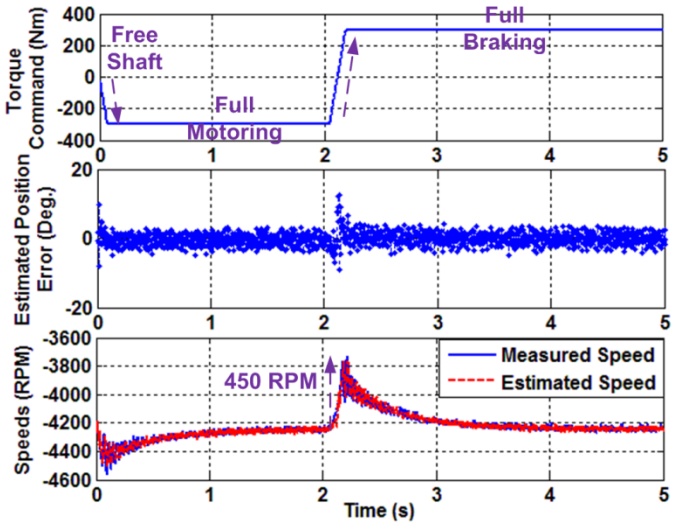

(a)

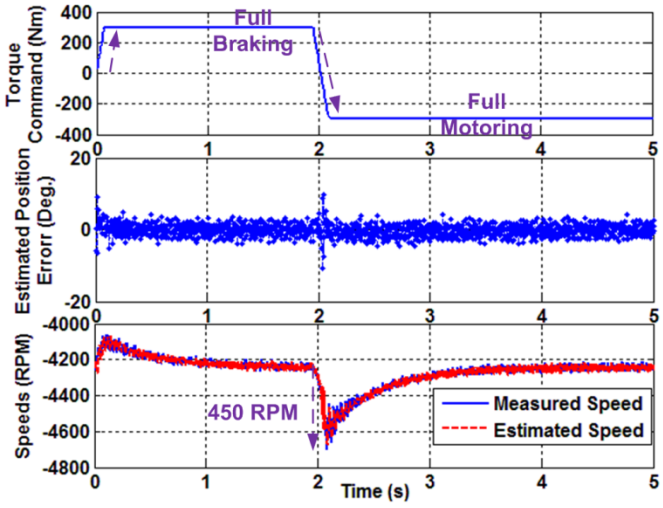

(b)

Figure 7.11: Performance of the sensorless drive under complete torque reversals: (a) from full motoring to full braking and (b) from full braking to full motoring.

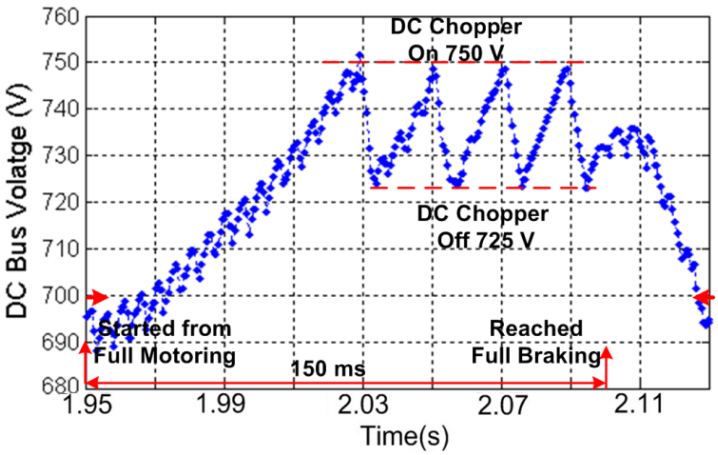

Figure 7.12: DC-bus voltage in the case of full motoring to full braking transition.

7.2.5 System Performance Using Conventional DSMO

As a comparison, similar experiments, i.e., torque ramp change and complete torque reversal, were performed for the sensorless drive system using a conventional DSMO without the proposed parameter adaption scheme shown in Figure 3.5. The torque

command profiles and the resultant position estimation errors of the system for the torque ramp change and complete torque reversal tests under base speed are shown in Figure 7.13(a) and (b), respectively. In the torque ramp change test, the torque command was increased linearly from 0 Nm to 120 Nm with a constant slew rate of 4000 Nm/s. The parameters of the DSMO were tuned to guarantee a zero phase lag between the estimated and measured positions at the zero-torque condition. As shown in Figure 7.13(a), the position estimation error had large oscillations during the torque transient stage, and phase lags are obvious. Although the position estimation error settled down after the torque command reached the new steady-state value, there was an obvious phase lag around 10 electric degrees between the estimated and measured positions. In this case, due to the saliency of the IPMSM, without proper observer parameter adaption, a phase difference was present between the estimated and measured positions. If the torque was ramp changed to a higher value, e.g., 200 Nm, the system lost stability due to a large phase lag.

In the complete torque reversal test, the torque command was reduced linearly from 300 Nm to −300 Nm with a constant slew rate of 4000 Nm/s. The parameters of the DSMO were tuned to guarantee a zero phase lag between the estimated and measured positions when the torque was 300 Nm. The measured rotor position was first used in the drive system, i.e., a sensor-based drive system, to increase the output torque of the IPMSM to 300 Nm. Then, when the estimated rotor position was aligned with the measured rotor position, the drive system was switched to closed-loop sensorless control. With fixed observer parameters, the sensorless drive system was able to produce 300 Nm torque at steady state. However, when the torque reversal occurred, instability was

observed. The position estimation error diverged quickly, which triggered an over current fault on the test stand.

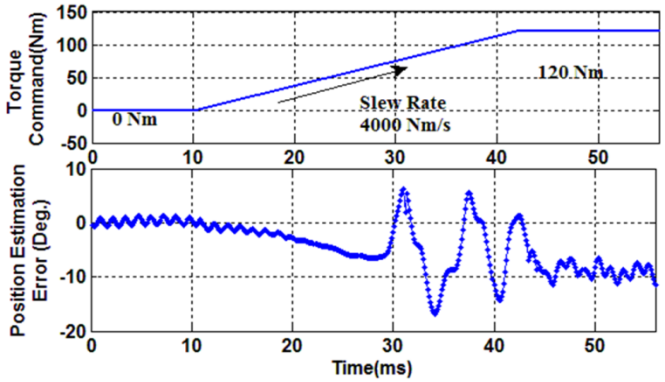

(a)

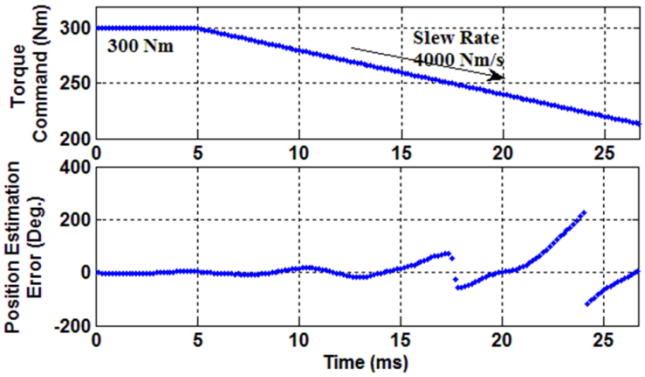

(b)

Figure 7.13: Performance of conventional DSMO-based sensorless drive under (a) torque ramp change and (b) complete torque reversal.

7.3 Simulation Studies for Improved Position/Speed Estimator

7.3.1 Simulation Results of the MRAS-Based Rotor Speed Estimator

Real-world vehicle data was used for simulation studies to verify the performance of the proposed MRAS-based rotor speed estimator. The data were logged from an

IPMSM operating as a generator on an off-road test vehicle. Figure 7.14 depicts the torque and speed of the IPMSM and the DC bus voltage of the vehicle during one typical driving cycle. In the simulation, the IPMSM was operated in the torque control mode using the profile shown in Figure 7.14 as the torque command. When the torque had a higher slew rate change, e.g., around 104 s, an obvious abrupt speed dip was observed correspondingly, which is a critical period for performance evaluation of the proposed rotor speed estimator.

The corresponding simulation results of the rotor speed are shown in Figure 7.15, including the speed command, the estimated speed obtained from the estimated rotor position using a MA filter, and the speeds obtained from the proposed MRAS speed estimator in both operating modes. During the large speed transient around the 104^{th} second, the speeds estimated by the MA and the proposed MRAS in Mode I could track the desired value. However, both of the estimated speeds had obvious delays and relatively large estimation errors caused by the large load transition, where the maximum speed estimation error of MA reached 150 RPM, i.e., 3% when using 5000 RPM as the base. Compared to the MA and the MRAS in Mode I, the delay in the speed estimation was negligible; and the magnitude of the speed estimation error obtained from the MRAS in Mode II with respect to the speed command was always smaller, i.e., less than 1%.

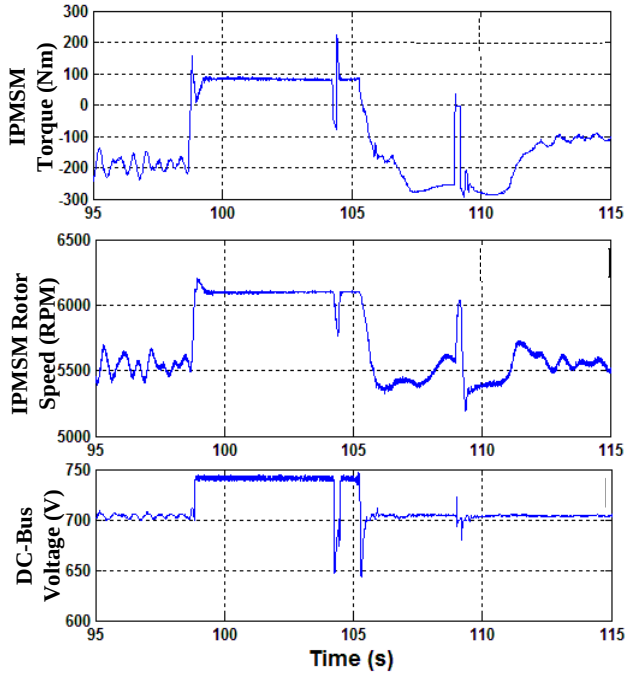

Figure 7.14: Real-world vehicle data profiles used for simulation studies.

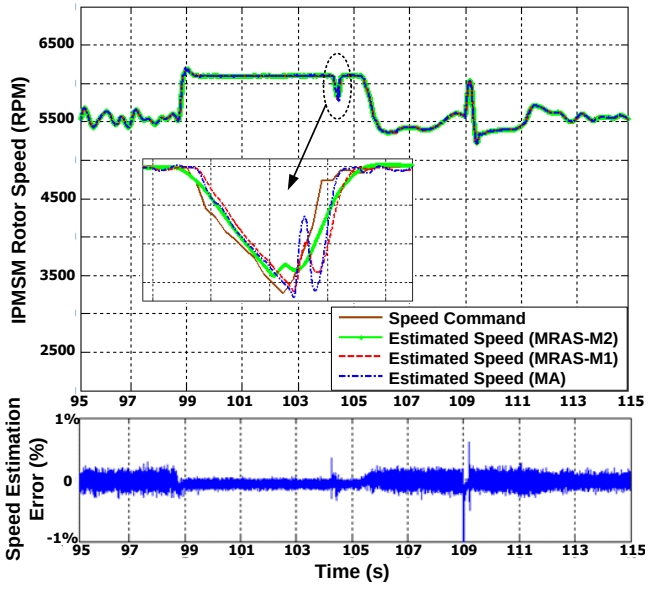

Figure 7.15: Speed estimation results using the proposed speed estimator and an MA filter.

7.3.2 Simulation Results of Oscillation Mitigation Scheme

Simulation studies were performed to compare the performance of the proposed rotor position estimator with and without the estimated speed feedback-based oscillation mitigation scheme, and the steady-state results are shown in Figures 7.16 and 7.17, respectively. In the simulation, the rotor speed was 3000 RPM; and the corresponding fundamental frequency of the EEMF was 200 Hz. The weight λ in Equation (4.15) was selected to be 0.1. Due to the noise content in the estimated EEMF, the estimated position had many oscillations; and the position estimation error was relatively large, within ±10 electric degrees, as shown in Figure 7.16(c). As Figure 7.17(a) shows, the estimated EEMF was exactly the same as that in Figure 7.16(a), since the oscillation mitigation algorithm only modified the estimated position but had no effect on the EEMF estimated by the SMO. As shown in Figure 7.15, the speed estimation error was always smaller than 1%; namely, the speed estimation error was limited to within ± 30 RPM when the rotor speed was 3000 RPM. Using the maximum speed estimation error of 1% of the operating speed, i.e., 30 RPM, in this simulation study, for one sampling period, the position estimation error caused by the speed estimation error was only 0.12 electric degrees, which is so small such that it had little effect on the position estimation. As shown in Figure 7.17, by using the proposed rotor position estimation algorithm, the estimated and measured rotor positions were on top of each other. The position estimation error was almost limited within ±3 electric degrees. The position oscillation problem was significantly mitigated at steady state, when compared to the position estimator without the proposed oscillation mitigation scheme.

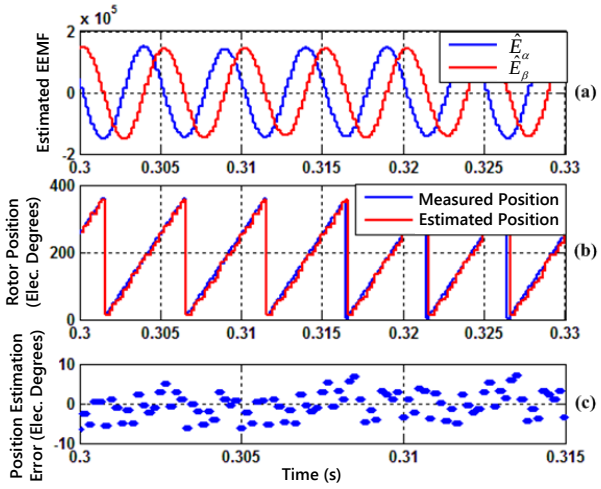

Figure 7.16: Simulation results for the proposed position estimator without the oscillation mitigation scheme; (a) estimated EEMF components; (b) measured and estimated positions; and (c) position estimation error.

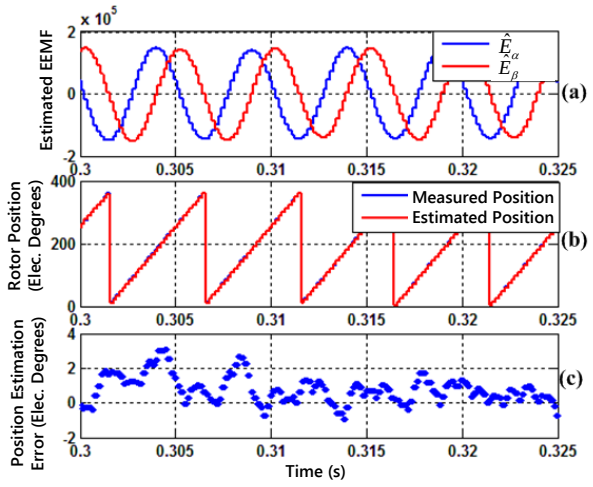

Figure 7.17: Simulation results for the proposed position estimator with the oscillation mitigation scheme (when λ=0.1); (a) estimated EEMF components; (b) measured and estimated positions; and (c) position estimation error.

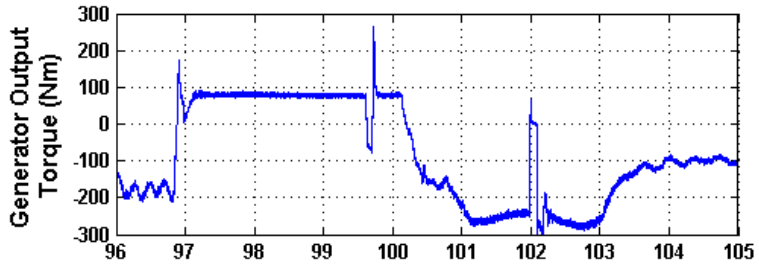

(a)

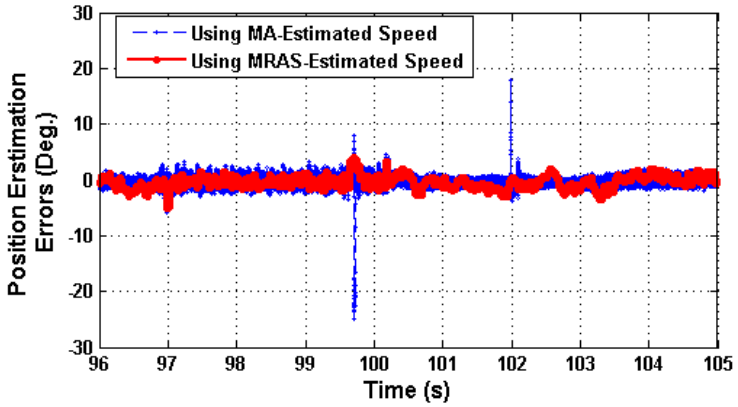

(b)

Figure 7.18: Comparison of simulation results of methods presented in the Chapter 4 and in [111]: (a) output torque profile of the IPMSM; and (b) position estimation errors.

The transient performance of the proposed oscillation mitigation scheme was also evaluated by using the real-world vehicle data shown in Figure 7.14. Figure 7.18 compares the rotor position estimation errors obtained from the methods presented in Chapter 4 and in [111]. In Chapter 4, the rotor speed was estimated by using the proposed MRAS-based speed estimator. While in [111], the rotor speed was estimated from the estimated rotor position using an MA filter. As shown in Figure 7.18(b), when the generator torque was constant or had a slow slew rate variation, the two methods had almost identical oscillation mitigation performance. However, when the generator torque had abrupt changes, e.g., around 99.7 s and 102 s, due to the delay in the estimated speed

caused by the MA filter, large position estimation errors (>20 electric degrees) were observed when using the method presented in [111]. On the contrary, the abrupt torque changes had no effect on the position estimation error when the method presented in Chapter 4 was used.

7.4 Experimental Results for Improved Position/Speed Estimator

7.4.1 Performance Evaluation for the Proposed Rotor Speed Estimator

Complete torque reversals were used to mimic a large load transient in Figure 7.14. The performance of the conventional MRAS and the proposed MRAS in Mode II in the complete torque reversal tests is compared in Figure 7.19. Because of the fast torque reversals, the rotor speed experienced sudden changes, e.g., around a 500 RPM drop in Figure 7.19(a) and (b) and 500 RPM increase in Figure 7.19(c) and (d). Both the conventional MRAS and the proposed MRAS in Mode II can track the speed changes. However, the speed estimated from the conventional MRAS had an unwanted large oscillation, as highlighted in the dashed-line circles in Figure 7.19(a) and (c). On the other hand, no obvious unwanted oscillation was observed in the speed estimated from the MRAS in Mode II. Using 5000 RPM as the speed base, the speed estimation error of the MRAS in Mode II was always smaller than 1% in steady state and during large load transient; while the speed estimation error was nearly 2% during large load transient when using conventional MRAS.

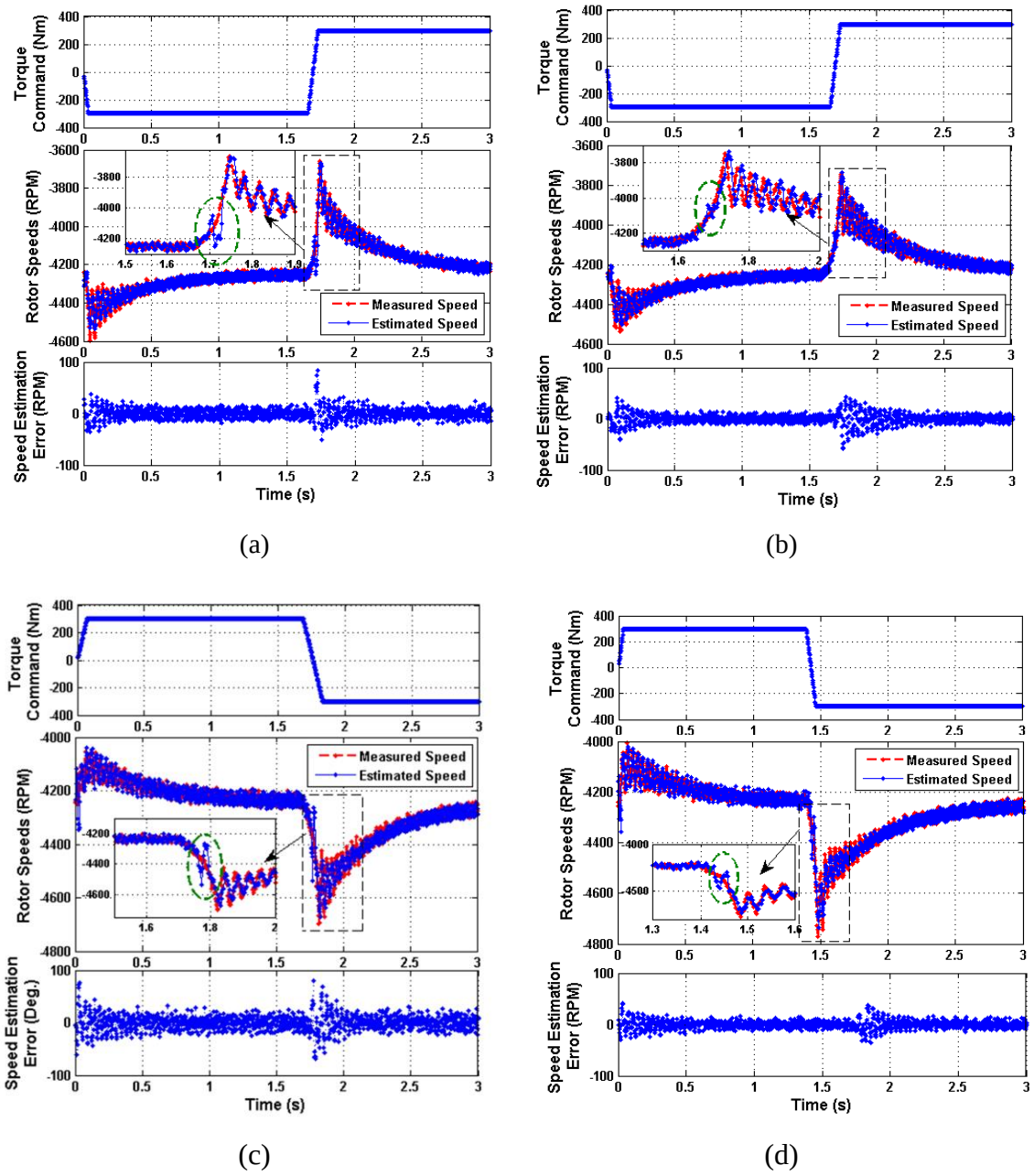

Figure 7.19: Experimental results during complete torque reversals: (a) from full motoring to full braking using conventional MRAS; (b) from full motoring to full braking using the experimental MRAS in Mode II; (c) from full braking to full motoring using the conventional MRAS; and (d) from full braking to full motoring using the experimental MRAS in Mode II.

7.4.2 Performance Evaluation for the Proposed Position Estimator with Oscillation Mitigation Scheme

Figure 7.20 compares the position estimation errors obtained from the experimental rotor position estimator with and without the oscillation mitigation scheme using different weights λ. In all of the tests, the rotor speed was 3000 RPM; and the sampling frequency of the current measurements was 6 kHz. The effect of the rotor speed feedback on the rotor position estimation reduced with the increase of λ. When λ was larger than 0.8, the speed feedback had little effect on the estimated position. Even when λ decreased to 0.5, the position filtering effect was not obvious. However, when λ further decreased to 0.3 and 0.1, the magnitude of oscillation of the position estimation error reduced significantly; and the variance of the oscillation was closer to zero. As Figure 7.20(a) shows, when λ = 0.1, the position estimation error was limited within ±2 electric degrees, which agrees with the simulation result presented in Figure 7.17.

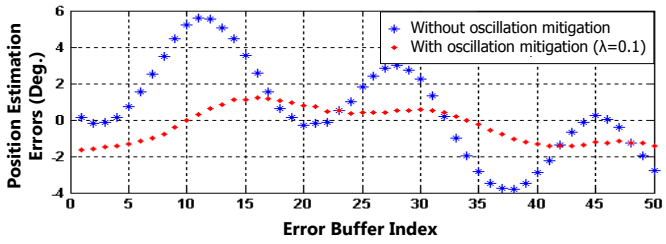

(a)

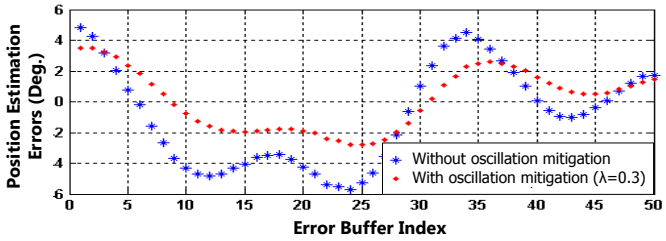

(b)

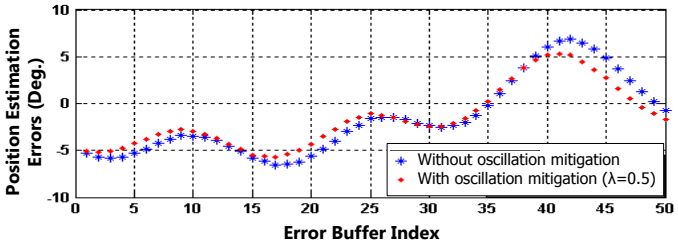

(c)

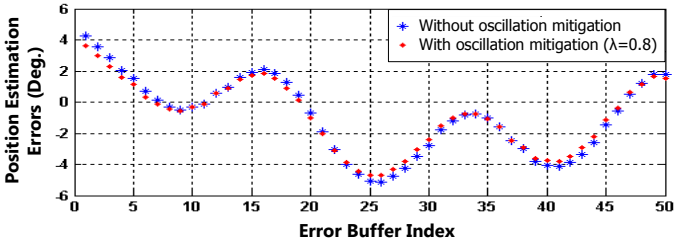

(d)

Figure 7.20: Comparison of position estimation errors obtained from the proposed rotor position estimator with and without the oscillation mitigation scheme using different weights λ. (a) λ = 0.1; (b) λ = 0.3; (c) λ = 0.5; and (d) λ = 0.8.

Figure 7.21 shows the experimental results obtained when using the proposed position estimator without the oscillation mitigation scheme, where the rotor speed was 1500 RPM. The curves of the measured and estimated rotor positions were on top of each other. However, it was still obvious that the estimated position had small oscillations. As a comparison, the estimated rotor position obtained from the proposed position estimator with the oscillation mitigation scheme is shown in Figure 7.22, where λ = 0.1. It can be seen that the oscillation in the estimated rotor position had been effectively mitigated.

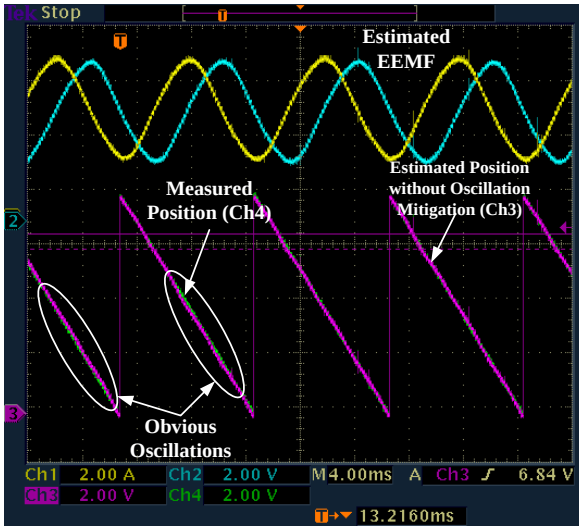

Figure 7.21: Experimental results when using the proposed rotor position estimator without the oscillation mitigation scheme, where the rotor speed was 1500 RPM.

Figure 7.22: Comparison of the measured and estimated rotor positions for $\lambda = 0.1$ when the rotor speed was 1500 RPM.

The transient performance of the rotor position estimation methods proposed in Chapter 4 and in [111] during complete torque reversals is compared in Figures 7.23 and 7.24. When the torque command had fast slew rate changes during the complete torque reversals, the position estimation error of the method presented in [111] had large spikes,

whose amplitudes exceeded 20 electric degrees. As a comparison, the spikes in the position estimation error during the fast torque transient were significantly mitigated by using the method proposed in Chapter 4. The results presented in Figures 7.23 and 7.24 are coincident with the simulation results presented in Figure 7.18.

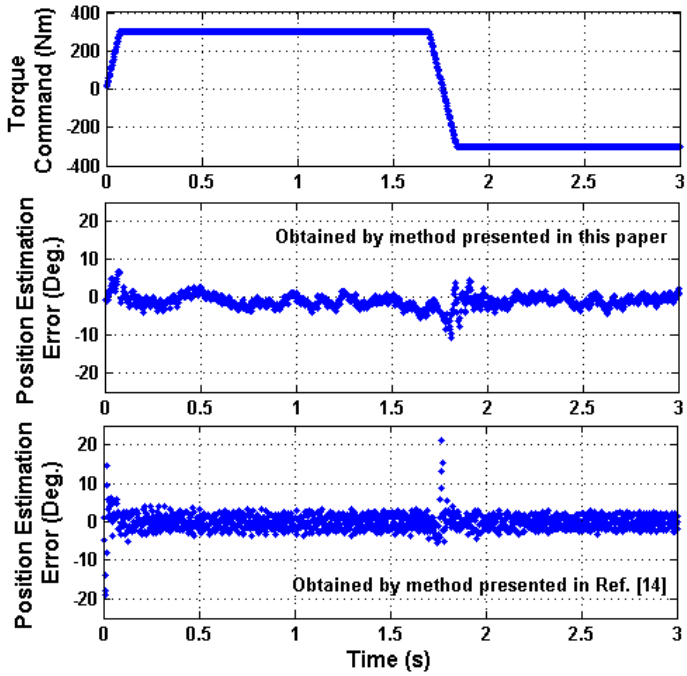

Figure 7.23: A comparison of transient performance of the methods proposed in Chapter 4 and in [111] under a complete torque reversal from full braking to full motoring.

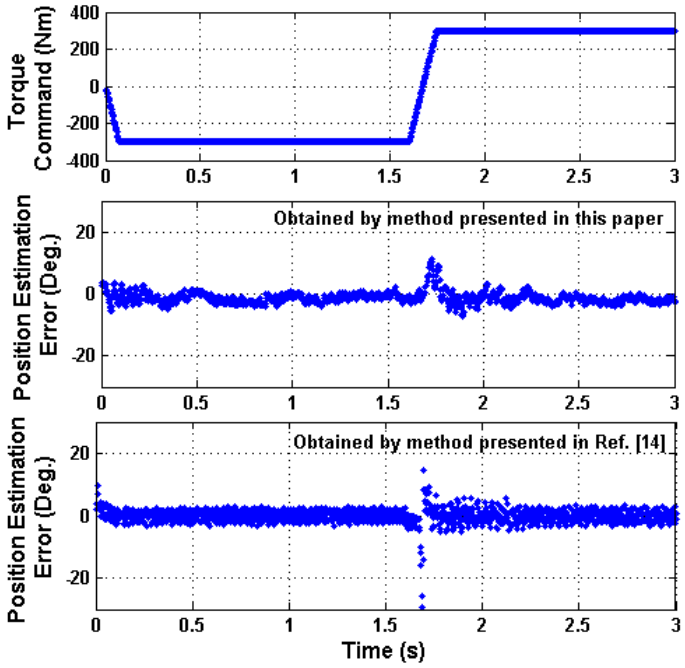

Figure 7.24: A comparison of transient performance of the methods proposed in Chapter 4 and in [111] under a complete torque reversal from full motoring to full braking.

7.5 Simulation Studies for Sensorless PMSM Drive using Extended Flux-Based QSMO

Figure 7.25 compares the performance of the three estimators when the salient-pole PMSM operated at the rated speed with different load variations. The commanded torque (T^*) and generated torque (T_{em}) of the PMSM using the proposed rotor position estimator are shown in Figure 7.25(a), where the torque has slow slew rate changes, step changes, and complete reversals under both slow slew rate changes and step changes. The output torque of the sensorless drive system could well track the torque command during the whole test. The rotor position estimation errors obtained from the three estimators are compared in Figure 7.25(b). The three rotor position error curves are on top of each other during slow slew rate torque changes. Under this circumstance, the variation of the

extended flux was quite small and could be ignored. Therefore, the three rotor position estimators had similar performance. However, when the torque had step changes, the rotor position error was significantly reduced by using the proposed estimator; and the performance of the proposed estimator without the dynamic position compensator was still better than the EEMF-based rotor position estimator. The response of φ is shown in Figure 7.25(c). It clearly shows when the torque changed with slow slew rates, φ was almost zero; however, when the torque experienced a step change, φ was a large value and could not be ignored.

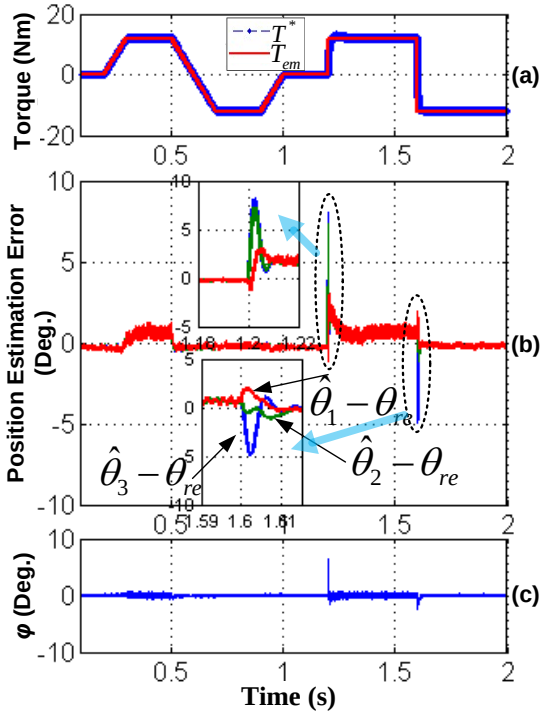

Figure 7.25: Comparison of the three rotor position estimators when the salient-pole PMSM operated at the rated speed with different torque variations.

Figure 7.26 compares the responses of the three estimators when the salient-pole PMSM operated at 20% of the rated speed, i.e., 250 RPM, with the same torque variations as in Figure 7.25. The transient performance of the proposed estimator was much better than the other two estimators. Figure 7.27(a) shows the performance of the proposed estimator when the salient-pole PMSM operated at 1% of the rated speed, i.e., 12.5 RPM, during a torque step change from zero to the rated value. Both the EEMF-based rotor position estimator and the proposed estimator without the position compensator failed in this case. However, the proposed estimator still worked; and the accuracy of the rotor position estimation was still acceptable, as shown in Figure 7.27(b) and (c).

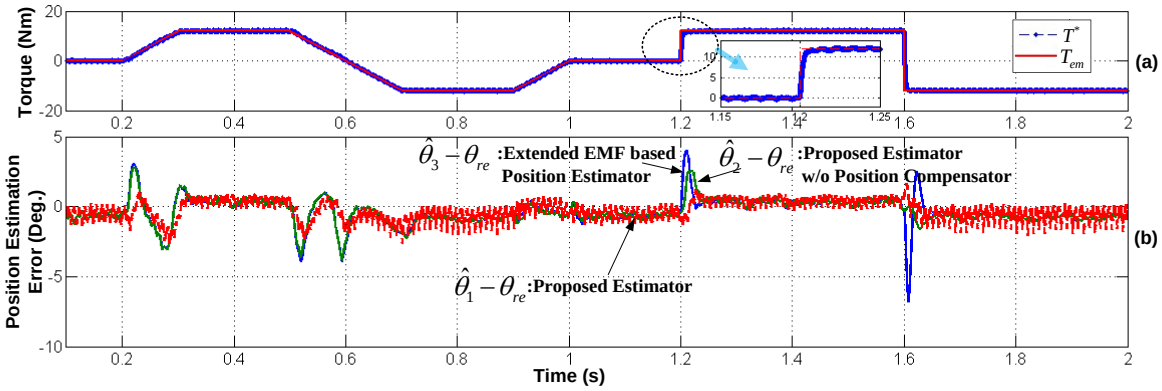

Figure 7.26: Comparison of the three rotor position estimators when the salient-pole PMSM operated at 20% rated speed with different torque variations.

The rotor speed response under the no load condition of the sensorless drive equipped with the proposed rotor position estimator is shown in Figure 7.28. The profiles of the commanded speed (Spd_{cmd}), measured speed (Spd_{mea}), and estimated speed (Spd_{est}) are compared in Figure 7.28(a). The PMSM rotor speed increased from 5% of the rated

value, i.e., 62.5 RPM, to the rated value within 0.5 s, stayed at the rated value for 0.6 s, and then decreased back to 62.5 RPM within 0.4 s. The sensorless control system showed good speed tracking performance during the speed variations. The corresponding rotor position estimation error, as shown in Figure 7.28(b), was within ±4 electric degrees except for a spike at the beginning of the speed ramp-up, which, however, settled down shortly.

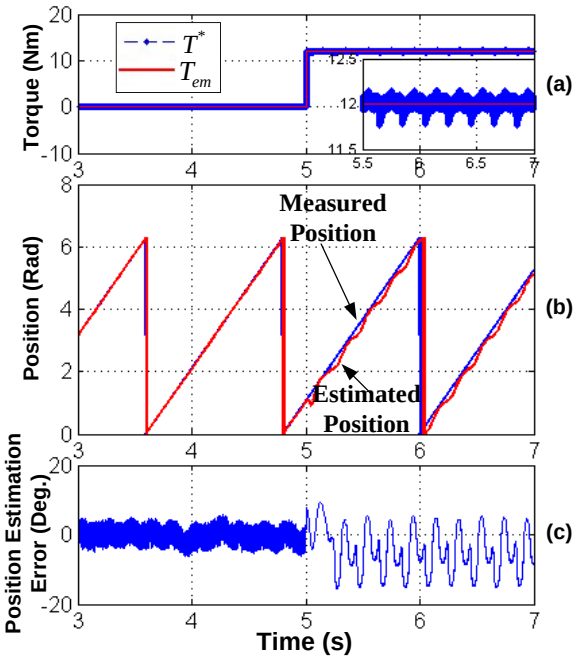

Figure 7.27: Performance of the proposed rotor position estimator when the salient-pole PMSM operated at 1% rated speed under a step torque change.

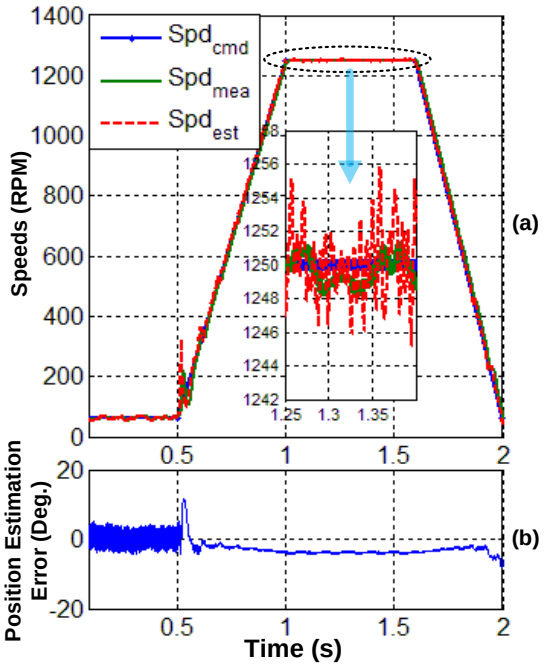

Figure 7.28: Speed tracking performance of the sensorless drive using the proposed rotor position estimator.

7.6 Experimental Results for Sensorless PMSM Drive Using Extended Flux-Based QSMO

The performances of the EEMF-based and extended flux-based estimators are compared under the same speed ramp change tests, where the salient-pole PMSM was operated in the speed control mode as a motor; and the rotor speed decreased from 1500 RPM to 500 RPM in 200 ms. The corresponding experimental results are shown in Figure 7.29. In the steady states, when the speed command was fixed at either 1500 RPM or 500 RPM, the rotor position estimation performances of the two estimators were identical. However, during the speed transients, the error between the measured rotor position and the rotor position obtained from the proposed estimator was much smaller than that obtained from the EEMF-based position estimator. These results verified that the transient performance of the proposed estimator was better than that of the EEMF-based position estimator. The results of the proposed estimator under a speed ramp-up test, where the PMSM rotor speed increased from 500 RPM to 1500 RPM in 200 ms, is shown in Figure 7.30. Again, the transient performance of the proposed estimator was almost the same as that in the steady state in terms of the position estimation error. These results show that the proposed rotor position estimator is robust to rotor speed variations of the PMSM.

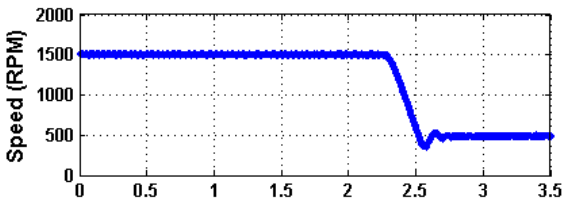

(a)

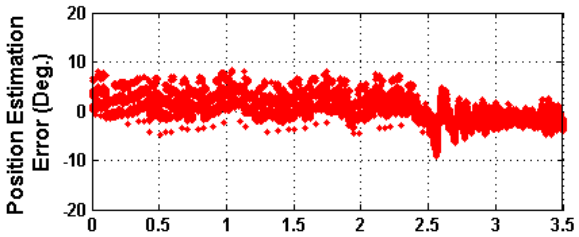

(b)

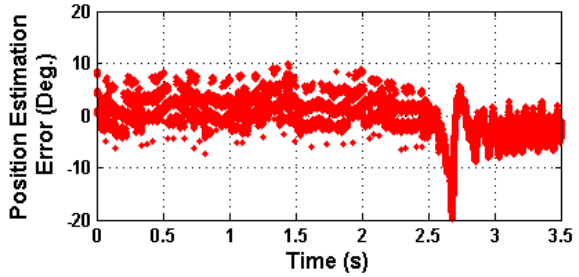

(c)

Figure 7.29: Results for speed ramp down test: (a) rotor speed profile and error between the measured rotor position and the rotor position obtained from (b) the proposed estimator and (c) the EEMF-based estimator.

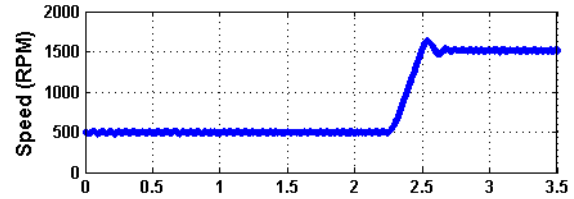

(a)

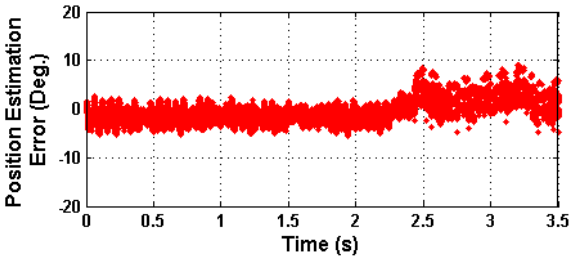

(b)

Figure 7.30: Results for speed ramp-up test: (a) rotor speed profile and (b) estimation error between the estimated (from proposed estimator) and measured positions.

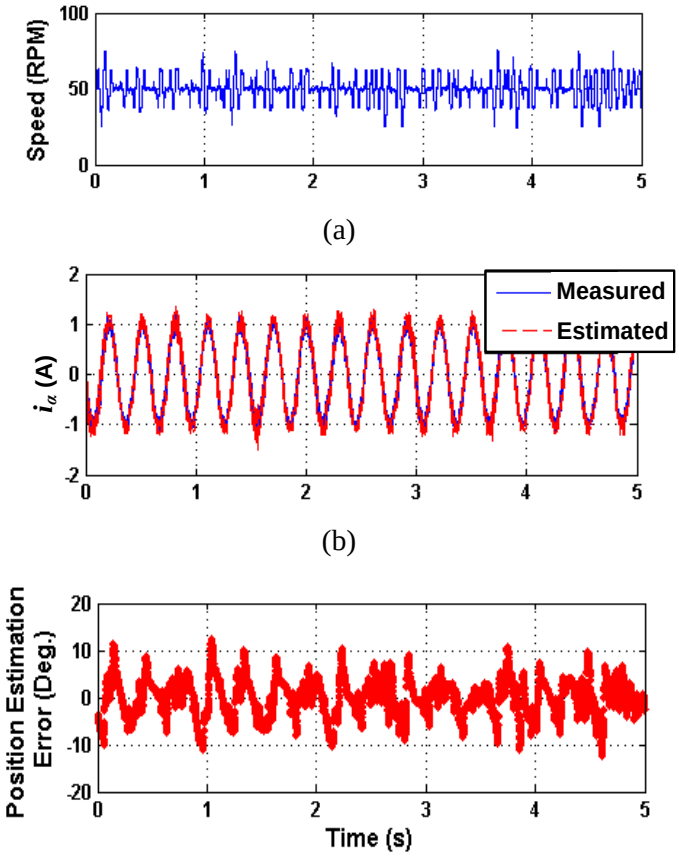

Figure 7.31: Results at 50 RPM (1.67% of the rated speed): (a) rotor speed profile, (b) estimated and measured values of the α-axis stator current, and (c) error between the estimated (from the proposed estimator) and measured rotor positions.

To verify the low speed operation capability of the sensorless drive using the proposed estimator, the system was tested in the low speed condition, e.g., 50 RPM (1.67% of the rated speed). The corresponding experimental results are presented in Figure 7.31. At 50 RPM, the rotor speed had relatively larger ripples compared to that at 500 RPM and 1500 RPM. However, the average value of the rotor speed was maintained at 50 RPM. Under this circumstance, the estimated value of the α-axis PMSM stator current (i_α) tracks the measured value well, illustrated in Figure 7.31(b). The position

estimation error was limited within an acceptable range to maintain a stable speed control. While using the EEMF-based estimator, the speed control failed at such a low speed level due to the low SNR.

The results of the sensorless torque control of the PMSM using the proposed rotor position estimator are presented in Figure 7.32. In this test, the DC motor ran as a prime mover machine, which regulated the shaft speed of the system. The salient-pole PMSM worked as a generator in the torque control mode. There were three key points in this test, including (1) the dSPACE system switched from the edit mode to the animation mode, (2) the DC drive was enabled, and (3) the period of the PMSM torque changed at a constant speed. Before the DC drive was enabled, the DC motor and the PMSM were in the stall condition. There was a constant error between the estimated and measured rotor positions. Once the DC drive was enabled, with the information of the PMSM terminal voltages and phase currents, the estimated rotor position quickly converged to the measured value even in the low speed range. After that, the rotor position estimation error was always maintained within a constant range, of ±6 electric degrees, even during the torque transition, where the torque increased from zero to the rated value and then decreased back to zero. No torque-dependent offset was observed in the position estimation error. These results showed that the proposed position estimator was robust to torque variations of the PMSM.

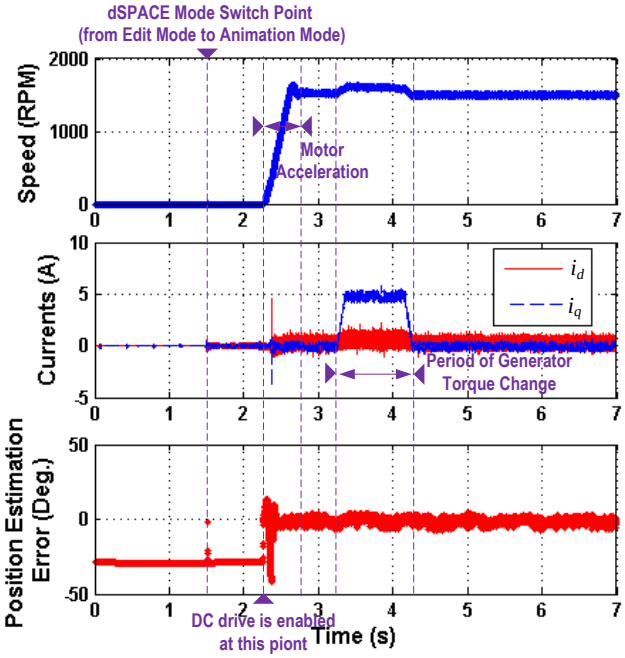

Figure 7.32: Results of the sensorless torque control of the PMSM using the proposed rotor position estimator.

7.7 Simulation Studies for Sensorless SPMSM Drive in Low-Speed Operation

The simulation results of the SPMSM sensorless drive system under different torque conditions, when the fundamental electrical rotating frequency of the SPMSM, f_e (= $\omega_{re}/2\pi$), was 1 Hz, are shown in Figure 7.33. In the simulation, the PWM switching frequency and current sampling frequency were 3 kHz. The frequency of the injected square-wave voltage signal was 1 kHz. Figure 7.33 shows the responses of $i_{\alpha\beta}$, $i_{\alpha,h}$, and $i_{\beta,h}$, the estimated and measured rotor positions, and the position estimation error for each torque condition. At 1 Hz and under different torque conditions, the position estimation error always oscillated around 0°; and no phase shift was observed. The position

estimation error was limited within an acceptable range, and the torque (or current) was well regulated by the sensorless drive system.

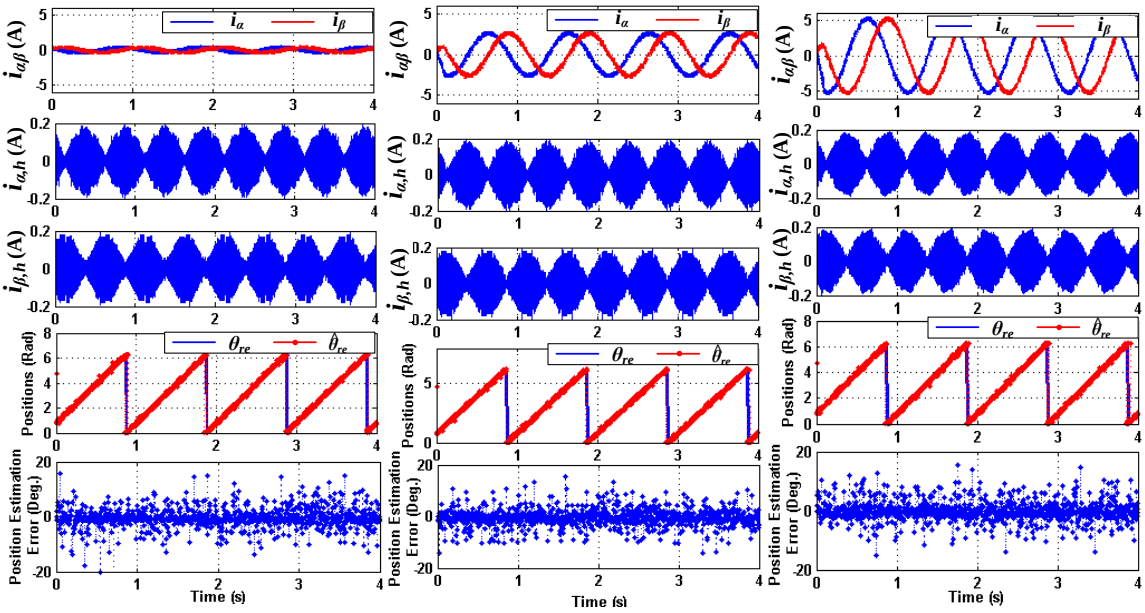

(a) (b) (c)

Figure 7.33: Simulation results of the sensorless SPMSM drive system, when the fundamental electrical frequency of currents is 1 Hz: (a) zero torque; (b) 50% of rated torque; and (c) rated torque.

To verify a wide speed control bandwidth of the proposed rotor position estimator and sensorless drive system, results for the speed control from f_e = 1 Hz (15 RPM) to f_e = 53.3 Hz (800 RPM) are shown in Figures 7.34 and 7.35. To guarantee good speed tracking performance in the medium speed range, e.g., 5-64% of the base speed) as well, the PWM switching frequency and the injected signal frequency were increased to 4 kHz and 2 kHz, respectively. As shown in Figure 7.34, in the speed control mode, the actual rotor speed tracked the reference speed well from 15 RPM to 800 RPM. Figure 7.35 depicts the profiles of $i_{\alpha,h}$ and $i_{\beta,h}$ and their position-dependent envelopes at 800 RPM.

These results indicated that the proposed method was effective up to 800 RPM, which is 64% of the base speed. At this speed, the back EMF-based position estimator is also effective. Therefore, it was convenient to transit from the proposed method used in the low-speed range to the back EMF-based method used in the medium- and high-speed ranges.

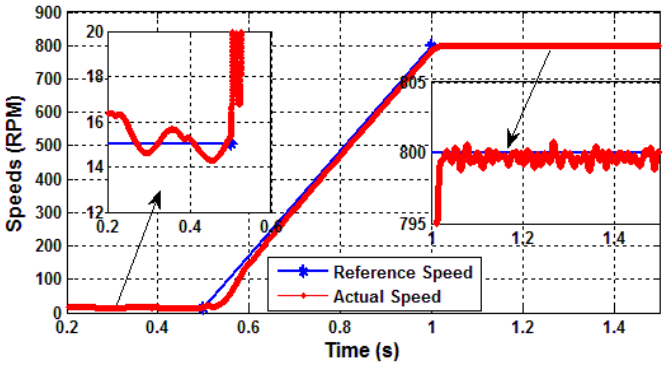

Figure 7.34: Simulation result of sensorless speed control in the low- and medium-speed ranges.

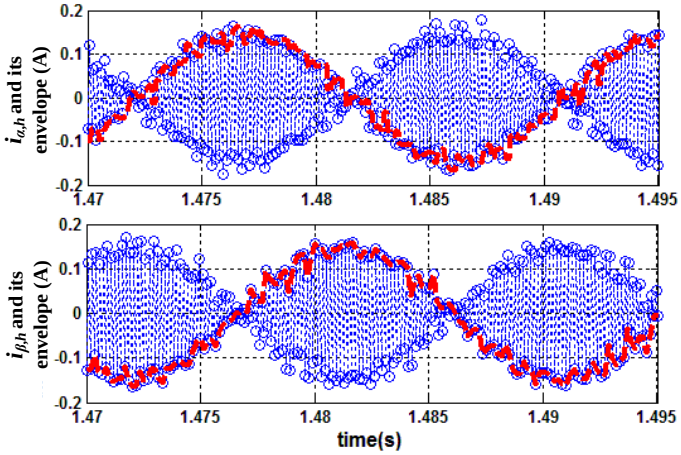

Figure 7.35: Profiles of $i_{\alpha,h}$ and $i_{\beta,h}$ and their envelopes at 800 RPM (f_e = 53.3 Hz).

7.8 Experimental Results for Sensorless SPMSM Drive in Low-Speed Operation

When the test SPMSM worked as a motor, the shaft speed was regulated. Since the rotating speed was proportional to the value of v_q, by using different v^*_q, different rotating speeds can be achieved. At the same time, a 200 Hz square-wave voltage vector was used as v^*_d, whose magnitude is 0.5 V. The PWM switching frequency was 2 kHz. Experimental results for the sensorless speed control are shown in Figure 7.36 for different speed conditions. In each case, the speed was almost constant; and the measured f_e, $i_{\alpha,h}$ and its envelope and the position estimation error are plotted.

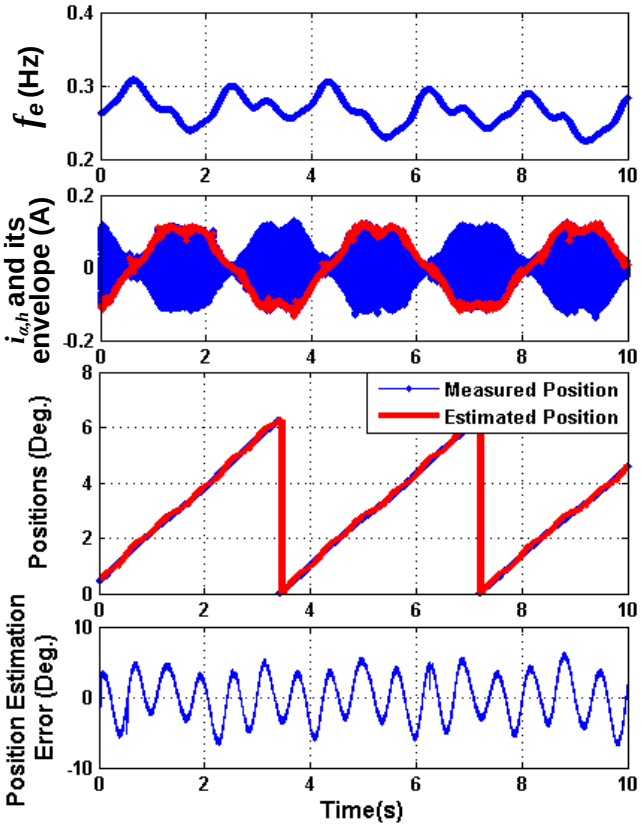

(a)

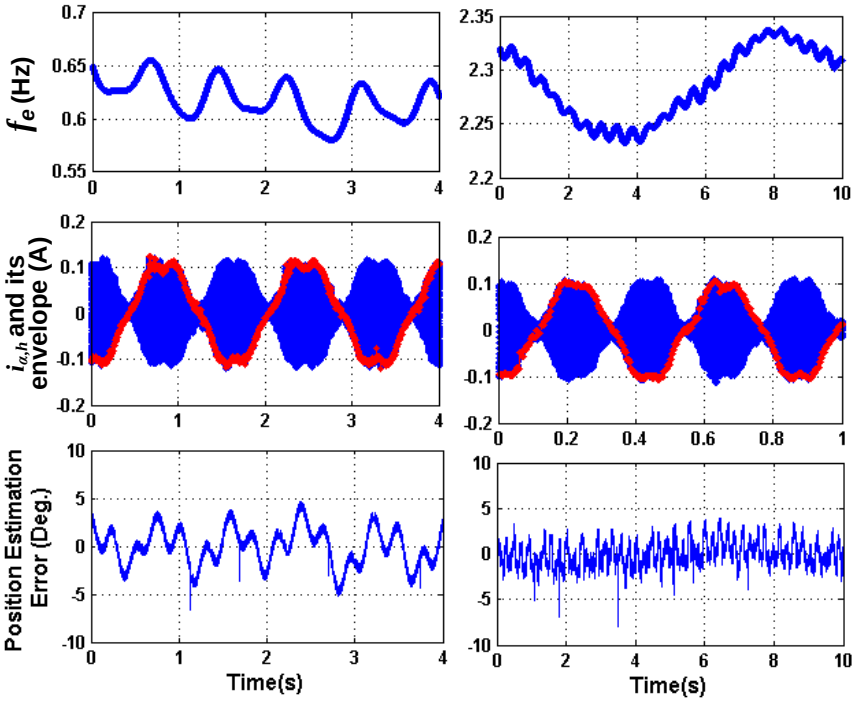
f_e (Hz)
$i_{a,h}$ and its envelope (A)
Position Estimation Error (Deg.)
Time(s)
Time(s)

(b) (c)

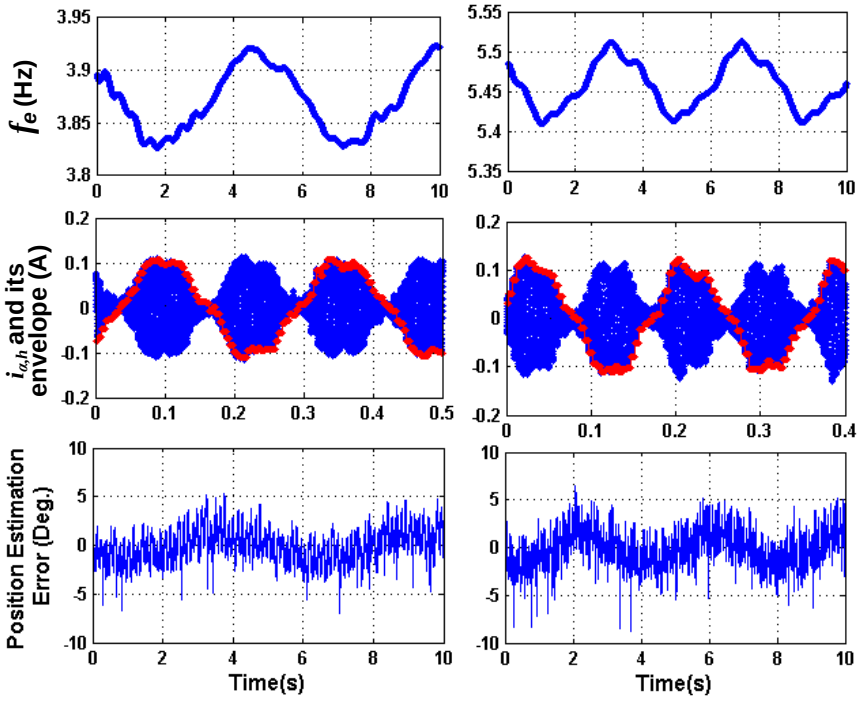
f_e (Hz)
$i_{a,h}$ and its envelope (A)
Position Estimation Error (Deg.)
Time(s)
Time(s)

(d) (e)

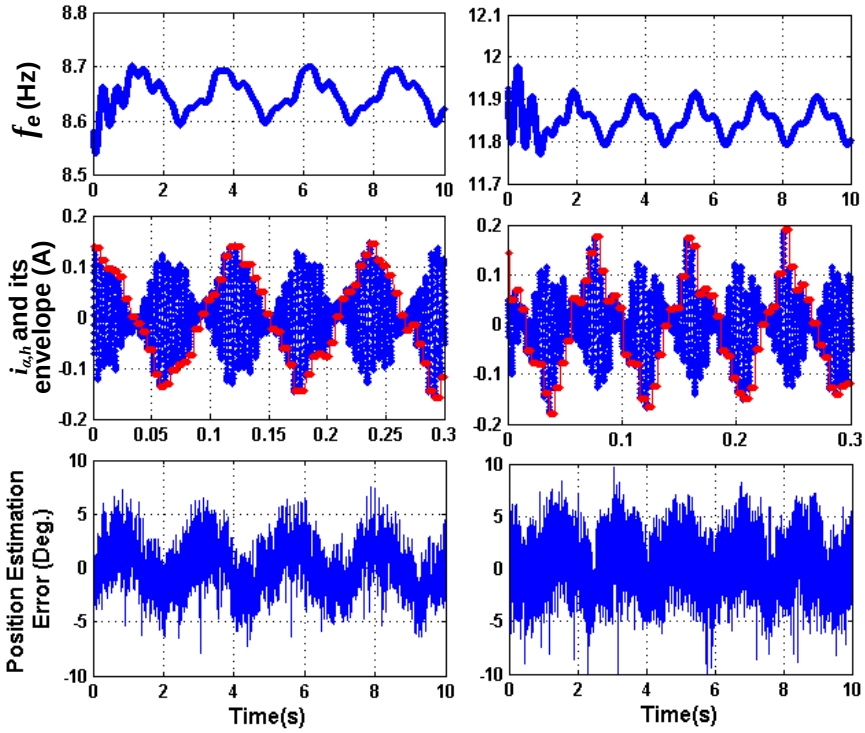

(f) (g)

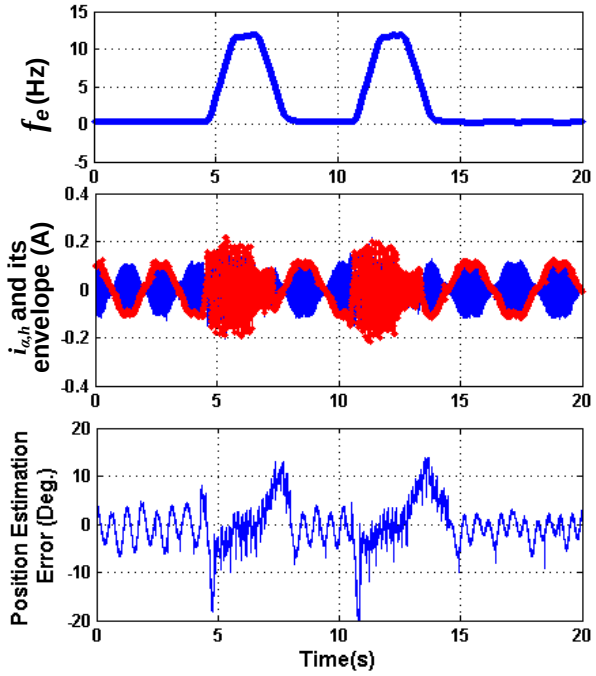

(h)

Figure 7.36: Experimental results of the sensorless speed control for the test SPMSM: (a) v_q = 2 V and f_e = 0.28 Hz; (b) v_q = 2.5 V and f_e = 0.6 Hz; (c) v_q = 5 V and f_e = 2.3 Hz; (d) v_q = 7.5 V and

f_e = 3.87 Hz; (e) v_q = 10 V and f_e = 5.45 Hz; (f) v_q = 15 V and f_e = 8.65 Hz; (g) v_q = 20 V and f_e = 11.85 Hz; and (h) ramp speed test.

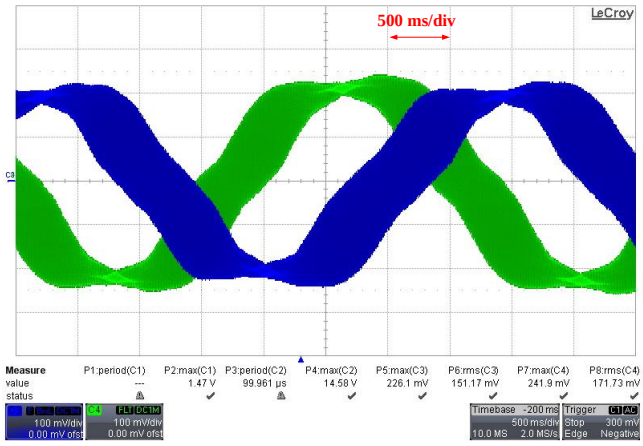

Figure 7.37: Phase current (i_a and i_b) waveforms in the case of Fig. 10(a).

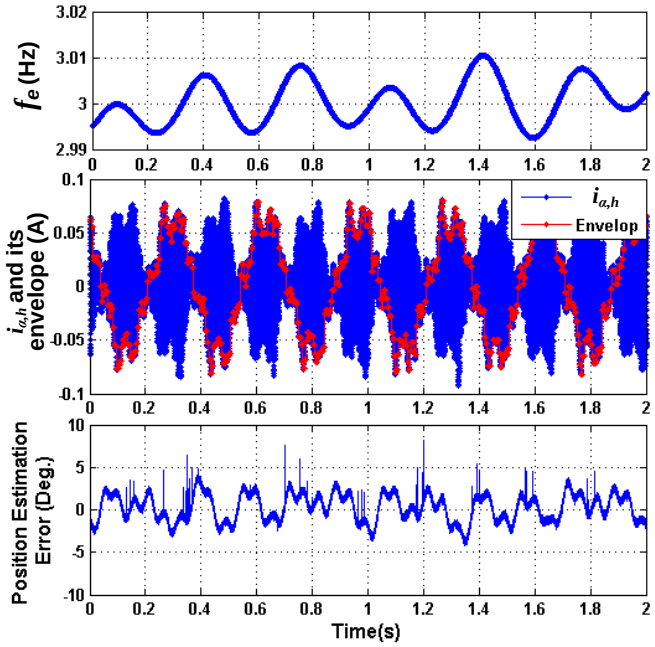

Figure 7.38: Experimental results of sensorless torque control, when f_e = 3 Hz and the SPMSM generated the rated torque.

In the lowest speed case shown in Figure 7.36(a), f_e was lower than 0.3 Hz. The machine rotor speed was well regulated, and the position estimation error was limited within ±6 electric degrees. The corresponding phase currents, i_a and i_b, which contained both fundamental and HF components, are shown in Figure 7.37. The time scale in Figure 7.37 is 500 ms per division. Since the frequency of the injected signal is 200 Hz, in the highest speed case shown in Figure 7.36(g) where f_e is 12 Hz, there were less than 17 (≈ 200/12) control cycles per electric revolution. Under this circumstance, the machine rotor speed was still well regulated, and the position estimation error was limited to within ±10 electric degrees, which, however, was larger than other cases with more control cycles per electric revolution. Due to the limitations of the DC-bus voltage and the cutoff frequency of the LC filter on the inverter board, the frequency of the injected signal could not be increased further. However, as obvious by the trend, shown in Figure 7.36, if the frequency of the injected signal could be further increased, the SPMSM could be well controlled for higher operating speed. The results for the ramp speed test are show in Figure 7.36(h), where the reference speed was increased and decreased linearly between 0.3 and 12 Hz. In this circumstance, the rotor speed was also well regulated.

When the test SPMSM worked as a generator, the output torque of the machine was regulated. The shaft speed of the test SPMSM was maintained by the other SPMSM, which worked in the speed control mode. The AC power generated by the test SPMSM was converted to DC power by a three-phase IGBT converter. A DC electronic load was connected in parallel with a DC source to consume the electric power generated. The function of the DC source was to stabilize the DC-terminal voltage of the converter. Some typical experimental results of the sensorless torque control are shown in Figure

7.38. The test SPMSM generated the rated torque, and f_e was maintained at 3 Hz. The results shown in Figure 7.38 are consistent with the simulation results shown in Figure 7.33, since no load-dependent position offset was observed. The magnitude of the position estimation error was also close to that of the no-load cases shown in Figure 7.36.

CHAPTER 8

CONCLUSIONS, CONTRIBUTIONS, AND RECOMMENDATIONS FOR FUTURE RESEARCH

8.1 Conclusions of This Dissertation

The goal of the research conducted for this dissertation was to develop rotor position/speed sensorless control with performance comparable to the sensor-based controls for PMSMs over a wide operating range, including low-speed operation. Innovative rotor position/speed estimation methods were proposed, investigated, and validated in this dissertation.

The sensorless control investigated offers an effective means to solving the problems incurred in using electromechanical sensors in PMSM control systems. This dissertation covers four major issues and solutions related to the rotor position/speed sensorless control of PMSMs, including,

- Sensorless control of a salient-pole PMSM using a low sampling ratio.
- Sensorless control of PMSMs using model-based methods for low speed operation.
- The stability of a sensorless PMSM drive system under large load transient.
- Sensorless control of nonsalient-pole PMSMs using saliency-based methods for low-speed operation.

The following conclusions can be drawn based on the fulfillment of the dissertation research.

For this dissertation, research was conducted on an adaptive quasi-sliding-mode position observer for sensorless control of salient-pole PMSMs operating in medium- and high-speed conditions. The adaptive QSMO is robust in terms of load variations and allows the state trajectory of the QSMO to quickly converge into the boundary layer designed around the sliding surface. The global stability and quasi-sliding-mode motion are guaranteed using the proposed adaptive switching function. Experimental results verified that the QSMO with the linear parameter adaption schemes had good steady-state and transient performance over a wide range of speeds and loads. The performance of the adaptive QSMO does not degrade even when using a low sampling ratio in high-speed and heavy-load conditions. As shown in the experimental results, the sensorless drive using the adaptive QSMO performs excellently under ramp torque changes with different slew rates, symmetrical performance for four-quadrant operations, and excellent ride-through capability under complete torque reversals. These capabilities, however, cannot be achieved by using the conventional DSMO without the parameter adaption scheme.

Research was conducted on both the EEMF-based and extended flux model-based QSMOs. The novel extended flux model was derived by using a mathematical model reconstruction process, which was proposed for the dynamic modeling of a generic salient-pole PMSM. The extended flux model has the notable advantages of simpler structure and improved robustness to the variations of machine parameters and operating conditions (both speed and torque) when compared to the EEMF-based model. To further improve the dynamic performance and low-speed operating capability of the sensorless

control system, a dynamic position compensator was also investigated. Extensive simulation and experimental results validated the rotor position estimator and sensorless control. The results show that compared to the commonly used EEMF-based position estimators, the extended flux model-based rotor position estimator has much better dynamic performance, improved capability in very low-speed operating conditions, and is robust in terms of speed and torque variations of the system.

A robust MRAS-based rotor speed estimator using a heterodyning speed adaption mechanism has been investigated for sensorless PMSM drives. The MRAS contains an improved reference model, which uses an ALE to provide better noise cancellation capability for the EEMF estimated from a QSMO. The rotor speed estimator has two operating modes that are suitable for generator and motor applications, respectively. Furthermore, a novel oscillation mitigation algorithm using the estimated rotor speed as a feedback input signal was proposed to work with the conventional inverse tangent method for rotor position estimation. This algorithm can mitigate the oscillations in the estimated rotor position caused by the noisy content in the estimated EEMF. Simulation and experimental results on a heavy-duty IPMSM drive system were provided to validate the performance of rotor position and speed estimators and to evaluate the effects of key parameters on the performance of the estimators. The implementation of the proposed method is simple and has a low computational cost and, therefore, has great potential for industrial applications.

In this dissertation, a square-wave voltage injection-based rotor position/speed estimator was investigated for nonsalient-pole PMSMs, e.g., SPMSMs, operating in the low-speed range. In the estimator, the HF signal is injected into the estimated rotor

reference frame; the rotor position is then estimated from the envelopes of the induced HF current components in the stationary reference frame. Compared to conventional methods, the proposed rotor position estimator is much less dependent on the rotor spatial saliency. Therefore, it is well suited for SPMSM applications. By using the square-wave signal injection, the operating speed range of the speed controller is at least twice higher than that when using the sinusoidal signal injection. The rotor position/speed estimation scheme and sensorless control were validated by simulation and experimental results.

8.2 Contributions of This Dissertation

The contributions of this dissertation are summarized as follows:

- The existing methods for rotor position/speed estimation and sensorless control of both salient-pole and nonsalient-pole PMSMs have been reviewed in this dissertation.
- A QSMO has been proposed to estimate the EEMF components of a salient-pole PMSM. Online parameter adaption schemes have been proposed to guarantee the stability of the observer and the quasi-sliding mode motion of the state trajectory. The rotor position estimation accuracy of the proposed QSMO is acceptable even under a low sampling ratio.
- A model reconstruction process has been proposed to obtain proper machine models for rotor position/speed observation. A novel extended flux model has been derived by using the proposed model reconstruction process. Then another QSMO has been proposed to

estimate the extended flux components of a salient-pole PMSM. Moreover, a dynamic position compensator has been proposed to work together with the QSMO to further improve the dynamic response of the QSMO. The integrated rotor position/speed estimator has improved dynamic performance and better capability in low-speed operation than the rotor position estimator based on the EEMF-based QSMO.

- A robust MRAS-based rotor speed estimator using a heterodyning speed adaption mechanism has been proposed for sensorless PMSM drives. The MRAS contains an improved reference model, which uses an ALE to provide a better noise cancellation capability for the EEMF estimated from a QSMO.
- A novel oscillation mitigation algorithm using the estimated rotor speed as a feedback input signal has been proposed to work with the conventional inverse tangent method for rotor position estimation. This algorithm mitigates the oscillations in the estimated rotor position caused by the noisy content in the estimated EEMF.
- A HF square-wave voltage injection-based rotor position/speed estimator has been proposed for nonsalient-pole PMSMs, e.g., SPMSMs, operating in the low-speed range. Compared to conventional methods, the proposed rotor position/speed estimator has much less dependence on the rotor spatial saliency. Therefore, it is well suited for SPMSM applications.

- Three sets of sensorless control platforms were built in Matlab Simulink. Simulation studies are performed to validate the effectiveness of proposed sensorless control systems.
- Three sets of experimental test setups using different types of PMSMs with different power ratings were built to further validate the effectiveness of the proposed sensorless control systems. Extensive experimental results and their analysis were presented in this dissertation.

8.3 Recommendations for Future Research

Recommendations for future research are listed as follows:

- Perform reliability analysis for the sensorless drive system. One of major drawbacks of the position sensor is its high failure rate in a harsh environment. Although numerous sensorless control schemes have been proposed for different applications, neither reliability analysis nor failure mechanism study of the sensorless control system can be found in the existing literature.
- When using a model based position observer, the reference voltages generated by current regulators instead of machine terminal voltages can be used in the observer model. However, for generator type application, at a certain operating speed (the shaft speed is maintained by the prime mover) and at no load condition (no phase current), the rotor position cannot be identified by using a model based observer. A

method is desired to estimate rotor position information under this circumstance without using voltage sensors.

- Investigate the relationship between current regulation quality and rotor position estimation quality. In model based observer, since rotor position is estimated based on the measured currents, there will be a certain relationship between current regulation quality and rotor position estimation quality. This relationship can be further used for condition monitoring purpose, e.g., to detect the current sensor fault.
- Investigate the performance of drive system using a combination of rotor position estimator and low-cost position sensors.
- Develop a smooth transition scheme between saliency-based rotor position estimator (low-speed operation) and model-based rotor position estimator (for medium- and high-speed operation).
- If the sensorless drive has the capability to perform signal injection for low-speed operation, more value-added schemes can be investigated to fully use this capability, e.g., using the signal injection-based method to estimate the rotor temperature for condition monitoring purposes.

Appendix A

Inequality Derived from Stability Condition 1)

According to Equations (3.16) and (3.17), if $\boldsymbol{\varepsilon_\alpha}[k] > Z_0$, then $Z_\alpha = Z_0$. In this condition, $\boldsymbol{\varepsilon_\alpha}[k+1] < \boldsymbol{\varepsilon_\alpha}[k]$ needs to be satisfied. Thus,

$$\varepsilon_\alpha[k+1]-\varepsilon_\alpha[k]=-\frac{T_s R}{L_d}\varepsilon_\alpha[k]+T_s E_\alpha[k]-T_s l Z_0<0 \tag{A-1}$$

which is equivalent to $lZ_0+\frac{R}{L_d}\varepsilon_\alpha[k]>E_\alpha[k]$.

Since $\boldsymbol{\varepsilon_\alpha}[k] > Z_0 > 0$, $\frac{R}{L_d}\varepsilon_\alpha[k]>\frac{R}{L_d}Z_0$. Thus, if the following inequality is satisfied, Equation (A-1) will also be satisfied.

$$\left(l+\frac{R}{L_d}\right)Z_0>E_\alpha[k] \tag{A-2}$$

If $\boldsymbol{\varepsilon_\alpha}[k] < -Z_0$, then $Z_\alpha = -Z_0$. In this case, $\boldsymbol{\varepsilon_\alpha}[k+1] > \boldsymbol{\varepsilon_\alpha}[k]$ needs to be satisfied. Thus,

$$\varepsilon_\alpha[k+1]-\varepsilon_\alpha[k]=-\frac{T_s R}{L_d}\varepsilon_\alpha[k]+T_s E_\alpha[k]+T_s l Z_0>0 \tag{A-3}$$

which is equivalent to $lZ_0-\frac{R}{L_d}\varepsilon_\alpha[k]>-E_\alpha[k]$.

Since $\boldsymbol{\varepsilon_\alpha}[k] < -Z_0 < 0$, $-\frac{R}{L_d}\varepsilon_\alpha[k]>\frac{R}{L_d}Z_0$. Thus, if the following inequality is satisfied, Equation (A-3) will also be satisfied.

$$\left(l+\frac{R}{L_d}\right)Z_0>-E_\alpha[k] \tag{A-4}$$

According to Equations (A-2) and (A-4), since R/L_d is positive, a stronger condition can be obtained as

$$lZ_0 > |E_\alpha[k]| \tag{A-5}$$

so that both Equations (A-2) and (A-4) are satisfied, as well as Condition 1).

Appendix B

Inequality Derived from Stability Condition 2)

If $\boldsymbol{\varepsilon_\alpha}[k] > Z_0$, then $Z_\alpha = Z_0$. In this condition, $\boldsymbol{\varepsilon}[k+1] + \boldsymbol{\varepsilon}[k] > 0$ needs to be satisfied. Thus,

$$\varepsilon_\alpha[k+1]+\varepsilon_\alpha[k]=\left(2-\frac{T_s R}{L_d}\right)\varepsilon_\alpha[k]+T_s E_\alpha[k]-T_s l Z_0>0 \tag{B-1}$$

which is equivalent to $lZ_0<\left(\frac{2}{T_s}-\frac{R}{L_d}\right)\varepsilon_\alpha[k]+E_\alpha[k]$.

Since $\boldsymbol{\varepsilon_\alpha}[k] > Z_0 > 0$, $\left(\frac{2}{T_s}-\frac{R}{L_d}\right)Z_0<\left(\frac{2}{T_s}-\frac{R}{L_d}\right)\varepsilon_\alpha[k]$. Thus, if the following inequality is satisfied, Equation (B-1) will also be satisfied:

$$lZ_0<\left(\frac{2}{T_s}-\frac{R}{L_d}\right)Z_0+E_\alpha[k] \tag{B-2}$$

If $\boldsymbol{\varepsilon_\alpha}[k] < -Z_0$, then $Z_\alpha = -Z_0$. In this condition, $\boldsymbol{\varepsilon}[k+1] + \boldsymbol{\varepsilon}[k] < 0$ needs to be satisfied. Thus,

$$\varepsilon_\alpha[k+1]+\varepsilon_\alpha[k]=\left(2-\frac{T_s R}{L_d}\right)\varepsilon_\alpha[k]+T_s E_\alpha[k]+T_s l Z_0<0 \tag{B-3}$$

which can be formulated as: $lZ_0<-\left(\frac{2}{T_s}-\frac{R}{L_d}\right)\varepsilon_\alpha[k]-E_\alpha[k]$.

Since $\boldsymbol{\varepsilon_\alpha}[k] < -Z_0 < 0$, $\left(\frac{2}{T_s}-\frac{R}{L_d}\right)Z_0<-\left(\frac{2}{T_s}-\frac{R}{L_d}\right)\varepsilon_\alpha[k]$. Thus, if the following inequality is satisfied, Equation (B-3) will also be satisfied:

$$lZ_0 < \left(\frac{2}{T_s} - \frac{R}{L_d} \right) Z_0 - E_\alpha[k] \tag{B-4}$$

According to Equations (B-2) and (B-4), a stronger condition can be obtained as

$$lZ_0 < \left(\frac{2}{T_s} - \frac{R}{L_d} \right) Z_0 - \left| E_\alpha[k] \right| \tag{B-5}$$

so that both (B-2) and (B-4) are satisfied, as well as Condition 2).

In order to satisfy both Conditions 1) and 2), both Equations (A-5) and (B-5) should be used, which draws (3.18-I). To guarantee the existence of lZ_0, the upper boundary in Equation (B-5) should be larger than the lower boundary in Equation (A-5), which draws (3.18-II).

Appendix C

Proof of the Stability of the Proposed MRAS-Based Speed Estimator

According to Equations (4.3), (4.4), and (4.11), the following relations can be obtained: $\dot{\hat{E}}^n_{\alpha\beta} = \omega_{re} J \cdot \hat{E}^n_{\alpha\beta}$ and $\dot{\tilde{E}}^n_{\alpha\beta} = \hat{\omega}_{re} J \cdot \tilde{E}^n_{\alpha\beta} + L \cdot \left(\hat{E}^n_{\alpha\beta} - \tilde{E}^n_{\alpha\beta} \right)$. Then the differential equation of the EEMF tracking error is defined and examined as follows:

$$\dot{\varepsilon}^n_{\alpha\beta} = \dot{\hat{E}}^n_{\alpha\beta} - \dot{\tilde{E}}^n_{\alpha\beta} = \underbrace{\left(\omega_{re} J - L \right)}_{A} \cdot \varepsilon^n_{\alpha\beta} - \underbrace{\left(\hat{\omega}_{re} - \omega_{re} \right) J \cdot \tilde{E}^n_{\alpha\beta}}_{W} \tag{C-1}$$

To guarantee the stability of the MRAS, the following two Popov's hyperstability criteria [94] should be satisfied simultaneously:

1) the forward path transfer matrix $(sI - A)^{-1}$ is strictly positive real. This can be theoretically verified and the verification process is the same as that in [44], which will not be repeated in this part.

2) $\int_0^{t_0} \left[\left(\varepsilon^n_{\alpha\beta} \right)^T \cdot W \right] dt \geq -\gamma^2$ for all $t_0 \geq 0$, where γ^2 is a positive real constant. When the heterodyning speed adaption scheme, Equation (4.10), is chosen, a brief proof of the second criterion is given below.

$$\begin{aligned} \int_0^{t_0} \left[\left(\varepsilon^n_{\alpha\beta} \right)^T \cdot W \right] dt &= \int_0^{t_0} \left\{ \left(\varepsilon^n_{\alpha\beta} \right)^T \cdot J \cdot \tilde{E}^n_{\alpha\beta} \left(\hat{\omega}_{re} - \omega_{re} \right) \right\} dt \\ &= \int_0^{t_0} \left\{ \left(\hat{E}^n_{\beta} \tilde{E}^n_{\alpha} - \hat{E}^n_{\alpha} \tilde{E}^n_{\beta} \right) \left(\hat{\omega}_{re} - \omega_{re} \right) \right\} dt \end{aligned} \tag{C-2}$$

Substituting Equation (4.10) into Equation (C-2) yields:

$$\int_0^{t_0}\left[\left(\varepsilon_{\alpha\beta}^n\right)^T\cdot W\right]dt=\int_0^{t_0}\left\{\left(\hat{E}_\beta^n\tilde{E}_\alpha^n-\hat{E}_\beta^n\tilde{E}_\alpha^n\right)\left[\left(k_p+\frac{k_i}{s}\right)\left(\hat{E}_\beta^n\tilde{E}_\alpha^n-\hat{E}_\alpha^n\tilde{E}_\beta^n\right)-\omega_{re}\right]\right\}dt$$
$$=\underbrace{k_p\int_0^{t_0}\left(\hat{E}_\beta^n\tilde{E}_\alpha^n-\hat{E}_\beta^n\tilde{E}_\alpha^n\right)^2dt}_{I}+\underbrace{\int_0^{t_0}\left\{\left(\hat{E}_\beta^n\tilde{E}_\alpha^n-\hat{E}_\alpha^n\tilde{E}_\beta^n\right)\left[k_i\int\left(\hat{E}_\beta^n\tilde{E}_\alpha^n-\hat{E}_\alpha^n\tilde{E}_\beta^n\right)d\tau-\omega_{re}\right]\right\}dt}_{II} \quad \text{(C-3)}$$

where the first term *I* is nonnegative. For the second term *II*, denote

$$f(t)=k_i\int\left(\hat{E}_\beta^n\tilde{E}_\alpha^n-\hat{E}_\alpha^n\tilde{E}_\beta^n\right)d\tau-\omega_{re},$$

such that

$$\frac{d\left[f(t)\right]}{dt}=k_i\left(\hat{E}_\beta^n\tilde{E}_\alpha^n-\hat{E}_\alpha^n\tilde{E}_\beta^n\right).$$

Then,

$$II=\int_0^{t_0}\left\{\frac{1}{k_i}\frac{d\left[f(t)\right]}{dt}f(t)\right\}dt=\frac{1}{2k_i}\left[f^2(t_0)-f^2(0)\right]\geq-\frac{1}{2k_i}f^2(0).$$

Thus,

$$\int_0^{t_0}\left[\left(\varepsilon_{\alpha\beta}^n\right)^T\cdot W\right]dt=I+II\geq 0-\frac{1}{2k_i}f^2(0)=-\frac{1}{2k_i}f^2(0).$$

Define $\gamma^2=\frac{1}{2k_i}f^2(0)$, which a positive real constant. Therefore, the second criterion is satisfied.

Bibliography

[1] S.-K. Sul, *Control of Electric Machine Drive Systems*, 1st Edition, John Wiley & Sons, Inc., Hoboken, New Jersey, 2011.

[2] D. W. Novotny and T. A. Lipo, *Vector Control and Dynamics of AC Drives*, Oxford University Press Inc., New York, 1996.

[3] W. Leonhard, *Control of Electrical Drives*, 3rd Edition, Springer, Berlin, 2001.

[4] S. Chi, Z. Zhang, and L. Xu, "Sliding-mode sensorless control of direct-drive PM synchronous motors for washing machine applications," *IEEE Trans. Industry Applications*, vol. 45, no. 2, pp. 582-590, Mar.-Apr. 2009.

[5] K. T. Chau, C. C. Chan, and C. Liu, "Overview of permanent-magnet brushless drives for electric and hybrid electric vehicles," *IEEE Trans. Industrial Electronics*, vol. 55, no. 6, pp. 2246-2257, June 2008.

[6] M. Chinchilla, S. Arnaltes, and J. C. Burgos, "Control of permanent-magnet generators applied to variable-speed wind-energy systems connected to the grid," *IEEE Trans. Energy Conversion*, vol. 21, no. 1, pp. 130-135, March 2006.

[7] S. T. Lee, "Development and analysis of interior permanent magnet synchronous motor with field excitation structure," Ph.D. dissertation, Dept. Elect. Eng., University of Tennessee, Knoxville, TN, 2009.

[8] R. Krishnan, *Permanent Magnet Synchronous and Brushless DC motor Drives*, 1st Edition, CRC press, Taylor & Francis Group, FL, 2009.

[9] A. Vagati, G. Pellegrino, and P. Guglielmi, "Comparison between SPM and IPM motor drives for EV application," in *Proc. International Conference on Electrical Machines*, Sept. 2010, pp. 1-6.

[10] A. M. EL-Refaie and T. M. Jahns, "Comparison of synchronous PM machine types for wide constant-power speed range operation," in *Proc. IEEE Industry Applications Society Annual Meeting*, vol. 2, Oct. 2005, pp. 1015-1022.

[11] Department of Energy, "EV Everywhere: Grand Challenge Blueprint," 2013, [Online]. Available: http://www1.eere.energy.gov/vehiclesandfuels/electric_vehicles/pdfs/evevery where_blueprint.pdf).

[12] Department of Energy, "EV Everywhere Grand Challenge: Traction Drive System," 2012, [Online]. Available http://www1.eere.energy.gov/vehiclesandfuels/pdfs/ev_everywhere/ 9a_miller_ed. pdf).

[13] C. C. Chan, "The state of the art of electric and hybrid vehicles," *Proceedings of the IEEE*, vol. 90, no. 2, pp. 247-275, Feb 2002.

[14] C. C. Chan, "The state of the art of electric, hybrid, and fuel cell vehicles," *Proceedings of the IEEE*, vol. 95, no. 4, pp. 704-718, April 2007.

[15] A. Emadi, Y. -J. Lee, and K. Rajashekara, "Power electronics and motor drives in electric, hybrid electric, and plug-in hybrid electric vehicles," *IEEE Trans. Industrial Electronics*, vol. 55, no. 6, pp. 2237-2245, June 2008.

[16] M. Ehsani, K. M. Rahman, and H. A. Toliyat, "Propulsion system design of electric and hybrid vehicles," *IEEE Trans. Industrial Electronics*, vol. 44, no. 1, pp. 19–27, Feb. 1997.

[17] Z. Q. Zhu and D. Howe, "Electrical machines and drives for electric, hybrid, and fuel cell vehicles," *Proceedings of the IEEE*, vol. 95, no. 4, pp. 746-765, April 2007.

[18] T. M. Jahns, G. B. Kliman, and T. Neumann, "Interior permanent-magnet synchronous motors for adjustable-speed drives," *IEEE Trans. Industry Applications*, vol. IA-22, no. 4, pp. 738-747, July 1986.

[19] S. Morimoto, M. Sanada, and Y. Takeda, "Wide-speed operation of interior permanent magnet synchronous motors with high-performance current regulator," *IEEE Trans. Industry Applications*, vol. 30, no. 4, pp. 920-926, Jul/Aug 1994.

[20] M. Olszewski, Evaluation of the 2010 Toyota Prius Hybrid Synergy Drive System, Oak Ridge National Laboratory, U.S. Department of Energy, USA, 2011, [Online]. Available: http://info.ornl.gov/sites/publications/files/Pub26762.pdf

[21] "The World Wind Energy Association: Half-year Report 2013," [Online]. Available: http://www.wwindea.org.

[22] A.D. Hansen, F. Iov, F. Blaabjerg, and L.H. Hansen, "Review of contemporary wind turbine concepts and their market penetration," *J. Wind Eng.*, vol. 58, no. 4, pp. 1081-1095, Apr. 2011.

[23] M. Liserre, R. Cardenas, M. Molinas, and J. Rodriguez, "Overview of multi-MW wind turbines and wind parks," *IEEE Trans. Industrial Electronics*, vol. 58, no. 4, pp. 1081-1095, Apr. 2011.

[24] "Wind Energy-The Facts," [Online]. Available: http://www.wind-energy-the-facts.org.

[25] "Siemens 6.0 MW Offshore Wind Turbine," [Online]. Available: http://www.energy.siemens.com.

[26] N. Mohan, *Advanced Electric Drives: Analysis, Control and Modeling Using Simulink*, MNPERE, 2001.

[27] B. Cheng and T. R. Tesch, "Torque feedforward control technique for permanent-magnet synchronous motors," *IEEE Trans. Industrial Electronics*, vol. 57, no. 3, pp. 969-974, March 2010.

[28] M. Pacas, "Sensorless drives in industrial applications," *IEEE Industrial Electronics Magazine*, vol. 5, no.2, pp. 16-23, Jun. 2011.

[29] P. P. Acarnley and J. F. Watson, "Review of position-sensorless operation of brushless permanent-magnet machines," *IEEE Trans. Industrial Electronics*, vol. 53, no. 2, pp. 352-362, April 2006.

[30] K. -W. Lee and J. -I. Ha, "Evaluation of back-EMF estimators for sensorless control of permanent magnet synchronous motors," *Journal of Power Electronics*, vol. 12, no. 4, pp. 1-11, July 2012.

[31] Y. Zhao, C. Wei, Z. Zhang, and W. Qiao, "A Review on position/speed sensorless control for permanent-magnet synchronous machine-based wind energy conversion systems," *IEEE Journal of Emerging and Selected Topics in Power Electronics*, vol. 1, no. 4, pp. 203-216, Dec. 2013.

[32] Y. Li and H. Zhu, "Sensorless control of permanent magnet synchronous motor−A survey," in *Proc. 2008 Vehicle Power and Propulsion Conference*, Sept. 2008, pp. 1-8.

[33] K. Iizuka, H. Uzuhashi, M. Kano, T. Endo, and K. Mohri, "Microcomputer control for sensorless brushless motor," *IEEE Trans. Industry Applications*, vol. 21, no. 3, pp. 595–601, July/Aug. 1985.

[34] S. Ogasawara and H. Akagi, "An approach to position sensorless drive for brushless DC motors," *IEEE Trans. Industry Applications*, vol. 27, no. 5, pp. 928–933, Sept./Oct. 1991.

[35] J. C. Moreira, "Indirect sensing for rotor flux position of permanent magnet AC motors operating over a wide speed range," *IEEE Trans. Industry Applications*, vol. 32, no. 6, pp. 1394–1401, Nov./Dec. 1996.

[36] F. Profumo, G. Griva, M. Pastorelli, J. C. Moreira, and R. D. Donker, "Universal field oriented controller based on airgap flux sensing via third-harmonic stator voltage," *IEEE Trans. Industry Applications*, vol. 30, pp. 448–455, Mar./Apr. 1994.

[37] J. X. Shen, Z. Q. Zhu, and D. Howe, "Sensorless flux-weakening control of permanent-magnet brushless machines using third harmonic back EMF," *IEEE Trans. Industry Applications*, vol. 40, no. 6, pp. 1629–1636, Nov./Dec. 2004.

[38] J. M. Liu and Z. Q. Zhu, "Improved sensorless control of permanent magnet synchronous machine based on third-harmonic back-EMF," in *Proc. IEEE International Electric Machines & Drives Conference*, May 2013, pp. 1180-1187.

[39] M. Naidu and B. K. Bose, "Rotor position estimation scheme of a permanent magnet synchronous machine for high performance variable speed drive," in *Proc. IEEE Industry Applications Society Annual Meeting*, vol. 1, Oct. 1992, pp. 48-53.

[40] R. Wu and G. R. Slemon, "A permanent magnet motor drive without a shaft sensor," *IEEE Trans. Industry Applications*, vol. 27, no. 5, pp. 1005-1011, Sep./Oct. 1991.

[41] J. X. Shen, Z. Q. Zhu, and D. Howe, "Improved speed estimation in sensorless PM brushless AC drives," *IEEE Trans. Industry Applications*, vol. 38, no. 4, pp. 1072-1080, Jul./Aug. 2002.

[42] A. B. Kulkarni and M. Ehsani, "A novel position sensor elimination technique for the interior permanent-magnet synchronous motor drive," *IEEE Trans. Industry Applications*, vol. 28, no. 1, pp. 144-150, Jan./Feb. 1992.

[43] M. A. Hoque and M. A. Rahman, "Speed and position sensorless permanent magnet synchronous motor drives," in *Proc. Canadian Conference on Electrical and Computer Engineering*, pp. 689-692, Sept. 1994.

[44] M. Tomita, T. Senjyu, S. Doki, and S. Okuma, "New sensorless control for brushless DC motors using disturbance observers and adaptive velocity estimations," *IEEE Trans. Industrial Electronics*, vol. 45, no. 2, pp. 274-282, Apr 1998.

[45] Z. Chen, M. Tomita, S. Doki, and S. Okuma, "An extended electromotive force model for sensorless control of interior permanent-magnet synchronous motors," *IEEE Trans. Industrial Electronics*, vol. 50, no. 2, pp. 288- 295, Apr. 2003.

[46] S. Morimoto, K. Kawamoto, M. Sanada, and Y. Takeda, "Sensorless control strategy for salient-pole PMSM based on extended EMF in rotating reference frame," *IEEE Trans. Industry Applications*, vol. 38, no. 4, pp. 1054-1061, Jul./Aug. 2002.

[47] H. Kim, M. C. Harke, and R. D. Lorenz, "Sensorless control of interior permanent-magnet machine drives with zero-phase lag position estimation," *IEEE Trans. Industry Applications*, vol. 39, no. 6, pp. 1726-1733, Nov./Dec. 2003.

[48] M. Hasegawa, S. Yoshioka, and K. Matsui, "Position sensorless control of interior permanent magnet synchronous motors using unknown input observer for high-speed drives," *IEEE Trans. Industry Applications*, vol. 45, no. 3, pp. 938-946, May/June 2009.

[49] S. Chi, Z. Zhang, and L. Xu, "Sliding-mode sensorless control of direct-drive PM synchronous motors for washing machine applications," *IEEE Trans. Industry Applications*, vol. 45, no. 2, pp. 582-590, Mar.-Apr. 2009.

[50] W. Qiao, X. Yang, and X. Gong, "Wind speed and rotor position sensorless control for direct-drive PMG wind turbines," *IEEE Trans. Industry Applications*, vol. 48, no. 1, pp. 3-11, Jan.-Feb. 2012.

[51] H. Kim, J. Son, and J. Lee, "A high-speed sliding-mode observer for the sensorless speed control of a PMSM," *IEEE Trans. Industrial Electronics*, vol. 58, no. 9, pp. 4069-4077, Sept. 2011.

[52] G. Foo and M. F. Rahman, "Sensorless sliding-mode MTPA control of an IPM synchronous motor drive using a sliding-mode observer and HF signal injection," *IEEE Trans. Industrial Electronics*, vol. 57, no. 4, pp. 1270-1278, Apr. 2010.

[53] Y. Zhao, W. Qiao, and L. Wu, "An adaptive quasi sliding-mode rotor position observer-based sensorless control for interior permanent magnet synchronous machines," *IEEE Trans. Power Electronics*, vol. 28, no. 12, pp. 5618-5629, Dec. 2013.

[54] J. Liu, J. Hu, and L. Xu, "Sliding mode observer for wide speed range sensorless - induction machine drives: Considerations for digital implementation," in *Proc. IEEE International Conference on Electric Machines and Drives*, Jun. 2005, pp. 300-307.

[55] X. Xiao, Y. Li, M. Zhang, and Y. Liang, "A sensorless control based on MRAS method in interior permanent-magnet machine drive," in *Proc. International Conference on Power Electronics and Drives Systems*, Nov.-Dec. 2005, pp. 734-738.

[56] Y. Shi, K. Sun, L. Huang, and Y. Li, "Online identification of permanent magnet flux based on extended kalman filter for IPMSM drive with position sensorless control," *IEEE Trans. Industrial Electronics*, vol. 59, no. 11, pp. 4169-4178, Nov. 2012.

[57] F. Z. Peng and T. Fukao, "Robust speed identification for speed sensorless vector control of induction motors," *IEEE Trans. Industry Applications*, vol. 30, no. 5, pp. 1234–1240, Sep./Oct. 1994.

[58] F. Dezza, G. Foglia, M. Iacchetti, and R. Perini, "An MRAS observer for sensorless DFIM drives with direct estimation of the torque and flux rotor current components," *IEEE Trans. Power Electronics*, vol. 27, no. 5, pp. 2576-2584, May 2012.

[59] S. Bolognani, L. Tubiana, and M. Zigliotto, "Extended Kalman filter tuning in sensorless PMSM drives," *IEEE Trans. Industry Applications*, vol. 39, no. 6, pp. 1741-1747, Nov./Dec. 2003.

[60] S. Bolognani, L. Tubiana, and M. Zigliotto, "EKF-based sensorless IPM synchronous motor drive for flux-weakening applications," *IEEE Trans. Industry Applications*, vol. 39, no. 3, pp. 768-775, May/Jun. 2003.

[61] R. Hoseinnezhad and P. Harding, "A novel hybrid angle tracking observer for resolver to digital conversion," in *Proc. 44th IEEE Conference on Decision and Control and 2005 European Control Conference*, Dec. 2005, pp. 7020- 7025.

[62] R. D. Lorenz and K. W. Van Patten, "High-resolution velocity estimation for all-digital, AC servo drives," *IEEE Trans. Industry Applications*, vol. 27, no. 4, pp. 701-705, Jul./Aug. 1991.

[63] M. Elbuluk and C. Li, "Sliding mode observer for wide-speed sensorless control of PMSM drives," in *Proc. IEEE IAS Annual Meeting*, vol. 1, Oct. 2003, pp. 480- 485.

[64] F. Briz and M. W. Degner, "Rotor position estimation," *IEEE Industrial Electronics Magazine*, vol. 5, no. 2, pp. 24-36, June 2011.

[65] F. Briz, M. W. Degner, P. Garcia, and R. D. Lorenz, "Comparison of saliency-based sensorless control techniques for ac machines," *IEEE Trans. Industry Applications*, vol. 40, no. 4, pp. 1107-1115, July/Aug. 2004.

[66] N. Bianchi and S. Bolognani, "Influence of rotor geometry of an IPM motor on sensorless control feasibility," *IEEE Trans. Industry Applications*, vol. 43, no. 1, pp. 87-96, Jan./Feb. 2007.

[67] J. Jang, S. Sul, J. Ha, K. Ide, and M. Sawamura, "Sensorless drive of surface-mounted permanent-magnet motor by high-frequency signal injection based on magnetic saliency," *IEEE Trans. Industry Applications*, vol. 39, no. 4, pp. 1031-1039, July/Aug. 2003.

[68] P. Garcia, D. Reigosa, F. Briz, C. Blanco, and J. Guerrero, "Sensorless control of surface permanent magnet synchronous machines using the high frequency resistance," in *Proc. IEEE Energy Conversion Congress and Exposition*, Sept. 2011, pp. 2709-2716.

[69] M. J. Corley and R. D. Lorenz, "Rotor position and velocity estimation for a salientpole permanent magnet synchronous machine at standstill and high speeds," *IEEE Trans. Industry Applications*, vol. 34, no. 4, pp. 784–789, July/Aug. 1998.

[70] P. Jansen and R. Lorenz, "Transducerless field orientation concepts employing saturation-induced saliencies induction machines," *IEEE Trans. Industry Applications*, vol. 32, no. 6, pp. 1380-1393, Nov/Dec 1996.

[71] J.-I. Ha, K. Ide, T. Sawa, and S.-K. Sul, "Sensorless rotor position estimation of an interior permanent-magnet motor from initial states," *IEEE Trans. Industry Applications*, vol. 39, no. 3, pp. 761–767, May/June 2003.

[72] Y. Yoon, S. Sul, S. Morimoto, and K. Ide, "High-bandwidth sensorless algorithm for AC Machines based on square-wave-type voltage injection," *IEEE Trans. Industry Applications*, vol. 47, no. 3, pp. 1361-1370, May/June 2011.

[73] E. Robeischl and M. Schroedl, "Optimized INFORM measurement sequence for sensorless PM synchronous motor drives with respect to minimum current distortion," *IEEE Trans. Industry Applications*, vol. 40, no. 2, pp. 591–598, Mar./Apr. 2004.

[74] Y. Hua, G. M. Asher, M. Sumner, and Q. Gao, "Sensorless control of surface mounted permanent magnetic machine using the standard space vector PWN," in *Proc. IEEE Industry Applications Society Annual Meeting*, Sept. 2007, pp. 661-667.

[75] S. Yang and R. Lorenz, "Surface permanent-magnet machine self-sensing at zero and low speeds using improved observer for position, velocity, and disturbance torque estimation," *IEEE Trans. Industry Applications*, vol. 48, no. 1, pp. 151-160, Jan./Feb. 2012.

[76] J. Lee, J. Hong, K. Nam, R. Ortega, L. Praly, and A. Astolfi, "Sensorless control of surface-mount permanent-magnet synchronous motors based on a nonlinear observer," *IEEE Trans. Power Electronics*, vol. 25, no. 2, pp. 290-297, Feb. 2010.

[77] D. Reigosa, P. Garcia, F. Briz, D. Raca, and R. D. Lorenz, "Modeling and adaptive decoupling of high-frequency resistance and temperature effects in carrier-based sensorless control of PM synchronous machines," *IEEE Trans. Industry Applications*, vol. 46, no. 1, pp. 139-149, Jan./Feb. 2010.

[78] J. Hu, J. Liu, and L. Xu, "Eddy current effects on rotor position estimation and magnetic pole identification of PMSM at zero and low speeds," *IEEE Trans. Power Electronics*, vol. 23, no. 5, pp. 2565-2575, Sept. 2008.

[79] M. Schroedl, "Sensorless control of AC machines at low speed and standstill based on the "INFORM" method," in *Proc. IEEE Industry Applications Society Annual Meeting*, vol. 1, Oct 1996, pp. 270-277.

[80] L. Ribeiro, M. Degner, F. Briz, and R. D. Lorenz, "Comparison of carrier signal voltage and current injection for the estimation of flux angle or rotor position," in *Proc. IEEE Industry Applications Society Annual Meeting*, vol. 1, Oct. 1998, pp. 452-459.

[81] J. Liu and Z. Q. Zhu, "Sensorless control strategy by square waveform high frequency pulsating signal injection into stationary reference frame," *IEEE Journal of Emerging and Selected Topics in Power Electronics*, vol. 2, no. 2, pp. 171-180, June 2014.

[82] C.–H. Choi and J.–K. Seok, "Pulsating signal injection-based axis switching sensorless control of surface-mounted permanent-magnet motors for minimal zero-current clamping effects," *IEEE Trans. Industry Applications*, vol. 44, no. 6, pp. 1741-1748, Nov./Dec. 2008.

[83] S. Koonlaboon and S. Sangwongwanich, "Sensorless control of interior permanent-magnet synchronous motors based on a fictitious permanent magnet flux model," in *Proc. IEEE IAS Annual Meeting*, Oct. 2005, pp. 311–318.

[84] I. Boldea, M. C. Paicu, and G. D. Andreescu, "Active flux concept for motion sensorless unified ac drives," *IEEE Trans. Power Electronics*, vol. 23, no. 5, pp. 2612–2618, Sep. 2008.

[85] V. Utkin, J. Guldner, and J. Shi, *Sliding Mode Control in Electromechanical Systems*, 1st ed. New York: Taylor & Francis, 1999

[86] A. Bartoszewicz, "Discrete-time quasi-sliding-mode control strategies," *IEEE Trans. Industry Electronics*, vol. 42, no. 2, pp. 117-122, Apr. 1995.

[87] S. Janardhanan and B. Bandyopadhyay, "Multirate output feedback based robust quasi-sliding mode control of discrete-time systems," *IEEE Trans. Automatic Control*, vol. 52, no. 3, pp. 499-503, Mar. 2007.

[88] X. Chen, T. Fukuda, K. Young, "Adaptive quasi-sliding-mode tracking control for discrete uncertain input-output systems," *IEEE Trans. Industrial Electronics*, vol. 48, no. 1, pp. 216-224, Feb. 2001.

[89] S. Sarpturk, Y. Istefanopulos, and O. Kaynak, "On the stability of discrete-time sliding mode control systems," *IEEE Tran. Automatic Control*, vol. 32, no. 10, pp. 930- 932, Oct. 1987.

[90] S. Sira-Ramiraz, "Non-linear discrete variable structure systems in quasi-sliding mode," *Int. J. Control*, vol. 54, no. 5, pp. 1171-1187, 1991.

[91] W. Gao, Y. Wang, and A. Homaifa, "Discrete-time variable structure control systems," *IEEE Trans. Industrial Electronics*, vol. 42, no. 2, pp. 117-122, Apr. 1995.

[92] G. Foo and M. F. Rahman, "Sensorless sliding-mode MTPA control of an IPM synchronous motor drive using a sliding-mode observer and HF signal injection," *IEEE Trans. Industrial Electronics*, vol. 57, no. 4, pp. 1270-1278, Apr. 2010.

[93] J. Liu, T. A. Nondahl, P. Schmidt, S. Royak, and M. Harbaugh, "Rotor position estimation for synchronous machines based on equivalent EMF," *IEEE Trans. Industry Applications*, vol. 47, no. 3, pp. 1310-1318, May-June 2011.

[94] C. Schauder, "Adaptive speed identification for vector control of induction motors without rotational transducers," *IEEE Trans. Industry Applications*, vol. 28, no. 5, pp. 1054-1061, Sept./Oct. 1992.

[95] M. Cirrincione, A. Accetta, M. Pucci, and G. Vitale, "MRAS speed observer for high-performance linear induction motor drives based on linear neural networks," *IEEE Trans. Power Electronics*, vol. 28, no. 1, pp. 123-134, Jan. 2013.

[96] L. Harnefors and M. Hinkkanen, "Stabilization methods for sensorless induction motor drives - A survey," *IEEE Journal of Emerging and Selected Topics in Power Electronics*, vol. 2, no. 2, pp. 132-142, June 2014.

[97] B. Farhang-Boroujeny, *Adaptive Filters Theory and Applications*, 1st Ed, Wiley, 1999.

[98] M. Corley and R. Lorenz, "Rotor position and velocity estimation for a salient-pole permanent magnet synchronous machine at standstill and high speeds," *IEEE Trans. Industry Applications*, vol. 34, no. 4, pp. 784-789, Jul/Aug 1998.

[99] P. Jansen and R. Lorenz, "Transducerless field orientation concepts employing saturation-induced saliencies induction machines," *IEEE Trans. Industry Applications*, vol. 32, no. 6, pp. 1380-1393, Nov/Dec 1996.

[100] W. Hammel and R. M. Kennel, "Position sensorless control of PMSM by synchronous injection and demodulation of alternating carrier voltage," in *Proc. 1st Symp. SLED*, Jul. 2010, pp. 56–63.

[101] P. Sergeant, F. De Belie, and J. Melkebeek, "Effect of rotor geometry and magnetic saturation in sensorless control of PM synchronous machines," *IEEE Trans. on Magnetics*, vol. 45, no. 3, pp. 1756-1759, March 2009.

[102] S. Yang and R. Lorenz, "Surface permanent-magnet machine self-sensing at zero and low speeds using improved observer for position, velocity, and disturbance torque estimation," *IEEE Trans. Industry Applications*, vol. 48, no. 1, pp. 151-160, Jan./Feb. 2012.

[103] J. Lee, J. Hong, K. Nam, R. Ortega, L. Praly, and A. Astolfi, "Sensorless control of surface-mount permanent-magnet synchronous motors based on a nonlinear observer," *IEEE Trans. Power Electronics*, vol. 25, no. 2, pp. 290-297, Feb. 2010.

[104] J. Jang, J. Ha, M. Ohto, K. Ide, and S. Sul, "Analysis of permanent-magnet machine for sensorless control based on high-frequency signal injection," *IEEE Trans. Industry Applications*, vol. 40, no. 6, pp. 1595- 1604, Nov./Dec. 2004.

[105] P. Garcia, D. Reigosa, F. Briz, C. Blanco, and J. Guerrero, "Sensorless control of surface permanent magnet synchronous machines using the high frequency resistance," in *Proc. IEEE Energy Conversion Congress and Exposition*, Sept. 2011, pp. 2709-2716.

[106] Z. Zhang, Y. Zhao, W. Qiao, and L. Qu, "A space-vector modulated sensorless direct-torque control for direct-drive PMSG wind turbines," *IEEE Trans. Industry Applications*, in press.

[107] Y. Zhao, W. Qiao, and L. Wu, "Sensorless control for IPMSMs based on a multilayer discrete-time sliding-mode observer," in *Proc. IEEE Energy Conversion Congress and Exposition*, Sept. 2012, pp. 1788-1795.

[108] A. V. Oppenheim and R. W. Schafer, *Adaptive Discrete-Time Signal Processing*, 3rd Ed, Prentice Hall, 2009.

[109] Y. Zhao, W. Qiao, and L. Wu, "Dead-time effect and current regulation quality analysisfor a aliding-mode position observer-based sensorless IPMSM drives," in *Proc. IEEE Industry Applications Society Annual Meeting*, Oct. 2012, pp. 1-8.

[110] Y. Zhao, W. Qiao, and L. Wu, "Estimated-speed-aided stabilizers for sensorless control of interior permanent magnet synchronous machines," in *Proc. IEEE Energy Conversion Congress and Exposition*, Sept. 2012, pp. 2631-2638.

[111] Y. Zhao, W. Qiao, and L. Wu, "Oscillation mitigation for sliding mode observers in sensorless control of interior permanent magnet synchronous machines," in *Proc. IEEE Transportation Electrification Conference and Expo*, Jun. 2012, pp. 1-6.